OBSERVATION AND BRANCHING FRACTION MEASUREMENT OF $B^+ \to \psi(2S)\phi K^+$ AT $\sqrt{s} = 8$ TeV IN CMS
&
HADRON SHOWER DEVELOPMENT STUDIES USING GEANT4 SIMULATIONS

by

Reddy Pratap Gandrajula

A thesis submitted in partial fulfillment of the
requirements for the Doctor of Philosophy
degree in Physics
in the Graduate College of
The University of Iowa

December 2016

Thesis Supervisors: Associate Professor Jane Nachtman
Professor Yasar Onel

To my parents, who are simple and kind-hearted farmers, they try to understand and support me all the way.

ACKNOWLEDGEMENTS

The past seven years mean a lot to me. I owe my gratitude to many people that have always been generous to help me.

I express my profound sense of gratitude to my supervisors Associate Professor Jane M Nachtman and Professor Yasar Onel for their immense interest, invaluable guidance, moral support, constant encouragement during the tenure of this work and given me a complete freedom to decide which analyses to work on and in what order. When I moved from ATLAS experiment to CMS experiment for PhD, they had the courage to believe that I would finish the thesis project and successfully graduate in time.

Jane Nachtman has been a wonderful advisor both on physics and on real-life matters. She supported me in getting research funding of every possible opportunity, so that I can stay at Fermilab working on thesis project full time without being a Teaching Assistant at UIowa, and I can travel to conferences such as APS to present my thesis results. Her expertise in writing research proposals helped me in getting the prestigious URA fellowship from Fermilab. The combination of good mentoring with a kind, calm attitude makes Jane very pleasant to work with.

Yasar Onel introduced me to CMS and taught me special topics in physics course twice during my stay at Iowa. I am fortunate to listen to his lectures that showcased his impressive physics knowledge and intuition on Techniques for Nuclear and Particle Physics Experiments. The words of approval and encouragement from him were always important to me.

My deepest thanks to Dr. Kai Yi for his invaluable teaching and guidance throughout my stay at Fermilab as well as at the University of Iowa. He deserves much of the credit for the research presented in this thesis. He has been a source of wisdom and help throughout my PhD study at Iowa.

I would also like to thank Fermilab Scientist Dr. Joel Butler for his insightful comments on all the analysis results in this thesis.

I express my thanks to Dr. Adam Para for his immense knowledge on calorimeter techniques for energy resolution improvement. Conversations with Adam para were invariably instructive and enjoyable. The hadron shower development studies in a calorimeter presented in this manuscript are based on his calorimeter physics ideas.

I thank the members of my thesis committee for useful suggestions: the chairman Assoc. Prof. Jane M Nachtman, Prof. Yasar Onel, Prof. Yannick Meurice, Prof. Wayne Polyzou, Dr. Kai Yi, and Fermilab Scientist Dr. Adam Para. I am fortunate to have Assoc. Prof. Jane M Nachtman as an academic advisor at University of Iowa. Her constant support and encouragement were always important to me. I would also like to thank Prof. Yannick Meurice for teaching me Quantum Gauge Theories course. I am greateful to Prof. Wayne Polyzou for teaching me electromagnetic theory course and for his service and expertise in serving my dissertation committee.

The experimental data upon which this dissertation is based are the fruit of collaborative effort of the people who have built and improved the LHC accelerator and the CMS detector. My contribution to CMS is in the form of signing up for remote data quality shifts at CMS Tier 2 center in Fermilab. I thank Fermilab CMS LPC community for warm hospitality and the intellectually stimulating atmosphere of particle physics that they created around me.

The idea of the B^+ branching ratio measurement with $B^+ \to \psi(2S)\phi K^+$ decay came from Kai Yi and Jane Nachtman. The method of finding and reconstruction of B^+ is suggested by Kai Yi. I wrote much of the computer code for optimizing selection criteria for $B^+ \to \psi(2S)\phi K^+$ reconstruction, significance estimation, BF result, and systematic uncertainty measurements. Working on this project in close collaboration with Kai Yi is one of my most pleasant and stimulating experiences on CMS. I would also like to acknowledge Maksat Haytmyradov, Suleyman Durgut, Viktor D. Khristenko for allowing me in using routines/computer codes developed for their analyses.

The members of the CMS paper committees have ensured high quality of my work and made paper (and therefore this thesis) much more readable:Paula Eerola, James Stewart Russ, Alexis Pompili, sandra malvezzi. I thank all the committee members for their suggestions and criticisms on the paper that is making up this thesis.

I had a privilege to take the excellent courses taught at University of Iowa by William H. Klink, Mary Hall Reno, John A. Goree, Jack D. Scudder, Markus Wohlgenannt. The warm, friendly people at Iowa made my stay enjoyable: Burak Bilki (Thanks for teaching Sipm data analysis), Ping Tan (Thanks for having interesting physics chats during 3:30 pm Fermilab coffee break),James wetzel (Thanks

for thesis writing advises), Hasan Ogul, Emrah Tiras, Kamuran Dilsiz, Christina M. Snyder(Thanks for playing sports at Fermilab, and making Fermilab a livable place). Thanks to Amit, Suranga, Anik, Feng and Siraj for sheltering me from real-life problems.

I would like to express my gratitude to my teachers in India and especially two of the professors in Hyderabad Central University, Dr. Rukmani Mohanta and Dr. Hari Kumar, for teaching me much of the physics I know and being interested in my work at Iowa. I thank Dr.Venktesh Singh, my physics teacher at Banaras Hindu University, for his encouragement many years ago.

Finally, I thank my family for their support and encouragement.

ABSTRACT

Heavy quark decays provide a very advantageous opportunity to test the Standard Model (SM). Recently, promising experiments with b quark, as well as the analysis of the huge data sets produced at the Large Hadron Collider (LHC) experiment, have led to an increasing study and sensitive measurements of relative b quark decays. In this thesis, a preliminary study is presented for the first time observation of the $B^+ \rightarrow \psi(2S)\phi K^+$ with a statistical significance above 5 standard deviations using proton-proton collisions at $\sqrt{s} = 8$ TeV collected with Compact Muon Solenoid (CMS) detector at LHC. The data sample, selected on the basis of the dimuon decay mode of the $\psi(2S)$, corresponds to an integrated luminosity of 19.6 fb^{-1}. A total of 140±15 $B^+ \rightarrow \psi(2S)\phi K^+$ events have been observed. The branching fraction of $B^+ \rightarrow \psi(2S)\phi K^+$ is measured relative to $B^+ \rightarrow \psi(2S)K^+$, whose absolute branching fraction (BF) is known. The ratio is converted to an absolute branching fraction of $B^+ \rightarrow \psi(2S)\phi K^+$, including systematics which is determined to be $(4.0 \pm 0.4(stat) \pm 0.6(syst) \pm 0.1(BR)) \times 10^{-6}$, where the third uncertainty is due to imprecise knowledge of the BF. The upper limit of the fraction of $B^+ \rightarrow \psi(2S)(\mathrm{non} - \phi)K^+$ component in the selected $B^+ \rightarrow \psi(2S)K^+K^-K^+$ channel is found to be 26% at 95% confidence level.

PUBLIC ABSTRACT

Heavy quark decays provide an opportunity to test the Standard Model (SM). Recently, promising experiments with b quark, as well as the analysis of the huge data sets produced at the Large Hadron Collider (LHC) accelerator, have led to an increased study and more sensitive measurements of relative b quark decays. In this thesis, a preliminary study is presented of the first time observation of the $\mathrm{B}^+ \to \psi(2\mathrm{S})\phi\mathrm{K}^+$ with a statistical significance above 5 standard deviations using proton-proton collisions at $\sqrt{s} = 8$ TeV collected with CMS detector at LHC. The branching fraction of $\mathrm{B}^+ \to \psi(2\mathrm{S})\phi\mathrm{K}^+$ is measured relative to $\mathrm{B}^+ \to \psi(2\mathrm{S})\mathrm{K}^+$, whose absolute branching fraction (BF) is known. The $\mathcal{B}(\mathrm{B}^+ \to \psi(2\mathrm{S})\phi\mathrm{K}^+)$ is determined to be $(4.0 \pm 0.4(stat) \pm 0.6(syst) \pm 0.1(BR)) \times 10^{-6}$, where the third uncertainty is from the imprecision in the normalization channel.

TABLE OF CONTENTS

CHAPTER

LIST OF TABLES

Table

LIST OF FIGURES

Figure

CHAPTER 1
INTRODUCTION ON MATTER

A series of experiments on cosmic rays and with particle accelerators designed to probe the sub-nuclear structure of matter has revealed that there are two distinct types of matter. There are six fundamental particles like the electron that do not experience the strong nuclear force; these were named leptons from the Greek for lightweight. Then there are hadrons (Greek for bulky) that do feel the strong nuclear force, and researchers have discovered well over 200 of these. Hadrons may be usefully divided into baryons and mesons. Baryons are particles of spin 1/2 that are unstable and decay, ultimately returning to a proton. Mesons are particles with integer spin that ultimately decay to electrons, photons and neutrinos.

Studies of the proliferation of hadrons eventually gave hints of an underlying pattern which researchers called the Eightfold Way. Identification of such patterns lead to the proposal that hadrons are not fundamental but are composed of at least three varieties of quarks; the up (u), the down (d) and the strange (s). This served to explain most observed hadronic phenomena except for a few, among which was the observed rate of $K_L^0 \to \mu^+\mu^-$ which was lower than expected [1]. Introducing a fourth quark, the charm c, within the Glashow-Iliopoulos-Maiani (GIM) mechanism produced the required interference with the u being exchanged between the d and s quarks of the K_L^0 meson to lower the theoretical rate [2]. The mass of the charm quark required to lower the theoretical rate to the observed value was calculated to be in the range of a few GeV.

Bound states of the charm quark were subsequently discovered, the almost simultaneous discovery of the $J/(c\bar{c})$ meson at SLAC and BNL in November 1974 being among the most prominent. The b quark belongs to the third generation of quarks and is the weak doublet partner of the t quark. The existence of the third generation quark doublet was proposed in 1973 by Kobayashi and Maskawa [3] in their model of the quark mixing matrix (CKM matrix), and confirmed four years later by the first observation of a $b\bar{b}$ meson [4]. This was followed by the discovery of top (1995) quark [5, 6] at Fermilab.

The bound states of a b antiquark and a u, d, s, or c quark are referred to as the $B_u(B^+)$, $B_d(B^0)$, B_s^0, and B_c^+mesons, respectively. Experimental studies of b decays have been performed in e^+e collisions at the $\Upsilon(4S)$ resonance (ARGUS, CLEO, Belle, and BaBar), as well as at higher energies at the Z resonance (SLC and LEP) and in $p\bar{p}$ collisions (Tevatron). High-energy $p\bar{p}$ collisions produce b-flavored hadrons of all species with a very large cross-section ($\sigma(p\bar{p} \to bX, |\eta| < 1) \sim 30\mu b$ at the Tevatron, which is expected to be ten times larger at the LHC pp collider with $\sqrt{s} = 14$ TeV). Detectors operating at the above experiments have a high efficiency for most decays and have provided large samples of a rich variety of decays of B^+ mesons. With the availability of large data samples, it is now possible to look for rare B^+ meson decays and search for possible structures in subsystems of B^+ decay productions.

1.1 The Standard Model

The Standard Model of particle physics, formulated in the 1970s, is a theory of fundamental particles and their interactions, is based on experiments that started in 1897 with the discovery of the electron. Its theoretical framework is based on the quantum theory of fields and it provides the most accurate description of nature at the subatomic level so far. According to this model, all matter is built from a small number of fundamental spin-$\frac{1}{2}$ particles called *fermions*, six *quarks* and six *leptons* which follow the Fermi-Dirac statistics, while the carriers of the interactions are characterized as *bosons*, which possess integer spin (either 0 or 1) and follow the Bose-Einstein statistics. There are seventeen named particles in the SM, as shown in Fig. 1.1. The Higgs boson, as the last particle in the SM, was discovered in 2012 [7, 8].

There are four known fundamental interactions in the universe: the gravitational, the electromagnetic, the weak and the strong interactions. These work over different ranges and have different strengths. Gravity, acting between all types of particle, is the weakest but it has an infinite range. It is supposedly mediated by exchange of a spin-2 boson, the *graviton*, which has not yet been observed. Even though it is universal and is dominant on the scale of the universe, gravity is not included in the SM because it is much weaker than the other forces and can be ignored at the level of individual subatomic particles. The electromagnetic interaction occurs between all charged particles and is mediated by *photon* (γ) exchange. It also has infinite range but it is many times stronger than gravity. The weak and strong interactions are effective only over a very short range and dominate only at the level of subatomic particles. The weak interaction is associated with the exchange of elementary spin-1 bosons between quarks and/or leptons. These mediators are $W^{\pm}$ and Z^0 bosons, with masses of order 100 times the proton mass. The strong interaction, as its name suggests, is the strongest of all four fundamental interactions. It is responsible for binding the quarks in the neutron and proton, and the neutrons and protons within nuclei. The strong force is mediated by spin-1, massless particles known as *gluons*, which couple to color charge, rather like the photons couple to electromagnetic charge.

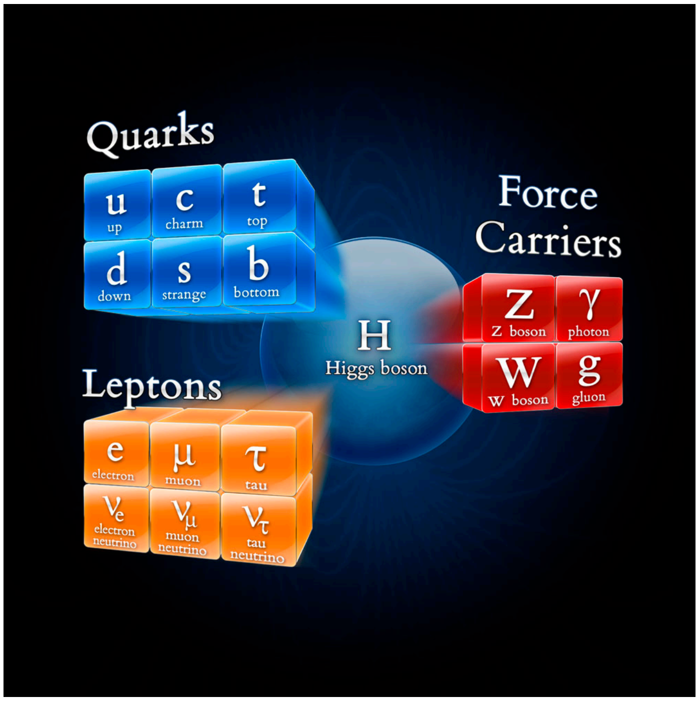

Figure 1.1: Fundamental building blocks of matter: The SM of Elementary Particles (matter fermions includes first three generations of quarks and leptons, gauge bosons, and the Higgs boson)

Fermions are fundamental matter particles in the SM. These twelve particles (six *leptons* and six *quarks*) can be grouped into three generations. The lightest and most stable particles make up the first generation, whereas the heavier and less stable particles belong to the second and third generations. The *leptons* carry integral electric charge. The charged *leptons* are the electron, muon and tau, while the neutral leptons are the corresponding neutrinos. A different "flavor"of neutrino is paired with each "flavor"of charged lepton, as indicated by the subscript, i.e., (e, ν_e), (μ, ν_μ) and (τ, ν_τ). The charged muon and tau are both unstable and decay spontaneously to electrons, neutrinos and other particles. The mean lifetime of the muon is 2.2×10^{-6} s, that of the tau only 2.9×10^{-13} s. Neutrinos were postulated by Pauli in 1930 in order to account for the energy and momentum missing in the process of nuclear β-decay. They experience the weak interactions only. The *quarks* carry fractional electric charges, of $+\frac{2}{3}e$ or $-\frac{1}{3}e$. The quark "flavor"is denoted by a symbol: u for 'up', d for 'down', s for 'strange', c for 'charmed', b for 'bottom'and t for 'top'. While leptons exist as free particles, quarks are not found to do so. The bound states of quarks are called *hadrons*, and can be categorized into two families: baryons (made of three quarks) and mesons (made of one quark and one anti-quark). Each quark carries one of the three colors (or color charges): r, g and b. Quarks are bound together by *gluons*, which are also colored. Fig.1.1 shows that the three lepton pairs are exactly matched by the three quark pairs.

1.2 The Electroweak Theory

1.2.1 Weak Interactions

The weak interaction is mediated by three massive bosons, the charged $W^{\pm}$ and the neutral Z^0. The W^+ and W^- are anti-particles of each other, while the Z^0, like the photon, is its own anti-particle. Depending on whether leptons and/or hadrons are involved, the weak interaction can be conventionally divided into three categories: (i) purely leptonic processes, e.g., $\mu^- \to e^- + \bar{\nu}_e + \nu_\mu$, (ii) semi-leptonic processes involving both hadrons and leptons, e.g., neutron β-decay $n \to p + e^- + \bar{\nu}_e$, and (iii) purely hadronic processes, e.g., $\Lambda \to p + \pi^-$. Perturbation theory is valid for weak and electromagnetic interactions. In the 1960s, a theory of electroweak interactions was developed by Sheldon Glashow, Abdus Salam and Steven Weinberg that can unify the electromagnetic and weak interactions.

So far, the experimental data on a wide range of leptonic and semi-leptonic processes are consistent with the assumption that the lepton fields enter the interaction only in the combinations

$$\begin{aligned} J_\alpha(x) &= \sum_l \bar{\psi}_l(x)\gamma_\alpha(1-\gamma_5)\psi_{\nu_l}(x), \\ J^\dagger_\alpha(x) &= \sum_l \bar{\psi}_{\nu_l}(x)\gamma_\alpha(1-\gamma_5)\psi_l(x), \end{aligned} \tag{1.1}$$

where $J_\alpha(x)$ and $J^\dagger_\alpha(x)$ are called leptonic currents, $l = e, \mu, \tau$, ψ_l and ψ_{ν_l} are the corresponding quantized fields in Eq. (1.1). We can describe the weak interaction as due to the transmission of quanta, i.e., $W^{\pm}$. For example, the interaction Hamiltonian density of quantum electrodynamics (QED), according to the intermediate vector boson (IVB) theory can be given by

$$\mathcal{H}_I(x) = g_W J^{\alpha\dagger}(x) W_\alpha(x) + g_W J^\alpha(x) W_\alpha^\dagger(x), \tag{1.2}$$

1.3 Quantum Chromodynamics

Quantum chromodynamics (QCD) is the standard theory to describe the strong interactions in which the color quantum number has been introduced as an extra degree of freedom. The color charge of a quark has three possible values, r, g and b, while anti-quarks carry anti-colors, $\bar{r}$, $\bar{g}$ and $\bar{b}$. The mediating bosons of the quark-quark interactions are called *gluons*, each carrying a color and an anti-color and postulated to belong to an octet of states.

Quarks and gluons are observed indirectly, which means that the evidence of their existence inside hadrons exists but these particles have not been observed individually. Experiments to study the strong interactions are performed with hadrons, not with the quarks and gluons that are described by quantum field theory (QFT). To explore or determine the quark and gluon structure of hadrons, structure functions are introduced to give the properties of a certain particle interaction without including all of the underlying physics. The experimental technique is to measure the angular distribution of some processes and compare them to that from a point particle; then the structure of the hadron can be deduced from some form factors (functions of the transferred momentum square). As an example, a charge distribution with electrons can be probed by measuring the cross section for scattering electrons [9]:

$$\frac{d\sigma}{d\Omega} = (\frac{d\sigma}{d\Omega})_{point} |F(q)|^2, \tag{1.3}$$

where q is the transferred momentum and $F(q)$ is the corresponding form factor.

Quantum Chromodynamics (QCD) is the sector of the Standard Model (SM) which is relevant for the strong interactions. It is obtained from the full SM by setting the weak and electromagnetic coupling constants to zero and freezing the scalar doublet to its vacuum expectation value. What remains is a Yang–Mills (YM) theory with local gauge group $SU(3)$ (color) vectorially coupled to six Dirac fields (quarks) of different masses (flavors). The vector fields in the YM Lagrangian (gluons) live in the adjoint representation and transform like connections under the local gauge group whereas the quark fields live in the fundamental representation and transform covariantly. The QCD Lagrangian reads [9]

$$\mathcal{L}_{\mathrm{QCD}} = -\frac{1}{4} F^a_{\mu\nu} F^{a\,\mu\nu} + \sum_{\{q\}} \bar{q}\left(i\gamma^\mu D_\mu - m_q\right) q\,, \tag{1.4}$$

where $\{q\} = u, d, s, c, b, t$, $F^a_{\mu\nu} = \partial_\mu A^a_\nu - \partial_\nu A^a_\mu + g f^{abc} A^b_\mu A^c_\nu$, $D_\mu = \partial_\mu - i T^a A^a_\mu$. f^{abc} are the $SU(3)$ structure constants and T^a form a basis for the fundamental representation of the $SU(3)$ algebra. When coupled to electromagnetism, gluons behave as neutral particles whereas u, c and t quarks have charges of $+2/3$ and d, s and b quarks have charges of $-1/3$.

The main properties of QCD are as follow [9]:

- It is Poincaré, parity, time reversal and (hence) charge conjugation invariant. It is in addition invariant under $U(1)^6$ which implies individual flavor conservation.
- Being a non-Abelian gauge theory, the physical spectrum consists of color singlet states only. The simplest of these states have the quantum numbers of

quark–antiquark pairs (mesons) or of three quarks (baryons), although other possibilities are not excluded.

- The QCD effective coupling constant $\alpha_s(q)$ decreases as the momentum transfer scale q increases (asymptotic freedom) [10, 11]. This allows for perturbative calculations in α_s at high energies.
- At low energies it develops an intrinsic scale (mass gap), usually referred as Λ_{QCD}, which provides the main contribution to the masses of most hadrons. At scales $q \sim \Lambda_{\text{QCD}}$, $\alpha_s(q) \sim 1$ and perturbation theory cannot be used. Investigations must be carried out using nonperturbative techniques, the best established of which is lattice QCD.

  Quarks are conventionally divided into light $m_q \ll \Lambda_{\text{QCD}},\ \ q = u, d, s$ and heavy $m_Q \gg \Lambda_{\text{QCD}},\ \ Q = c, b, t$

$$\begin{aligned} &m_u = 2.3^{+0.7}_{-0.5}\,\text{MeV}\,, \quad m_d = 4.8^{+0.5}_{-0.3}\,\text{MeV}\,, \quad m_s = 95 \pm 5\,\text{MeV}\,, \\ &m_c = 1.275 \pm 0.025\,\text{GeV}\,, \quad m_b = 4.18 \pm 0.03\,\text{GeV}\,, \quad m_t = 173.21 \pm 0.51 \pm 0.71\,\text{GeV}\,. \end{aligned} \tag{1.5}$$

  These are $\overline{\text{MS}}$ masses at scale 2 GeV, m_c and m_b for the light quarks, charm and bottom respectively. All values are taken from [66].

- If light quark masses are ignored, the $U(1)^3$ flavor conservation symmetry of the QCD Lagrangian in this sector is enlarged to a $U(3) \otimes U(3)$ group. The axial $U(1)$ subgroup is explicitly broken by quantum effects (axial anomaly). The vector $U(1)$ subgroup provides light flavor conservation. The remaining

$SU(3) \otimes SU(3)$ subgroup, known as chiral symmetry group, turns out to be spontaneously broken down to the diagonal $SU(3)$ (flavor symmetry). This produces eight Goldstone bosons, which, upon taking into account the explicit breaking of the symmetry due to the non-zero quark masses, acquire masses that are much smaller than $\Lambda_{\rm QCD}$.

- Hadrons containing heavy quarks have masses of the order of m_Q rather than of the order $\Lambda_{\rm QCD}$. They enjoy particular kinematical features that allow for specific theoretical treatments. The study of hadrons containing two heavy quarks is the aim of this report.

1.4 Summary

The Standard Model is a gauge theory which successfully describes the fermions and their interactions mediated by the gauge bosons. A brief history of experimental discovery of the heavy quarks is presented.

CHAPTER 2
THEORETICAL TOOLS

2.1 Introduction to Heavy Quark Physics

2.1.1 Heavy quark production

In hadron-hadron collisions, the leading-order processes for a heavy quark production contain both light quark annihilation and gluon-gluon fusion. During the last few years, B physics has received a lot of attention, both from theorists and experimentalists, and we are presently at the B-factory era in particle physics. The BaBar(SLAC), BELLE (KEK) and HERA-B (DESY) detectors have already seen their first events, and CLEO-III (Cornell), CDF-II and D0-II (Fermilab) will start taking data in the near future (see [2] for a recent experimental overview). Although the physics potential of these experiments is very promising, it may as well be that the definite answer in the search for new physics in B decays will be left for second-generation B experiments at hadron machines. In the following, we will give an overview of the B-physics potential of the LHC experiments ATLAS, CMS and LHCb, with the main focus on SM physics

2.1.2 Heavy quark decays

The exploration of physics with b-flavored hadrons offers a very fertile testing ground for the SM description of electroweak interactions. Studies of the decays of bound states of bottom quarks and light antiquarks have proven to be one of the most effective ways to explore the decay dynamics of heavy quark systems. The measurements of semileptonic decays of B^+ mesons, where a charged lepton and its corresponding neutrino are produced, have proven to be useful in the development of theoretical models that relate the semileptonic branching fractions to each other [15]. In a similar way, the measurements of the fully hadronic decays (modes where the B^+ meson decay daughters are hadrons) have also been shown to provide tests of the theory of heavy quark decay [16, 17].

The decay of hadrons containing b quark can be treated by the spectator model. Considering only the CKM-favored decay modes, the main decay channels for b quarks are $b \to c\bar{u}d, c\bar{c}s, cl\bar{\nu}_l(l = e, \mu, \tau)$.

2.2 Quarkonium

A bound state of a heavy quark-antiquark pair, $Q\bar{Q}$, is called quarkonium. The first quarkonium state, which is made up of $c\bar{c}$ and named $J\psi$, was discovered in late 1974 when a narrow vector state of mass around 3.1 GeV, decaying into e^+e^- and $\mu^+\mu^-$, was observed simultaneously at Brookhaven and SLAC [18, 19].

2.2.1 Quarkonium spectrum

A quarkonium state is characterized by the radial excitation level n, the total spin of the quark-antiquark pair S, the total orbital angular momentum L, and the total angular momentum $J(J = L + S)$.

2.2.2 Quarkonium production

Production of quarkonium states is a two-step process: first a heavy quark and antiquark pair is produced in the regime of perturbative QCD; then the formation of a bound state, which is driven by non-perturbative QCD. Some of the theoretical models which interpret the rate of the quarkonium production measured by experiments are listed below:

- Color Singlet Model
- Fragmentation Contribution
- Color Octet Model

2.3 Physics of B mesons

The charged B meson is a bound state of one heavy bottom quark and one light up quark.

2.3.1 B meson production

The production of B meson requires the production of the heavy quark pair $b\bar{b}$ then a soft non-perturbative binding of one of these bottom quark with light up quark in the final state. The b quark production cross section as a function of Center of Mass Energy of proton-(anti)proton collisions is shown in Fig. 2.1.

2.3.2 $B^+ \to \psi(2S)\phi K^+$ decay

The branching fraction of the decay of $B^+ \to \psi(2S)\phi K^+$ depends on a blend of effects due to the weak and strong interactions. In the following sections, I will

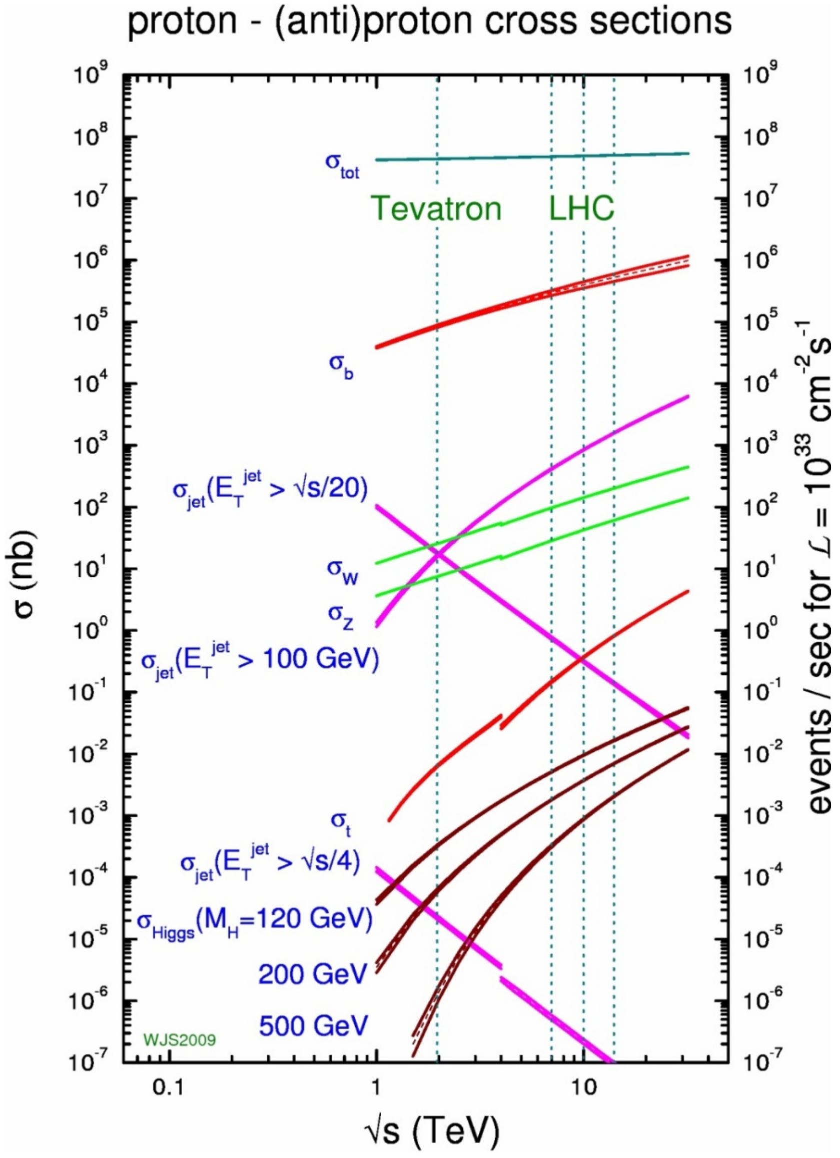

Figure 2.1: b quark production cross section as a function of Center of Mass Energy of proton-(anti)proton collisions [13].

provide a possible formalism for theoretical calculation of $BF(B^+ \to \psi(2S)\phi K^+)$. Throughout this thesis, references to a specific decay mode imply the charge conjugate mode as well.

2.4 Possible Feynman diagram for $B^+ \rightarrow \psi(2S)\phi K^+$ decay:

As illustrated in the diagram in Fig. 2.2, both of the $\psi(2S)$ decay modes are color-suppressed Cabibbo-favored decays; for instance $B^+ \rightarrow \psi(2S)K^+$ can only occur when the W bosons hadronic decay products, themselves a color singlet, combine with the charm antiquark from the flavor-changing decay and the light spectator quark to form color-singlet charmonium and strange meson. Strong interaction effects, however, are expected to modify the dynamics of these decays. The most successful theoretical treatments of such decays employ the factorization hypothesis, where the decay of the B^+ meson is described by processes that take place on different time scales: short-distance hard-gluon exchange and the weak nonleptonic decay of the b quark, followed by longer-distance strong

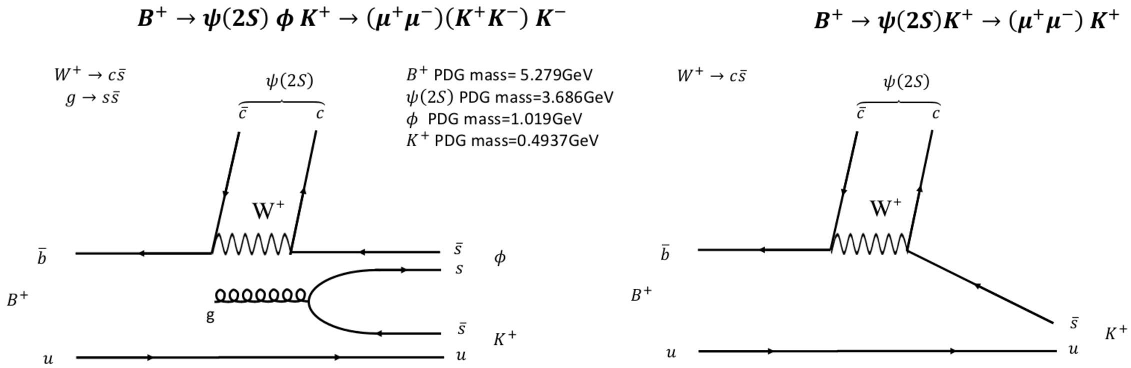

Figure 2.2: Feynman diagram of possible B decay. Diagram of the color-suppressed internal W emission mechanism for a B^+ decaying to charmonium ($\psi(2S)$), ϕ meson, and a strange meson (K^+) shown left or $\psi(2S)K^+$ state shown right. In this process, the u quark is assumed to be a spectator of the weak interaction (plus strong interaction in case of $\psi(2S)\phi K^+$) [14].

interactions between the final-state partons that produce the two or three daughter mesons. The decay amplitude is factorized into a product of hadronic currents that reduces to the charmonium decay constant and the matrix element for the $B^+ \to K^+$ hadronic current, which consists of several form factors [16, 17]. Measurements of the rates and polarization of these decays confront the assumptions that underlie the factorization hypothesis in B-meson decays and the calculations involving hadronic form factors [20].

Table 2.1: Branching fractions of the known decays of the B^+.

Mode	Branching Fraction
$BF(B^+ \to \psi(2S)K^+)$	$(6.27 \pm 0.24) \times 10^{-4}$
$BF(B^+ \to J/\psi\phi K^+)$	$(5.2 \pm 1.7) \times 10^{-5}$

2.5 $B^+ \to \psi(2S)K^+$ Decay Formalism

Exclusive B^+ hadronic decays are difficult for theory prediction. Even though over the years theorists developed a qualitative understanding and consistent quantitative description of two-body decays [21], some features still lack a clear dynamical explanation. The decay mode B $\to$ ψ(2S)K containing two heavy quarks in the final state may shed some light on the factorization method calculations.

Application of the QCD sum rule to exclusive heavy meson decays involves theoretical consideration of effects from (a) hard gluon exchange at short distances, (b) soft interactions of quarks and gluons including nonspectator effects, (c) hadronization, and (d) final state interactions among the hadronic decay products. Up to now, only the hard-gluon effects can be systematically taken into account in the framework of improved QCD perturbation theory. The result is an effective weak Hamiltonian at the physical scale $\mu \simeq m_Q \ll m_W$, given by a sum of local operators with renormalized Wilson coefficients [21].

The piece of the effective Hamiltonian relevant for B $\rightarrow \psi$(2S)K decay mode may be written in the form [21],

$$H_W = \frac{G}{\sqrt{2}} V_{cb} V_{cs}^* (c_2 + \frac{c_1}{3}) O_2 + 2c_1 \tilde{O}_2, \tag{2.1}$$

where

$$O_2 = (\bar{c}\Gamma^\rho c)(\bar{s}\Gamma_\rho b), \quad \tilde{O}_2(\mu) = (\bar{c}\Gamma^\rho \frac{\lambda^a}{2} c)(\bar{s}\Gamma_\rho \frac{\lambda^a}{2} b) \tag{2.2}$$

with $\Gamma_\rho = \gamma_\rho(1-\gamma_5)$. The Wilson coefficients $c_i(\mu)$ contain the effects from QCD interactions at short distances below the scale set by the inverse b-quark mass. The hadronic matrix elements of the four-quark operators Eq.(2.2) are supposed to incorporate the long-distance effects (b) to (d).

In a radical first approximation, one may factorize the matrix elements of H_W for $B \rightarrow J/\psi K$ into products of hadronic matrix elements of the currents that compose H_W. Strong interactions at scales lower than μ between quarks entering different currents as well as nonspectator effects are thereby completely neglected. Moreover, the matrix element of the operator $\tilde{O}_2$ vanishes because of color conservation so that

$$\langle\psi(2S)K|H_W|B\rangle = \frac{G}{\sqrt{2}}V_{cb}V_{cs}^*\left(c_2(\mu)+\frac{c_1(\mu)}{3}\right)\langle\psi(2S)K|O_2(\mu)|B\rangle. \tag{2.3}$$

The factorized matrix element of the operator O_2 is given by

$$\langle\psi(2S)K|O_2(\mu)|B\rangle = \langle\psi(2S)|\bar{c}\Gamma^\rho c|0\rangle\langle K|\bar{s}\Gamma_\rho b|B\rangle = 2f_{\psi(2S)}f^+_{B\to K}m_\psi(\epsilon^{\psi(2S)}.q), \tag{2.4}$$

where $f_{\psi(2S)} = 282$ MeV is the decay constant determined by the leptonic width $\Gamma(\psi(2S)\to l^+l^-) = 5.26\pm0.37$keV, and $f^+_{B\to K} = 0.55\pm0.05$ is the $B\to K$ form factor at the momentum transfer $p^2 = m^2_{\psi(2S)}$ estimated [22] from a light-cone sum rule similar to the one for the $B\to\pi$ form factor. Obviously, $\epsilon^{\psi(2S)}$ denotes the $\psi(2S)$ polarization vector, and q the K four-momentum. The above approximation can at best be valid at a particular value of μ which could be called the factorization scale μ_F. The conventional assumption is $\mu_F = O(m_b)$.

Using the next-to-leading order coefficients $c_{1,2}(\mu)$ in the HV scheme with $\Lambda^5_{\bar{M}S} = 225$MeV from [23] and taking $\mu = m_b \simeq 5$ GeV, one has

$$c_2(\mu)+\frac{c_1(\mu)}{3} = 0.155. \tag{2.5}$$

The prediction for the branching ratio of $B^+\to\psi(2S)K^+$ two-body decay using the NRSX model [24] is,

$$BR(B^+\to\psi(2S)k^+) = 0.05\% \tag{2.6}$$

2.6 Summary

Heavy quark production and decays are discussed. Quarkonium spectroscopy, in particular the B^+ meson production is presented. In summary, the B^+ meson decay formalism, and the theoretical predictions for branching ratio of $B^+ \to \psi(2S)K^+$ two body decay in NRSX model are presented.

CHAPTER 3
LHC AND THE CMS DETECTOR

3.1 The LHC

The Large Hadron Collider as shown in Fig. 3.1, is the worlds largest and most powerful particle accelerator. It first started up on 10 September 2008, and remains the latest addition to CERNs accelerator complex. The LHC consists of a 27-kilometer ring of superconducting magnets with a number of accelerating structures to boost the energy of the particles along the way. Inside the accelerator, two high-energy particle beams travel at close to the speed of light before they are made to collide. The beams travel in opposite directions in separate beam pipes two tubes kept at ultrahigh vacuum. They are guided around the accelerator ring by a strong magnetic field maintained by superconducting electromagnets. The electromagnets are built from coils of special electric cable that operates in a superconducting state, efficiently conducting electricity without resistance or loss of energy. This requires chilling the magnets to -271.3C a temperature colder than outer space. For this reason, much of the accelerator is connected to a distribution system of liquid helium, which cools the magnets, as well as to other supply services.

Thousands of magnets of different varieties and sizes are used to direct the beams around the accelerator. These include 1232 dipole magnets 15 meters in length which bend the beams, and 392 quadrupole magnets, each 57 meters long, which focus the beams. Just prior to collision, another type of magnet is used to ”squeeze” the

Figure 3.1: The Large Hadron Collider is the world's largest and most powerful particle accelerator. Four experiments lie along the beam line (Image: CERN).

particles closer together to increase the chances of collisions. The particles are so tiny that the task of making them collide is akin to firing two needles 10 kilometers apart with such precision that they meet halfway. All the controls for the accelerator, its services and technical infrastructure are housed under one roof at the CERN Control Center. From here, the beams inside the LHC are made to collide at four locations around the accelerator ring, corresponding to the positions of four particle detectors ATLAS, CMS, ALICE, and LHCb.

Each of this experiment is designed for distinctive purposes. Two of them, CMS and ATLAS are general purpose detectors and others, ALICE and LHCb are specific purpose experiments. The LHC operation center of mass energy was 7 TeV in 2010, 2011 and 8 TeV in 2012. The total integrated luminosity respectively is $44.2pb^{-1}$, $6.1fb^{-1}$, and $23.3fb^{-1}$. Fig. 3.5 (left) shows the total integrated luminosity recorded by CMS in 2010, 2011 and 2012 . The LHC operation parameters at $\sqrt{s} = 7$ TeV is shown in Fig. 3.2 at collision rates $\sim 10^9$ Hz and event selection rate $\sim 1/10^{13}$.

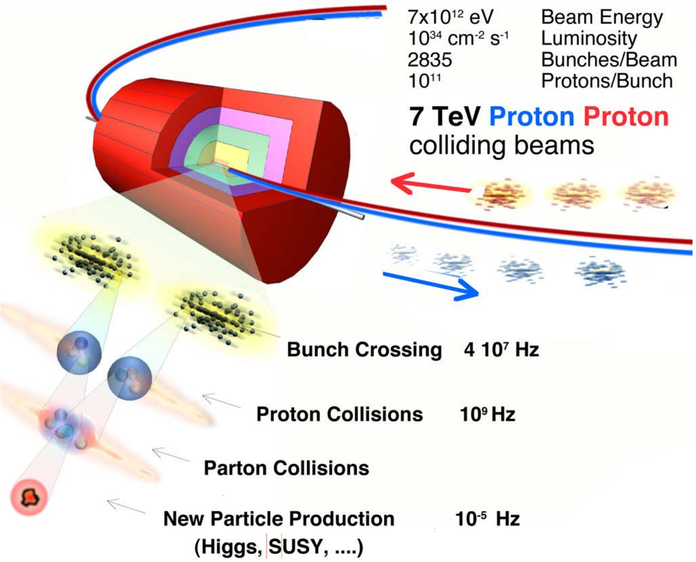

Figure 3.2: THE LHC with 7 TeV operation parameters [43].

3.1.1 The LHC Luminosity

The smallest opening we can squeeze the beam through is defined as the Transverse Emittance (ϵ), and can also be considered as a measurement of the parallelism of a beam. The amplitude function, β, is determined by the accelerator magnet configuration (basically, the quadrupole magnet arrangement) and powering. When expressed in terms of σ (cross-sectional size of the bunch) and the transverse emittance, the amplitude function β becomes $\beta = \pi.\sigma^2/\epsilon$.

β^* is referred to as the distance from the focus point that the beam width is twice as wide as the focus point as shown in Fig. 3.3.

The LHC Luminosity can be measured using the expression:

$$\begin{aligned} L &= \frac{f.N_1 N_2}{(4\pi\sigma_x\sigma_y)} \\ &= \frac{f.N_1 N_2}{(4.\epsilon.\beta^*)} \end{aligned} \tag{3.1}$$

Where, the so far achieved parameters are, the instantaneous luminosity = $7 \times 10^{33} cm^2/s$, frequency of bunch crossing= 20×10^6 Hz, number of protons per bunch= $N < 1.7 \times 10^{11}$, $\epsilon = 175\mu m$, and $\beta^* = 0.60$ m. In practice if σ_x and σ_y are respectively the transverse areas of the beam interaction region, we use the equivalent formula to measure the Luminosity. The areas of the beam are obtained by scanning the two beams and measuring the rate of collisions while the number of protons in the bunches is measured by dedicated devices of the accelerator.

Fig. 3.5 (right) shows the LHC run efficiency in 2012 in proton-proton collision mode. LHC performed very well by providing stable beams in 35.81% of run availability based on LHC physics schedule after overcoming many machine operation challenges.

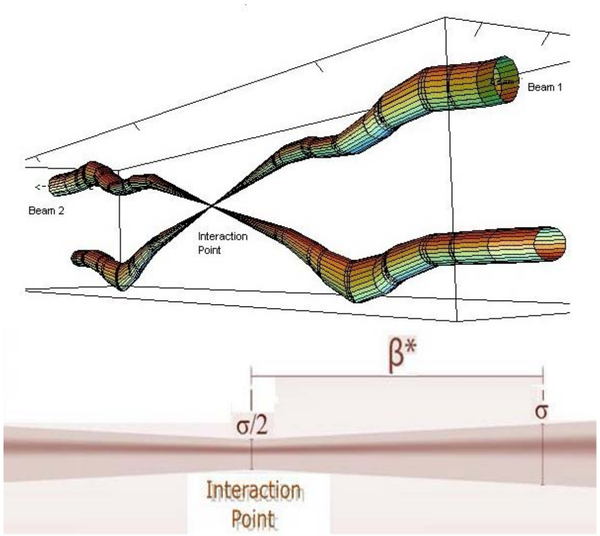

Figure 3.3: The β^* definition [43].

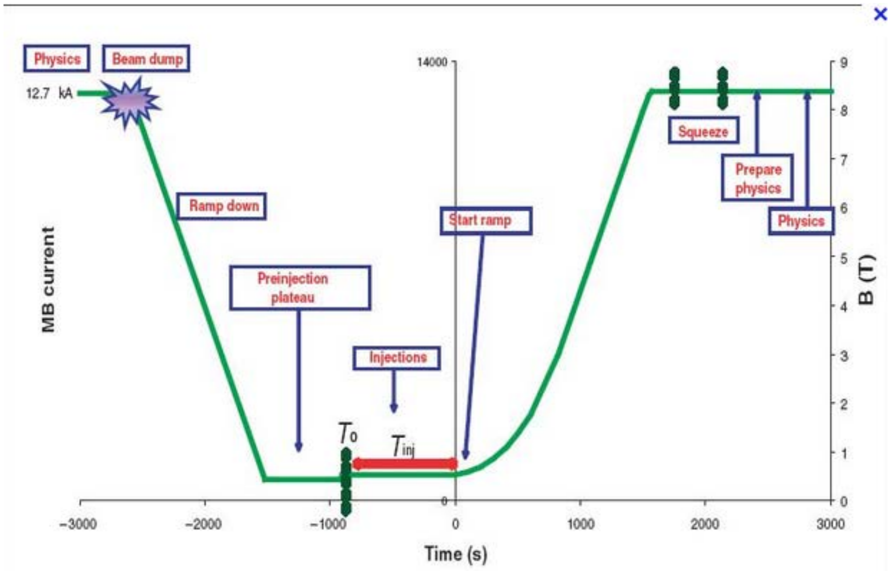

Figure 3.4: LHC Operation [43].

3.2 Compact Muon Solenoid (CMS)

The central feature of the Compact Muon Solenoid (CMS) apparatus is a superconducting solenoid of 6 m internal diameter, providing a field of 3.8 T (magnetic

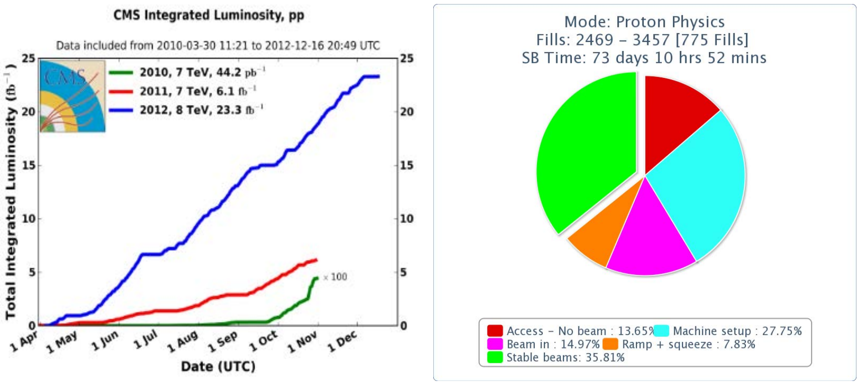

Figure 3.5: CMS Integrated Luminosity, PP data is shown on left and LHC performance, Run efficiency in 2012 is shown on right.

energy stored ∼2.7 GJ). The magnet is the Solenoid in Compact Muon Solenoid (CMS). The solenoid is a coil of superconducting wire that creates a magnetic field when electricity flows through it; in CMS the solenoid has an overall length of 13m and a diameter of 7m, and a magnetic field about 100,000 times stronger than that of the Earth. It is the largest magnet of its type ever constructed and allows the tracker and calorimeter detectors to be placed inside the coil, resulting in a detector that is, overall, compact, compared to detectors of similar weight. A cutaway view of the CMS detector is shown in Fig. 3.6. CMS uses a right-handed coordinate system, with the origin at the nominal interaction point, the x-axis pointing to the center of the LHC, the y-axis pointing up (perpendicular to the LHC plane), and the z-axis along the anticlockwise-beam direction. The polar angle (θ) is measured from the positive z-axis and the azimuthal angle (Φ) is measured from the positive x-axis in the x-y plane, whereas the radius (r) denotes the distance from the z-axis.

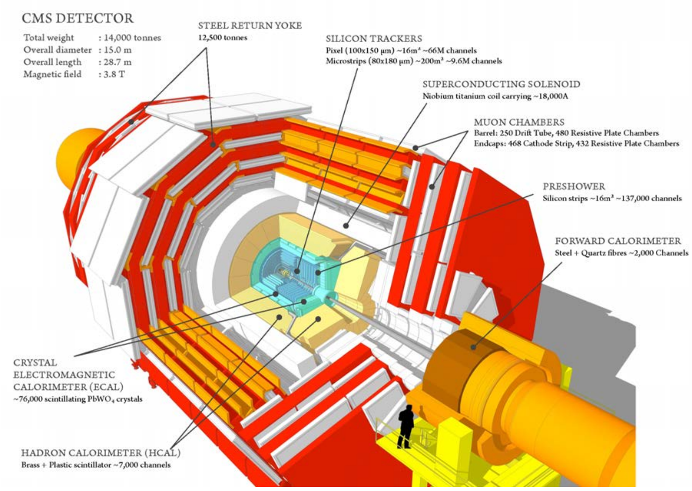

Figure 3.6: Sectional view of the CMS detector. The LHC beams travel in opposite directions along the central axis of the CMS cylinder colliding in the middle of the CMS detector [26].

3.2.1 Pixel and Silicon Tracking system

Within the field volume are a silicon pixel and strip tracker, a crystal electromagnetic calorimeter (ECAL) and a brass/scintillator hadron calorimeter (HCAL). Muons are measured in gas-ionization detectors embedded in the steel return yoke. Extensive forward calorimetry complements the coverage provided by the barrel and endcap detectors. The pixel tracker allows the reconstruction of charged particle trajectories in the region closest to the interaction point, consists of three 53.3 cm long barrel layers and two endcap disks on each side of the barrel section, as shown in Fig. 3.7 [29].

The innermost barrel layer has a radius of 4.4 cm, while for the second and third layers the radii are 7.3 cm and 10.2 cm, respectively. The layers are composed of modular detector units (called modules) placed on carbon fiber supports (called

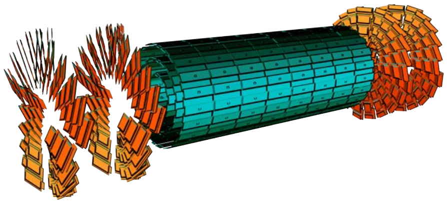

Figure 3.7: CMS Pixel detector, Sensors: n-on-n Silicon with size 150× 100 μm [43].

ladders). Each ladder includes eight modules, shown in Fig. 3.8, consisting of thin, segmented n-on-n silicon sensors with highly integrated readout chips (ROC) connected by indium bump-bonds. Each ROC serves a 52×80 array of 150μm×100μm pixels. The ladders are attached to cooling tubes, which are part of the mechanical structure. The barrel region is composed of 672 full modules and 96 half modules, each including 16 and 8 ROCs, respectively. The number of pixels per module is 66 560 (full modules) or 33 280 (half modules). The total number of pixels in the barrel section is 47 923 200. The endcap disks, extending from 6 to 15 cm in radius, are placed at z =±35.5 cm and z=±48.5 cm. Disks are split into half-disks, each including 12 trapezoidal blades arranged in a turbine-like geometry. Each blade is a sandwich of two back-to-back panels around a U-shaped cooling channel. Rectangular sensors of five sizes are bump-bonded to arrays of ROCs, forming the so-called plaquettes. Three (four) plaquettes are arranged on the front (back) panels with overlap to provide full coverage for charged particles originating from the interaction point. The endcap disks include 672 plaquettes, for a total of 17 971 200 pixels. The pixel detector dressed up with optical fibers is shown in Fig. 3.11.

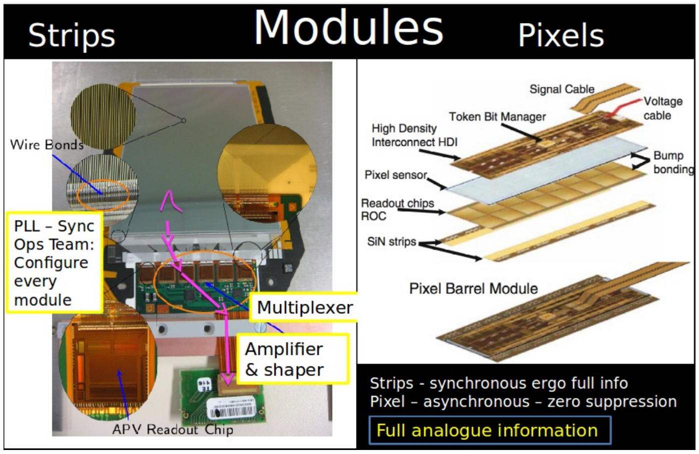

Strips - synchronous ergo full info
Pixel – asynchronous – zero suppression
Full analogue information

Figure 3.8: Barrel Module [43].

The basic working principle of silicon sensor is shown in Fig. 3.9. Electron-hole-pairs generated by ionizing particles traversing the silicon are separated by the electric field and drift to the electrodes. Strips collect holes and pixels collect electrons.

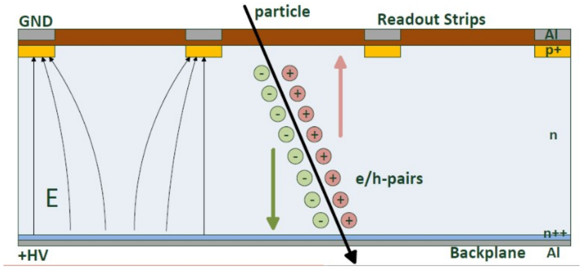

Figure 3.9: Basic working principle of silicon sensor [43].

The outer radius of the tracking system is 110 cm, length = 270 cm, and immersed in ~4 Tesla magnetic field. On an average there are 12 hits per track. The hit resolution is defined as: $\frac{pitch}{\sqrt{12}}$, with pitch$\sim$ $100\mu m$. CMS Tracker shown in Fig. 3.10 contains 66 Million pixels, 10 million strips. The momentum resolution can be defined as:

$$\frac{\Delta p}{p} \approx 0.12 \left(\frac{pitch}{100\mu m}\right)^{1} \left(\frac{1.1m}{L}\right)^{2} \left(\frac{4T}{B}\right)^{1} \left(\frac{p}{1TeV}\right) \tag{3.2}$$

The strong magnetic field and excellent position resolution of the silicon tracker enable the transverse momentum (p_T) of a muon matched to a reconstructed track to be measured with a resolution of approximately 0.7% for p_T of 1 GeV. The pixel detector, with its excellent spatial resolution and low occupancy, enables the separation of B^+ decay vertices from the primary interaction vertex.

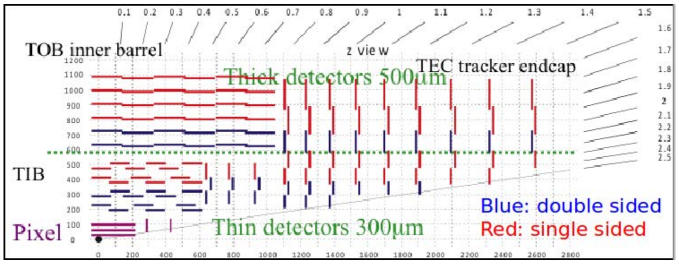

Figure 3.10: CMS Tracker [43].

3.2.2 Electromagnetic Calorimeter

In order to build up a picture of events occurring in the LHC, CMS must find the energies of emerging particles. Of particular interest are electrons and photons,

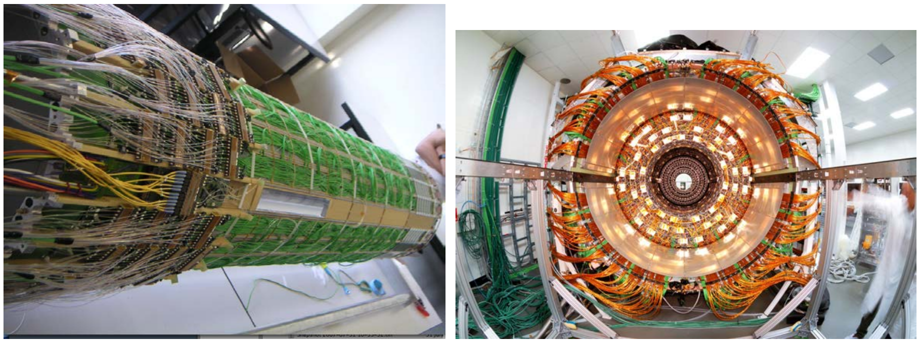

Figure 3.11: CMS Pixel Barrel plus End Caps dressed up with optical fibers [43].

because of their use in finding the Higgs boson and other new physics.

These particles are measured using an electromagnetic calorimeter (ECAL) as shown in Fig. 3.12 (left) at construction. But to find them with the necessary precision in the very strict conditions of the LHC - a high magnetic field, high levels of radiation and only 25 nanoseconds between collisions - required very particular detector materials.

Lead tungstate crystal is made primarily of metal and is heavier than stainless steel, but with a touch of oxygen in this crystalline form it is highly transparent and scintillates when electrons and photons pass through it. This means it produces light in proportion to the particles energy. These high-density crystals produce light in fast, short, well-defined photon bursts that allow for a precise, fast and fairly compact detector. Some of the crystal properties are tabulated in Table 3.13.

Photodetectors that have been especially designed to work within the high magnetic field, are also glued onto the back of each of the crystals to detect the scintillation light and convert it to an electrical signal that is amplified and sent for

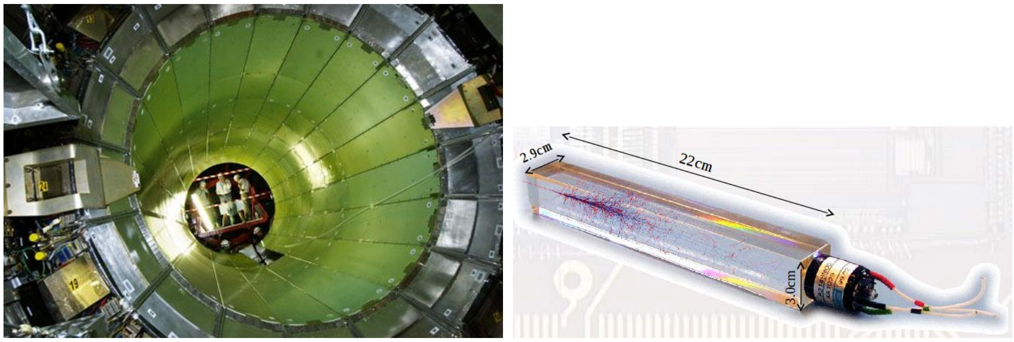

Figure 3.12: CMS ECAL during construction is shown on left and ECAL Endcap (EE) Crystal equipped with a glued Vacuum PhotoTriode (VPT) is shown on right [43].

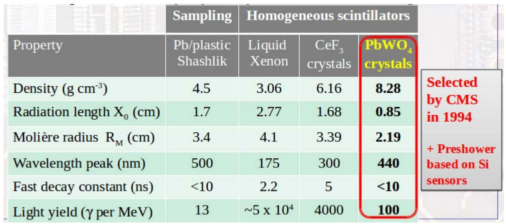

	Sampling	Homogeneous scintillators		
Property	Pb/plastic Shashlik	Liquid Xenon	CeF_3 crystals	$PbWO_4$ crystals
Density (g cm^{-3})	4.5	3.06	6.16	**8.28**
Radiation length X_0 (cm)	1.7	2.77	1.68	**0.85**
Molière radius R_M (cm)	3.4	4.1	3.39	**2.19**
Wavelength peak (nm)	500	175	300	**440**
Fast decay constant (ns)	<10	2.2	5	**<10**
Light yield (γ per MeV)	13	~5 x 10^4	4000	**100**

Selected by CMS in 1994

+ Preshower based on Si sensors

Figure 3.13: Properties of Lead tungstate crystal, which is used in the CMS ECAL [43].

analysis.

The ECAL is divided into Barrel (EB), Endcaps (EE), Endcap preShower(ES) partitions. ECAL forms a layer between the tracker and the HCAL. The cylindrical barrel consists of 61,200 crystals formed into 36 supermodules, each weighing around three tonnes and containing 1700 crystals. The flat ECAL endcaps seal off the barrel at either end and are made up of almost 15,000 further crystals.

For extra spatial precision, the ECAL also contains Preshower detectors that sit in front of the endcaps. These allow CMS to distinguish between single high-energy photons (often signs of exciting physics) and the less interesting close pairs of low-energy photons.

The CMS ECAL has,

- crystals each weigh 1.5kg but with a volume roughly equal to that of a small coffee cup,
- contains nearly 80,000 such crystals, each of which took two days to grow.

Homogeneous $PbWO_4$ generates showers & produces signal. Incident electron/photon generates EM shower (spread laterally over several crystals) in the heavy $PbWO_4$ material.

- Charged particles in the shower produce scintillation light isotropically
- Amount of scintillation light is proportional to incident particle energy
- Scintillation light detected by photodetectors with internal amplification:Silicon Avalanche PhotoDiodes - APDs (in EB) or Vacuum PhotoTriodes - VPTs (in EE)

ECAL Endcap (EE) Crystal equipped with a glued Vacuum PhotoTriode (VPT) is shown in Fig. 3.12 (right). $PbWO_4$ crystals are transparent to the entire scintillation emission spectrum.

Below are the ECAL in terms of numbers:

Barrel (EB): $|\eta| < 1.48$**:**

- 36 Supermodules: 1700 crystals, (1 supermodule = 4 modules):61200 crystals total, of 17 shapes.
- $(2.2 \times 2.2 \times 23\ cm^3) \sim 26X_0$

Endcaps (EE): $1.48 < |\eta| < 3.0$

- 4 Dees (2 per endcap): 3662 crystals,(mostly in $5 times 5$ supercrystals):14648 crystals total, of 1 shape
- $(3.0 \times 3.0 \times 22\ cm^3) \sim 25X_0$

Preshower (ES): $1.65 < |\eta| < 2.6$

- 4 planes (2 per endcap): 1072 Si sensors, 1 sensor $= 6.3 \times 6.3 \times 0.032\ cm^3$, 32 strips, 137216 strips total, $2X_0 + 1X_0$ of Pb interspersed with Si strips
- $1.90 \times 61\ mm^2$ x-y view

Ecal energy resolution (σ_E/E) for $e^{\pm}/\gamma$ quantified as:

$$\frac{\sigma_E}{E} = \frac{A}{\sqrt{E}} \oplus \frac{B}{E} \oplus C \tag{3.3}$$

where A = Stochastic term(quantifies effects of energy fluctuations)

B = Noise term(quantifies electronics and/or pileup noise)

C = Constant term (quality of construction, stability, uniformity).

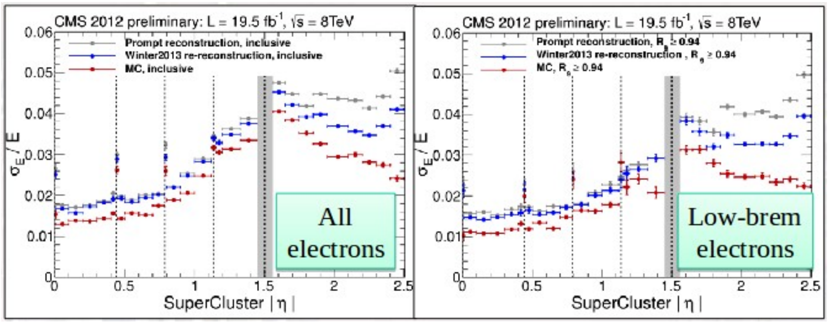

Figure 3.14: ECAL energy resolution [27].

ECAL energy resolution is shown in Fig. 3.14. Electron energy resolution is derived from $Z \rightarrow e^+e^-$ width. There is $\sim 1.2\%$ energy resolution for low bremsstrahlung electrons in the central barrel region [27].

For a detailed account of the ECAL detector see CMS ECAL Technical Design Report [30, 31].

3.2.3 Hadronic Calorimeter

All parts of HCAL are Sampling Calorimeters. Below are the criteria for design of HCAL in CMS:

- Hermetic and compact able to fit within the CMS solenoid up to $|\eta| < 3$
- Large dynamic range, coupled with excellent linearity, to > 1 TeV for jets
- Provide triggering information; e.g. particle ID, energy, isolation
- Radiation tolerant to expected dose rates and cumulative doses
- Reasonable energy resolution with depth segmentation →sampling calo.

The Hadron Calorimeter (HCAL) measures the energy of hadrons, particles made of quarks and gluons (for example protons, neutrons, pions and kaons). Additionally it provides indirect measurement of the presence of non-interacting, uncharged particles such as neutrinos.

Measuring these particles is important as they can tell us if new particles such as the Higgs boson or supersymmetric particles (much heavier versions of the standard particles we know) have been formed.

As these particles decay they may produce new particles that do not leave record of their presence in any part of the CMS detector. To spot these the HCAL must be hermetic, that is make sure it captures, to the extent possible, every particle emerging from the collisions. This way if we see particles shoot out one side of the detector, but not the other, with an imbalance in the momentum and energy (measured in the sideways transverse direction relative to the beam line), we can deduce that we are producing invisible particles.

To ensure that we are seeing something new, rather than just letting familiar particles escape undetected, layers of the HCAL were built in a staggered fashion so that there are no gaps in direct lines that a familiar particle might escape through. HCAL is less constrained by the physics processes. Good energy resolution is less important, Emphasis is laid on hermeticity to ensure a good missing transverse energy (MET) measurement. Hermetic hadronic calorimeters surround the intersection region up to $|\eta| = 4.7$ allowing tagging of forward jets and measurement of MET. Extending from $|\eta| = 3$ to $|\eta| = 5$ improves resolution of MET by a factor 3.

The HCAL is a sampling calorimeter meaning it finds a particles position, energy and arrival time using alternating layers of absorber and fluorescent scintillator materials that produce a rapid light pulse when the particle passes through. Special optic fibers collect up this light and feed it into readout boxes where photodetectors amplify the signal. When the amount of light in a given region is summed up over many layers of tiles in depth, called a tower, this total amount of light is a measure of a particles energy.

As the HCAL is massive and thick, fitting it into compact CMS was a challenge, as the cascades of particles produced when a hadron hits the dense absorber material (known as showers) are large, and the minimum amount of material needed to contain and measure them is about one meter.

To accomplish this feat, the HCAL is organized into barrel (HB and HO), endcap (HE) and forward (HF) sections. There are 36 barrel wedges, each weighing 26 tonnes. These form the last layer of detector inside the magnet coil whilst a few additional layers, the outer barrel (HO), sit outside the coil, ensuring no energy leaks out the back of the HB undetected. Similarly, 36 endcap wedges measure particle energies as they emerge through the ends of the solenoid magnet.

Lastly, the two hadronic forward calorimeters (HF) are positioned at either end of CMS, to pick up the myriad particles coming out of the collision region at shallow angles relative to the beam line. These receive the bulk of the particle energy contained in the collision so must be very resistant to radiation and use different materials to the other parts of the HCAL.

The CMS HCAL:

- Copper plates interleaved with plastic scintillators with embedded wavelength-shifting (WLS) fibers (eventually used brass (70% Cu, 30% Zn) absorber)
- Light channeled using clear fibers, to photodetectors at the ends of the barrel
- For HE, the initial design was rather ambitious
    - Cu absorber interleaved with $2 \times 2 \times 0.04\ cm^3$ Si sensors → $360m^2$ of Si (eventually used similar structure to HB brass + scintillator + WLS)

- For HF (outside the solenoid), the emphasis was on radiation hardness
  - Steel plates interleaved with parallel-plate chambers (eventually used steel absorber with Cerenkov-producing quartz fibers)

For a detailed account of the HCAL detector see:CMS HCAL Technical Design Report [32].

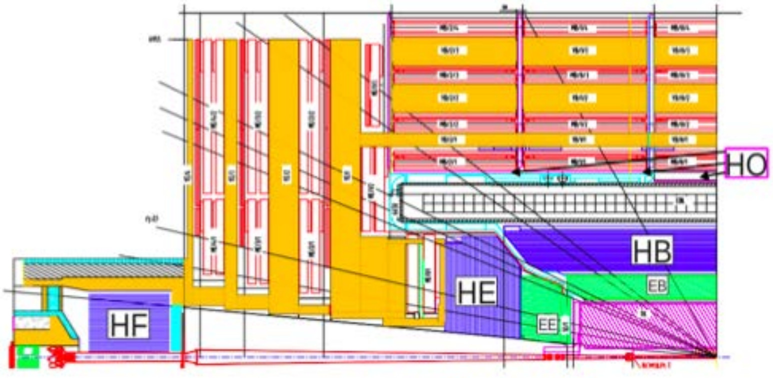

$$\frac{\sigma_E}{E}(\%) \sim \frac{100-150\%}{\sqrt{E}}$$

Figure 3.15: CMS HCAL [43].

3.2.3.1 HCAL Sampling Calorimeter

The CMS barrel and endcap sampling calorimeters are made of repeating layers of dense absorber and tiles of plastic scintillator. When a hadronic particle hits a plate of absorber, in this case brass or steel, an interaction can occur producing numerous secondary particles. As these secondary particles flow through successive layers of absorber they too can interact and a cascade or shower of particles results.

As this shower develops, the particles pass through the alternating layers of active scintillation material causing them to emit blue-violet light. Within each tile tiny optical wavelength-shifting fibers, with a diameter of less than 1mm, absorb this light. These shift the blue-violet light into the green region of the spectrum, and clear optic cables then carry the green light away to readout boxes located at strategic locations within the HCAL volume.

A megatile is a layer of tiles whose sizes depend on their spatial location and orientation relative to the collision, chosen so that each receives roughly the same number of particles. Optic fibers fit into grooves cut into the individual tiles. Because the light picked up gives a measure of energy, the gaps between tiles must be filled with a reflective paint to ensure that light produced in each tile cannot escape into others and vice versa.

The optical signals arrive at the readout boxes from megatile layers. There, signals from successive tiles, one behind the other, are then added optically to form towers. This optical summation covers the path of the particle through the HCAL and is a measure of its energy and/or can be an indicator of particle type.

These summed optical signals are converted into fast electronic signals by photosensors called Hybrid Photodiodes (HPDs). Special electronics then integrates and encodes these signals and sends them to the data acquisition system for purposes of event triggering and event reconstruction.

3.2.3.2 Hybrid Photodiodes (HPDs)

HPDs are photodetectors configured especially for CMS that can operate in a high magnetic field and give an amplified response, in proportion to the original signal, for a large range of particle energies. The HPDs are housed in special readout boxes within the calorimeter volume. Light signals from the calorimeter megatiles are delivered to the HPDs by special fiber-optic waveguides.

The light-sensitive surface of a HPD is called the photocathode, which converts light into electrons by the photoelectric effect. Inside the HPD, these low-energy electrons are quickly accelerated across a narrow gap of a few millimeters onto a silicon diode target. The target is divided up into 19 pixels each of which can generate its own amplified electronic signal when the accelerated electrons strike it. This allows the detection and amplification of up to 19 separate calorimetry signals with one HPD. The electronic signals are then sampled for each collision, digitized using special HCAL-designed integrated circuits called QIE chips (Charge Integration and Encode) and sent to the trigger and data acquisition system for analysis. The HPDs amplify the calorimetry signals approximately 2000 times, and 420 of these devices are used in CMS.

Fig. 3.16 shows the HCAL Barrel and Endcap sampling layers. Forward HCAL measures Cerenkov light in quartz fibers.

- Forward (HF): $3.0 < |\eta| < 5.0$, 18 wedges per end
    - Grooved steel plates, 5mm thick, 165cm long $\rightarrow \sim 10\lambda$
    - $\sim$square grid of holes spaced 5mm apart

- 1mm diameter fibers (600mm quartz core + cladding + buffer)
- 2 fiber lengths (read out separately) to distinguish e/g from hadron showers:
  - Half are 165cm long
  - Other half start after a depth of 22cm

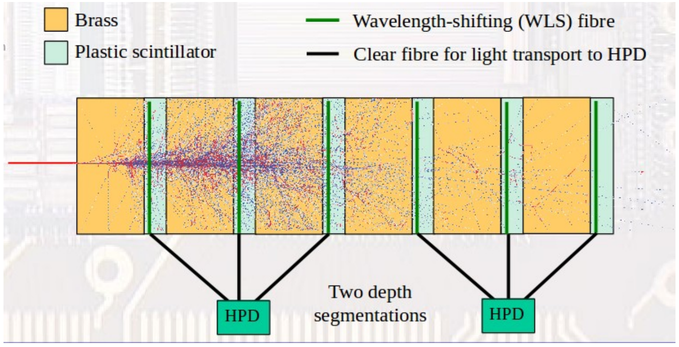

Figure 3.16: HCAL Barrel and Endcap sampling layers [43].

In the CMS HCAL, the tower size: $\Delta\eta \times \Delta\Phi = 0.087 \times 0.087$. The performance of the HCAL can be studied by plotting the calorimeter response as a function of track p_T, and MET resolution measurements.

$$HCAL_{response} = E_{HCAL}/p_{track} \tag{3.4}$$

$\sqrt{s} = 7$ TeV minimum-bias data is considered. No signal in ECAL; Isolated tracks $p_T > 5$ GeV, cone-based isolation at HCAL surface considered. Missing ET (MET) is calculated using a combination of measurements in all calorimeters (CaloMET) and also the Tracking detectors (Particle Flow - PF_MET and Tracker-

Corrected - TC_MET). Differences in responses & non-linearities necessitate E_T and η-dependent corrections. Special filters developed to eliminate noise, which could otherwise affect MET performance.

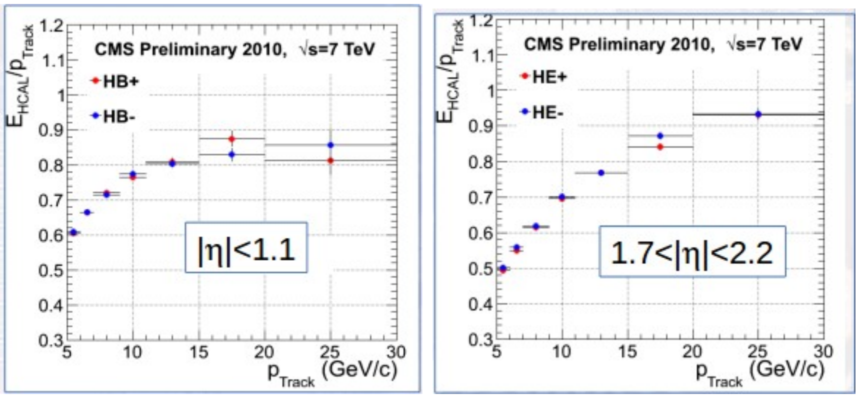

Figure 3.17: HCAL response in two pseudorapidity regions: for $|\eta| < 1.1$ is shown on the left plot and for $1.7 < |\eta| < 2.2$ is on the right [27].

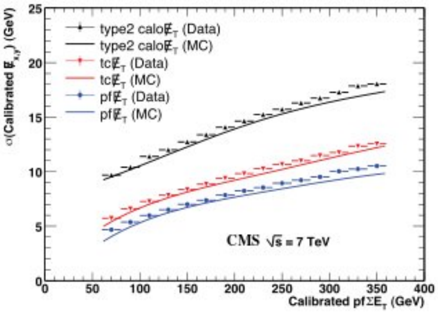

Figure 3.18: Resolution for the calibrated MET for multijet events with two jets with $p_T > 25$ GeV [27].

Fig. 3.17 shows HCAL response in two pseudorapidity regions. Fig. 3.18 shows the resolution for the calibrated MET for multijet events with two jets with $p_T > 25$ GeV [27]. The Particle Flow technique gives a substantial improvement in Jet energy and MET resolutions.

3.2.4 Muon reconstruction system

CMS contains three different muon subdetectors: drift tubes (DT), resistive plate chambers (RPC) and cathode strip chambers (CSC). Muon reconstruction steps are shown in Fig. 3.19.

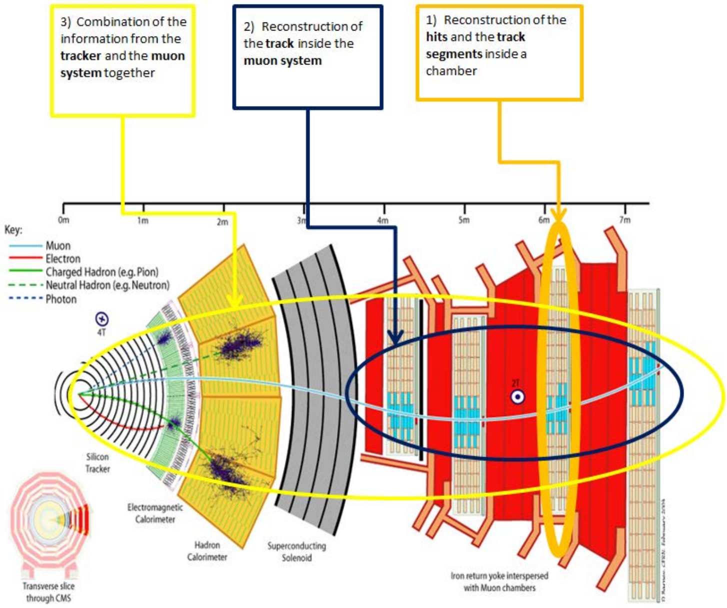

Figure 3.19: Overview of the Muon reconstruction [43].

The main subdetectors used in this analysis are the silicon tracker and the muon systems. The inner tracker measures charged particles within the pseudorapidity range $|\eta| < 2.5$. The CMS high quality central tracking system gives accurate momentum measurements. The tracker is composed of layers totaling 66 million $100{\times}150\mu m^2$ strips with pitch ranging from 80 to 183 μm silicon pixels and 9.6 million silicon immersed in a 3.8 T axial magnetic field, that provide precision tracking of charged particles. Muons are measured in the pseudorapidity range $|\eta| < 2.4$, with detection planes made using three technologies: drift tubes, cathode strip chambers, and resistive plate chambers.

The muon system performs three main tasks: triggering on muons, identifying muons, and improving the momentum measurement and charge determination of high p_T muons. Drift tube (DT) chambers and cathode strip chambers (CSC) detect muons in the η regions of $|eta| < 1.2$ and 0.9< $|\eta|$ <2.4, respectively, and are complemented by a system of resistive plate chambers (RPC) covering the range of $|\eta|$ <1.6. The use of these different technologies defines three regions in the detector, referred to as barrel ($|\eta|$ <0.9), overlap (0.9< $|\eta|$ <1.2), and endcap (1.2< $|\eta|$ <2.4). Muon energy deposits in the electromagnetic calorimeter (ECAL), hadronic calorimeter (HCAL), and outer hadronic calorimeter (HO) are also used for muon identification purposes.

For the measurement of muons the single most important aspect is the choice of magnetic field configuration. CMS magnetic field configuration can be seen in Fig. 3.20. The requirement of a good momentum resolution, specified to be $\sigma(p_T)/p_T \sim$ 1% at 100 GeV/c and $\sim$ 10% at 1 TeV/c [28], without making stringent demands on spatial resolution and the alignment of muon chambers leads to the choice of a high magnetic field. CMS chose a high-field solenoid. The magnetic flux generated by the central field is large enough to saturate a sufficient amount of steel in the return yoke to allow the installation of four muon stations. This provides a good level of redundancy in the measurement of muons. The favorable length to radius ratio allows efficient muon measurement up to pseudorapidity of $|\eta| < 2.4$. The strong magnetic field also enables an efficient first-level trigger with an acceptable rate.

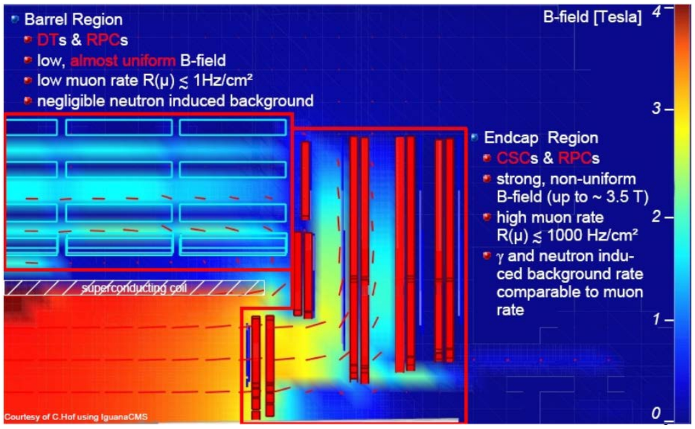

Figure 3.20: CMS Magnetic field configuration, Reference [28]

The CMS experiment uses a two-level trigger system. The Level-1 trigger, composed of custom hardware processors, selects events of interest using information from the calorimeters and muon detectors and reduces the read-out rate from the 20 MHz bunch-crossing frequency to a maximum of 100 kHz [33]. The high-level trigger (HLT) is software-based and further decreases the recorded event rate to around 300 Hz by using the full event information, including that from the inner tracker [34].

3.2.4.1 Muon track momentum in B field

When a charged particle such as muon enters into a magnetic field, work is done by the magnetic field on the muon to change its direction. The bending radius of the muon track is given by:

$$r = \frac{l^2}{8s} + \frac{s}{2} \tag{3.5}$$

Where l is the cord length of the track in the B field and s the sagitta as shown in Fig. 3.21. For a relatively high p_T, the s is small, then the track radius becomes $r \sim \frac{l^2}{8s}$. In CMS the tracker ends at 1.1m radius while the first layer of the DT is just outside the coil. The track transverse momentum is given by:

$$p_T \propto 0.3Br \tag{3.6}$$

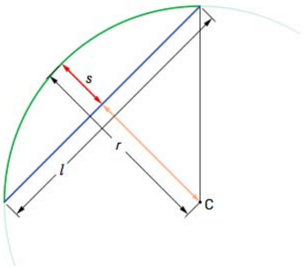

Figure 3.21: Particle radius in B field [43].

3.2.4.2 Muon reconstruction and Identification

In the standard CMS reconstruction for pp collisions [35, 28], tracks are first reconstructed independently in the inner tracker and in the muon system. The muon reconstruction chain starts with the ”local reconstruction”. First, hits in DTs, CSCs and RPCs are reconstructed from digitized electronics signals. Hits within each DT and CSC chamber are then matched to form ”segments” (track stubs). The production of hits and segments in muon sub-systems is shown in Fig. 3.22. Based on these objects, two reconstruction approaches are used:

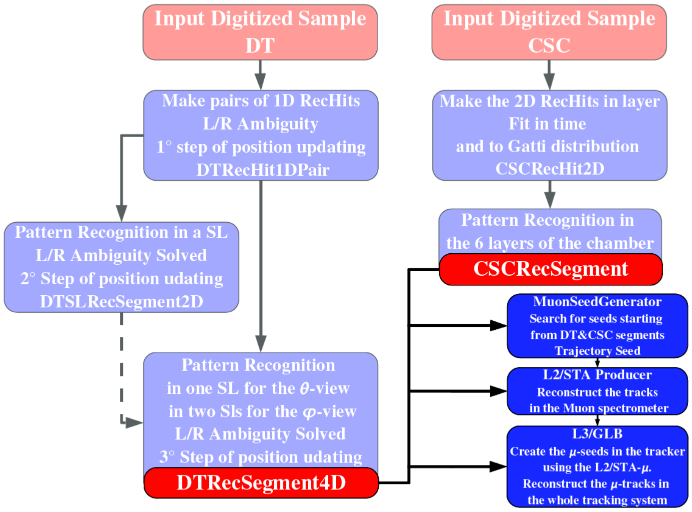

Figure 3.22: Muon track seed generation steps [43].

- Global Muon reconstruction (outside-in). For each standalone-muon track, a matching tracker track is found by comparing parameters of the two tracks propagated onto a common surface. A global-muon track is fitted combining hits from the tracker track and standalone-muon track, using the Kalman-filter technique [36]. At large transverse momenta, $p_T \gtrsim 200$ GeV/c, the global-muon fit can improve the momentum resolution compared to the tracker-only fit [35, 28].

- Tracker Muon reconstruction (inside-out). In this approach, all tracker tracks with $p_T > 0.5$ GeV/c and total momentum $p > 2.5$ GeV/c are considered as possible muon candidates and are extrapolated to the muon system taking into account the magnetic field, the average expected energy losses, and multiple Coulomb scattering in the detector material. If at least one muon segment (i.e., a short track stub made of DT or CSC hits) matches the extrapolated track, the corresponding tracker track qualifies as a Tracker Muon. Track-to-segment matching is performed in a local (chamber) coordinate system, where local x is the best-measured coordinate (in the $r - \phi$ plane) and local y is the coordinate orthogonal to it. The extrapolated track and the segment are considered to be matched if the distance between them in local x is less than 3 cm or if the value of the pull for local x is less than 4, where the pull is defined as the difference between the position of the matched segment and the position of the extrapolated track, divided by their combined uncertainties [35].

Tracker Muon reconstruction is more efficient than the Global Muon reconstruction at low momenta, $p \lesssim 5$ GeV/c, because it requires only a single muon segment in the muon system, whereas Global Muon reconstruction is designed to have high efficiency for muons penetrating through more than one muon station and typically requires segments in at least two muon stations. Owing to the high efficiency of the tracker-track reconstruction [65] and the very high efficiency of reconstructing segments in the muon system, about 99% of muons produced in pp collisions within the geometrical acceptance of the muon system and having sufficiently high momentum are reconstructed either as a Global Muon or a Tracker Muon, and very often as both. Candidates found both by the Global Muon and the Tracker Muon approaches that share the same tracker track are merged into a single candidate. Muons reconstructed only as standalone muon tracks have worse momentum resolution and higher admixture of cosmic-ray muons than the Global and Tracker Muons and are usually not used in physics analyses. The combination of different algorithms provides robust and efficient muon reconstruction. Physics analyses can set the desired balance between identification efficiency and purity by applying a selection based on various muon identification variables. The performance of three basic muon identification algorithms is discussed below:

- Soft Muon selection. This selection requires the candidate to be a Tracker Muon, with the additional requirement that a muon segment is matched in both x and y coordinates with the extrapolated tracker track, such that the pull for local x and y is less than 3. Segments that form a better match with a different tracker track are not considered. These additional requirements are optimized for low $p_T(< 10\text{GeV/c})$ muons. This selection is used in quarkonia and B-physics analyses in CMS [38].
- Tight Muon selection. For this selection, the candidate must be reconstructed outside in as a Global Muon with the $\chi^2/d.o.f.$ of the global-muon track fit less than 10 and at least one muon chamber hit included in the global-muon track fit. In addition, its corresponding tracker track is required to be matched to

muon segments in at least two muon stations (this implies that the muon is also reconstructed inside out as a Tracker Muon), use more than 10 inner-tracker hits (including at least one pixel hit), and have a transverse impact parameter $|d_{xy}| < 2$ mm with respect to the primary vertex. With this selection, the rate of muons from decays in flight is significantly reduced, at the price of a few percent loss in efficiency for prompt muons such as those from W and Z decays. The Tight Muon selection is used in many physics analyses in CMS, in particular in the measurements of inclusive W and Z cross sections [39].

- Particle-Flow Muon selection. The CMS particle-flow event reconstruction algorithm [40]combines information from all CMS subdetectors to identify and reconstruct individual particles like electrons, hadrons or muons. For muons, the particle-flow approach applies particular selection criteria to the muon candidates reconstructed with the Global and Tracker Muon algorithms described above. Depending on the environment of the muon (for example, whether it is isolated or not) the selection criteria are adjusted making use of information from other subdetectors (for example, the energy deposition in the calorimeters). In general, the selection is optimized in order to identify muons within jets with high efficiency, while maintaining a low rate for the misidentification of charged hadrons as muons. The details of the particle-flow muon selection are described in Ref. [41].

The default algorithm for muon momentum assignment in CMS is called the sigma switch. This algorithm chooses from the momentum estimates given by the tracker-only fit and by the global fit. The global fit is chosen when both fits yield muon p_T above 200 GeV/c and give the charge-to-momentum ratios q/p that agree to within $2\sigma_{q/p}$ of the tracker-only fit; in all other cases the tracker-only fit is taken. In addition, CMS has developed specialized algorithms for high p_T muon reconstruction and momentum assignment. As the muon passes through the steel of the magnet return yoke, multiple scattering and radiative processes can alter the muon trajectory. While the former is not so important for high-momentum muons, the latter can result in large energy losses and can also produce electromagnetic showers giving rise to additional hits in the muon chambers. As a consequence, the estimate of the muon momentum at the production vertex can be significantly different from its true value. Therefore, several different strategies for including information from the muon system have been developed and studied using cosmic rays [35]:

- Tracker-Plus-First-Muon-Station (TPFMS) fit. This algorithm refits the global-muon track ignoring hits in all muon stations except the innermost one containing hits, for reduced sensitivity to possible showering deeper in the muon system.
- The Picky fit. This algorithm again starts with the hit list of the global-muon track, but, in chambers appearing to have hits from showers (determined by the hit occupancy of the chamber), retains only the hits that, based on a χ^2 comparison, are compatible with the extrapolated trajectory.

To further improve the resolution at high p_T, mainly by reducing the tails of the momentum resolution distribution, combinations of the above can be used. In particular, the Tune P algorithm chooses, on a muon-by-muon basis, between the tracker-only, TPFMS, and Picky fits. The algorithm starts with the Picky fit, then switches to the tracker-only fit if the goodness of fit of the latter is significantly better. Then it compares the goodness of fit of the chosen track with that of TPFMS; TPFMS is chosen if it is found to be better. For high p_T muons, TPFMS and Picky algorithms are selected by Tune P in most of the cases, in approximately equal amounts, while the tracker-only fit is selected only in a few percent of events.

A more detailed description of the CMS detector can be found in [57].

3.3 Summary

A brief summary of LHC accelator parameters and run conditions during 2011-2012 data taking period are presented. Exclusive details of the CMS experiment and its sub-detectors geometry are discussed. Particle tracks reconstruction algorithms, and methods of particle identification, triggers are presented.

CHAPTER 4
OBSERVATION AND THE BRANCHING FRACTION MEASUREMENT OF $B^+ \to \psi(2S)\phi K^+$

4.1 Introduction

The flavor sector is that part of the standard model (SM) that arises from the interplay of quark weak gauge couplings and quark-Higgs couplings. The misalignment of these in the mass eigenstate basis gives rise to the Cabbibo-Kobayashi-Maskawa (CKM) matrix that encodes the physics of the weak flavor-changing decays of quarks. There are three generations of quarks and a very wide range of quark couplings and masses; however, we observe hadrons, not quarks. The top quark is so massive that it decays on timescales shorter than the typical hadronization time into other quarks. Bottom and charm quarks are therefore the most massive quarks that can comprise observable particles, and these are termed the heavy flavor hadrons.

The production of heavy flavor hadrons tests QCD theory, and spectroscopy explores the interactions and dynamics of quarks inside of hadrons. Lifetimes and branching fractions straddle the boundary of weak decays and hadronic physics effects.

4.2 Branching ratio measurements

The measurement of branching ratio $\mathcal{B}$ is very simple: the total number of events observed in a given final state $N^{\text{obs}}_{Q\bar{Q}\to f}$ is proportional to the total number of events produced $N^{\text{prod}}_{Q\bar{Q}}$ for that particular resonance:

$$N^{\mathrm{obs}}_{Q\bar{Q}\to\mathrm{f}} = \mathrm{eff} \times N^{\mathrm{prod}}_{Q\bar{Q}} \times \mathcal{B}(Q\bar{Q} \to \mathrm{f}), \tag{4.1}$$

$N^{\mathrm{prod}}_{Q\bar{Q}}$ in turn needs to be measured by counting some specific events. In most cases, depending on the process under study and the analysis strategy, $N^{\mathrm{prod}}_{Q\bar{Q}}$ is calculated from the number of events observed in a given "reference" final state $N^{\mathrm{obs}}_{Q\bar{Q}\to\mathrm{Ref}}$:

$$N^{\mathrm{prod}}_{Q\bar{Q}} = \frac{N^{\mathrm{obs}}_{Q\bar{Q}\to\mathrm{Ref}}}{\mathrm{eff}'\,\mathcal{B}_{\mathrm{Ref}}}.$$

The reported value of $\mathcal{B}(Q\bar{Q} \to \mathrm{f})$ will therefore use $\mathcal{B}_{\mathrm{Ref}}$ as reported by some previous experiment:

$$\mathcal{B}(Q\bar{Q} \to \mathrm{f}) = \frac{N^{\mathrm{obs}}_{Q\bar{Q}\to\mathrm{f}}}{N^{\mathrm{obs}}_{Q\bar{Q}\to\mathrm{Ref}}}\,\frac{\mathrm{eff}'}{\mathrm{eff}}\,\mathcal{B}_{\mathrm{Ref}}. \tag{4.2}$$

As discussed in [44], there are a number of potentially dangerous consequences in this procedure. First of all different experiments might use the same reference mode, so their values of $\mathcal{B}$ are not independent. Even worse, the $\mathcal{B}(Q\bar{Q} \to \mathrm{f})$ reported in Eq.(4.2) will also be (mistakenly) correlated to the normalization Ref chosen by the previous experiment(s) where $\mathcal{B}_{\mathrm{Ref}}$ had been measured, and ultimately may depend on some other branching ratio $\mathcal{B}'_{\mathrm{Ref}'}$. Such hidden correlations are hard to identify and can have pernicious consequences on the evaluation of $\mathcal{B}'$ based on independent measurements from different experiments.

For precision determination of branching ratios or partial widths, it is important to know the normalization used in each measurement and to quote explicitly the quantity that is indeed directly measured by each experiment

$$\frac{\mathcal{B}(Q\bar{Q} \to \mathrm{f})}{\mathcal{B}_{\mathrm{Ref}}} = \frac{N^{\mathrm{obs}}_{Q\bar{Q}\to\mathrm{f}}}{N^{\mathrm{obs}}_{Q\bar{Q}\to\mathrm{Ref}}} \frac{\mathrm{eff}'}{\mathrm{eff}}, \tag{4.3}$$

i.e. the ratio or product of branching ratios (even of different particles), which is most directly related to the event yield. Many experiments could also provide measurements of ratios of branching ratios

$$R_{\mathcal{B}}(f/f') = \frac{\mathcal{B}(Q\bar{Q} \to \mathrm{f})}{\mathcal{B}(Q\bar{Q} \to \mathrm{f}')}, \tag{4.4}$$

which do not depend on the normalization, and usually a number of other systematics cancel.

4.3 Experimental Characteristics of Flavor Physics at the LHC

The most appealing feature of hadron machines as tools to study b physics is their very high cross section for $b\bar{b}$ production. The LHC is a copious source of b hadrons with a production cross section several orders of magnitude greater than that of the Tevatron.

The feature of heavy quarks that makes it possible to observe meaningful levels of signal among the enormous backgrounds is the long lifetime of $\simeq 1.5$ ps [45] for b hadrons, so that these boosted hadrons are likely to decay at secondary vertices a significant distance on the order of a millimeter from the beamline and interaction point of the pp beams. The reconstruction of these secondary vertices, or the observation of a charged particle track inconsistent with its trace back to the beamline is a powerful signature in identifying heavy flavor decays.

A cornerstone of b physics in hadron collider experiments is the signature provided by $B \to J/\psi X$ or $\psi^{'} X$, with a branching fraction of approximately 1% followed by the decay of the ψ meson into $\mu^+\mu^-$ or e^+e^-. While the product branching fraction of $B \to J/\psi \to \mu^+\mu^-$ is only $\simeq 6 \times 10^{-4}$, these decays provide a distinctive signature and offer a wealth of information about the $b \to c\bar{c}s$ transition. These decays also provide triggering and tagging for the study of global properties of b hadrons.

Due to huge event rates, effective triggers and quality detectors are essential for extracting physics results. Heavy flavor analyses typically require a detector with strengths in the three aspects of the experiments: triggering, reconstruction, and flavor tagging. Heavy quarks are produced in hadronic colliders preferentially at small polar angles θ (with respect to the beam axis) and at large absolute values of pseudorapidity $\eta \equiv -\ln[tan(\theta/2)]$. CMS experiment employed muons from $b \to \mu$ for triggering. With a muon acceptance window in rapidity $|\eta| < 2.4$, The CMS detector has a distinct advantage in inclusive muon and dimuon triggering and studies. With less material before the first set of muon chambers, the CMS detector allows the study of dimuons with lower momenta.

4.3.1 B meson decays

The large dataset accumulated at the LHC provides us with opportunities to study non-pertubative Quantum-Chromo-Dynamics (QCD) theory via rare decays at the bottom sector; for example, the Okubo-Zweig-Iizuka (OZI) suppressed process.

Another prominent feature in an OZI suppressed process is that other new phenomena such as exotic structure, can be produced and spotted in these decays; for example, the $J/\psi\phi$ structures observed in $B^+ \to J/\psi\phi K^+$ decays [46, 47, 48, 49, 50, 51, 52]. In this chapter, an observation of a similar decay of $B^+ \to \psi(2S)\phi K^+$ is reported, where charge conjugate decay modes are implied throughout. The B meson decays through the weak interaction.

4.3.2 Exclusive $B^+ \to \psi(2S)\phi K^+$ decay

Decays into final states containing a ϕ meson are particularly interesting because the decay of a b quark to a charm quark associates with the production of an $s\bar{s}$ pair from vacuum. The study of B meson weak decays is of high interest in heavy flavor physics and exotic meson spectroscopy. In particular, much attention has been paid to the two-body charmless hadronic B decays, but there are relatively fewer discussions on the three-body decays with a charmed meson, strange mesons, such as the modes with one charmed-meson $\psi(2S)$ and two strange-mesons ϕ, K^+. $B^+ \to \psi(2S)\phi K^+$ has not yet been observed. The analysis is not only interesting due to the observation of a never-before-seen process, which may give input to the Quark Model, but because $\psi(2S)\phi$ is a search channel for new exotic structures such as the $X(3872)$ and the $Y(4140)$. The discovery of these structures has sparked a renewed interest in exotic searches in the charmonium sector, and is a growing area of interest in CMS.

4.4 Reference channel considered for BF measurement

Charged B mesons arising from $b\bar{b}$ pairs produced in LHC collisions can be reconstructed exclusively from their decay to $\psi 2SK^{\pm}$ (branching fraction 0.0627% [53]) using the $\psi(2S)$ decay to a di-muon final state (branching fraction 0.77%). CMS can reconstruct $B^{\pm}$ mesons decaying to the $\psi(2S)(\mu^{+}\mu^{-})K^{\pm}$ final state with high efficiency, provided at least one muon passes the trigger requirements. The channel $B^{+} \rightarrow \psi(2S)(\mu^{+}\mu^{-})K^{+}$ is the reference for $B^{+} \rightarrow \psi(2S)\phi K^{+}$ branching fraction measurement. This measurement was conducted in 20 fb^{-1} of pp collision data collected by the CMS experiment at a center of mass energy of 8 TeV.

4.5 Monte Carlo sample

A dedicated sample of 1000k Monte Carlo (MC) $B^{+} \rightarrow \psi(2S)(\mu^{+}\mu^{-})\phi(K^{+}K^{-})K^{+}$ and 500k MC $B^{+} \rightarrow \psi(2S)(\mu^{+}\mu^{-})K^{+}$ events are used to compare the mass position and resolution with the results obtained from the data. They are generated with PYTHIA6 [54] using the EVTGEN [55] program. The signal events are produced such that every generated event contains at least one instance of the signal process with appropriate run conditions such as pileup (mutiple collisions in the same bunch crossing). Generated events are retained only if both muons from the $\psi(2S)$ have transverse momenta $p_T > 4.9$ GeV. The CMS detector is simulated with the Geant4 package [56] and the events are fully reconstructed with the same software that is used to process the data from the detector.

Unless stated otherwise, the reconstructed MC events are analyzed in exactly the same way as the data.

4.6 Data sample and trigger selections

The CMS detector [57] covers nearly the entire solid angle around the collision point with layers of tracking detectors, calorimeters, and muon chambers. The muon and tracking systems are of particular importance in the reconstruction of the B^+ candidates. Only data with both systems fully operational, and stable LHC beams are used here. The data were collected in a period of rising instantaneous luminosity at the LHC, and the trigger conditions varied considerably over this time. Consequently, the trigger selections differ depending on the period of data taking. For data periods using HLT, events passing di-muon HLT triggers with threshold 5 GeV are accepted. Some triggers are prescaled at high instantaneous luminosity. We chose unprescaled Dimuon5 PsiPrime for this analysis. Applying these requirements on the data quality and trigger to $\sqrt{s} = 8$ TeV pp collisions in 2012, provides a data sample of $19.6 fb^{-1}$. The luminosity is estimated from the bunch properties, such as the well-known Van der Meers scan method, and it has an uncertainty of 2.5% [58].

4.7 CMS Muons Types

Muon identification and reconstruction in CMS extends over the pseudorapidity range $|\eta| < 2.4$, covering a p_T range above 1 GeV. In the muon reconstruction algorithms, the following categories of muons are reconstructed as shown in Fig. 4.1.

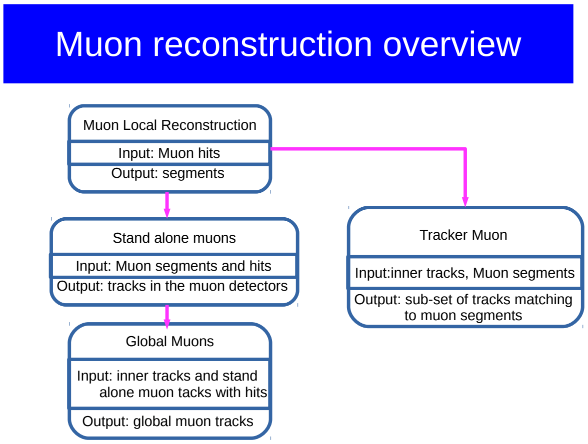

Figure 4.1: Muon reconstruction overview [43].

- Standalone Muons. In the offline reconstruction, the segments reconstructed in the muon chambers are used to generate seeds consisting of position and direction vectors and an estimate of the muon transverse momentum. These initial estimates are used as seeds for the track fits in the muon system, which are performed using segments and hits from DTs, CSCs and RPCs and are based on the Kalman filter technique. The result is a collection of reco::Track objects reconstructed in the muon spectrometer, which are referred to as standalone muons. To improve the momentum resolution, a beam-spot constraint can be applied in the fit. Two collections of standalone muons, with and without the beam-spot constraint, are available in the event record (in both RECO and AOD). A more detailed description of the reconstruction of tracks in the muon system alone can be found in Section 4 of [59].

- Global Muons. For each standalone muon track, a search for tracks matching it among those reconstructed in the inner tracking system (referred to as tracker tracks, inner tracks or silicon tracks) is performed, and the best-matching tracker track is selected. For each tracker track - standalone muon pair, the track fit using all hits in both tracks is performed, again based on the Kalman filter technique. The result is a collection of reco::Track objects referred to as global muons. More details on the reconstruction of global muons can be found in Section 5 of [59].
- Tracker Muons. An approach complementary to the global-muon reconstruction consists of considering all tracker tracks to be potential muon candidates and in checking this hypothesis by looking for compatible signatures in the calorimeters and muon system. Tracker tracks identified as muons by this method are referred to as tracker muons. A detailed description of the reconstruction of tracker muons can be found in Section 6 of [59].

The standalone muon reconstruction is entirely based on the tracks reconstructed in the Muon Chambers. The track parameters are obtained from the Muon chambers track and are extrapolated to the interaction point, taking into account multiple scattering and the energy loss in the traversed material. The standalone reconstruction covers $|\eta| < 2.5$.

The global muon reconstruction relies on combining the fitted tracks from the standalone Muon chambers and Inner Detector (ID) reconstruction, selecting the tracks to be paired on the basis of tight matching criteria to create a global muon track. Due to ID coverage, the global reconstruction covers $|\eta| < 2.5$.

A tagged muon track is formed by groups of hits in the muon detectors which are not associated with a muon chamber's track, but which are matched to inner detector tracks extrapolated to the Muon System. The reconstruction of tagged muons is of particular relevance for muons in the p_T range [3,8]GeV, as is the case for muons from J/ψ or $\psi(2S)$ decays. Because of their low p_T, they are not always fully reconstructed in the Muon System as they will not reach all muon stations. Such a reconstructed muon adopts the measured parameters of the associated ID track. The muon tagging covers $|\eta| < 2.2$.

In the current analysis, only global muons are used.

4.8 Selection criteria for signal reconstruction

In the CMS analysis framework the selection of signal candidates is performed in several stages, where each stage refines the sample obtained from the previous selection stage. The design of the analysis framework was mainly driven by CPU power and disk capacity efficiency.

A typical CMS physics analysis selects only a tiny fraction of all events. Therefore, it is extremely inefficient for each analysis to process all available data repeatedly.

Additionally, allowing many analysis jobs to access the centrally stored event puts a large load on the system and requires a large local computing farm to provide the necessary the limits of CPU power and disk capacity. These issues are circumvented by a centrally managed pre-selection, or *skim*, of events as a first stage in the analysis chain. The skim uses basic selection criteria such as mass and momentum cuts.

The skim produces a copy of events from the whole dataset that pass basic selection criteria in the form of smaller size objects (compared to raw data root files) called as *ntuples*.

The skim is usually defined to have a high signal selection efficiency. The background rejection is preferably high but of less importance in this stage. It does determine how fast the second selection stage can be optimized and performed. A single skim can be the starting sample for multiple analyses.

We summarize here the event pre-selection cuts used in this analysis:

- All kaon tracks to have $p_T > 0.5$ GeV.
- All kaon and muon tracks to have $|\eta| \leq 2.4$.
- All muon tracks to have at least 1 pixel hit and at least 5 silicon hits.
- $\mu^+\mu^-$ pair with a valid vertex fit and mass within the range $[3.4, 4.0]$ GeV.
- Three different tracks with assigned kaon mass, total charge$= \pm 1$ and mass upon combining with $\mu^+\mu^-$ in the range $[5.15, 5.45]$ GeV.
- We have two K^+K^- pairs from three charged kaon tracks. We require the mass of K^+K^- pair with lower mass to be smaller than 1.06 GeV.
- We do a vertex fit to the five tracks and constrain $\mu^+\mu^-$ to the nominal $\psi(2S)$

mass and require vertex probability $> 10^{-6}$.

The second selection stage is performed under the control of the user. The optimization of this stage is performed on the skimmed dataset and depends on the goal of the physics analysis; e.g. branching fraction measurement, possible structure analysis.

For this analysis a dedicated skim was implemented. Very loose restrictions are chosen for the skim to fully exploit the more sophisticated selection criteria available in the following selection stage. This results in a high signal efficiency but unfortunately introduces a higher rate for background events. The skim is chosen to select two types of decay modes, $B^+ \to \psi(2S)\phi K^+$ and $B^+ \to \psi(2S)K^+$. The later mode is the normalization channel.

This section describes the setup of the skim that is used in the analysis. The optimization of the selection that follows the skim is presented in Section 4.9.

The analysis is driven by the reconstruction of $\psi(2S)$ from two oppositely charged muon tracks. All muon tracks need to pass CMS standard soft muon selection criteria listed below:

- muon track should have at least 1 pixel hit and at least 5 silicon hits.
- the normalized χ^2 of muon track < 1.8.
- $|d_{xy}| < 3.0$ cm.
- $|d_z| < 30.0$ cm.
- Track matched with at least one muon segment (in any station) in both X and Y coordinates ($< 3\sigma$) and arbitrated TMOneStationTight.

We apply trigger matching [60] for the reconstructed muons. If the muon candidates for $\psi(2S)$ in our signal event pass any of the dimuon triggers, the trigger matching condition is true and the event is kept to apply additional selection cuts, discussed here. Kaon tracks are selected from reconstructed tracks with highest quality, known in CMS as *highpurity* tracks [61]. The high purity track selection is based on:

- The number of hits,
- The normalized χ^2 of the track,
- The compatibility of the track originating from a pixel vertex,
- The longitudinal track impact parameter $|d_z| < 10\sigma_z$, (where σ_z is the combined track and primary vertex uncertainty),
- $\sigma_{p_T}/p_T < 10\%$.

Below are the typical requirements for B^+ hadron reconstruction.

- All kaon tracks to have $|\eta| \leq 2.4$; all muon tracks to have $|\eta| \leq 2.0$
- All kaon tracks to have $p_T > 1.0$ GeV
- All muon tracks need to pass CMS standard soft muon selection
- we have two K^+K^- pairs and we chose the pair with invariant mass closest to the ϕ nominal mass.

For this analysis, displaced dimuon vertex and minimum (di)muon transverse momentum high level trigger is used. The B^+ signal(normalization channel) is reconstructed exclusively through the $\psi(2S)$, ϕ, and K^+mesons as shown in Fig. 4.2.

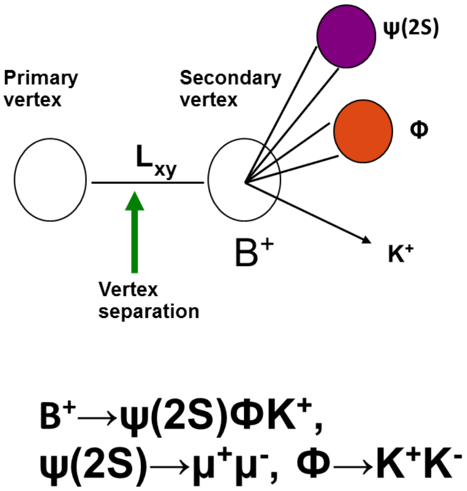

Figure 4.2: A schematic showing signal reconstruction from $\psi(2S)$, ϕ, and K^+.

Muon pairs are considered to form a $\psi(2S) \to \mu^+\mu^-$ candidate if: the pair of the muon candidate tracks fit successfully to a common vertex with vertex probability $> 0.1\%$, the dimuon pair has $p_T > 7$ GeV, and their invariant mass (calculated from the track parameters refitted by the vertexing algorithm [62] and under a muon mass hypothesis) lies within a $\pm 5\sigma$ window of ± 150 MeV of their fitted mean, that is, in the mass range 3535 - 3835 MeV. This cut is illustrated on Fig. 4.3. A maximum likelihood method is used to fit the $\psi(2S)$ mass. The signal is described using a double Gaussian with per-candidate uncertainties and background events are minimized after applying all final event selection cuts, the $\psi(2S)$ mass distibution from signal and normalization channels plotted.

Signal selection criteria are optimized, their efficiencies are noted, and background levels are estimated from data outside the signal region before we proceed to estimate the signal significance.

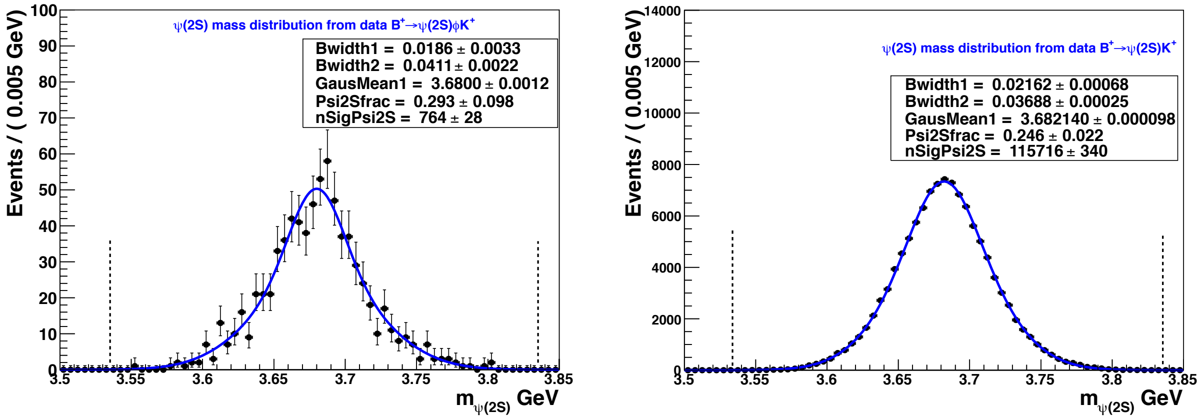

(a) $m(\psi(2S))$ from $B^+ \to \psi(2S)\phi K^+$ Decay (b) $m(\psi(2S))$ from $B^+ \to \psi(2S)K^+$ Decay

Figure 4.3: $\psi(2S)$ mass distribution for signal channel on the left and for normalization channel on the right from data passing all the event selection cuts for the B^+. Those used in the the search for B^+ candidates are subject to a tighter mass window, as shown by the dotted vertical lines. The points are data. The solid line is the result of an unbinned maximum likelihood fit to all di-muon pairs in the mass window 3500 - 3850 MeV. The signal is described using a double Gaussian with per candidate uncertainties. The given error on the fitted yield is statistical only.

4.9 Selection optimization

The resulting sample obtained from the skim becomes the input to a final event selection. This stage in the data selection uses as many signal-background discriminating variables as possible to achieve the highest possible signal sensitivity. A dedicated optimization procedure is used to maximize the significance level of the selected data set. Here, the significance level reflects the sensitivity to the discovery of the $B^+ \to \psi(2S)\phi K^+$ signal, which is the primary goal of this analysis. A set of optimized rectangular box cuts is produced for reconstructed decay chain. Here, rectangular means that one demands that certain measured quantities in the event lie in well-defined ranges which do not vary with other quantities in the event.

The optimization process aims to find the highest significance level in the multi-variable phase space. We first find an appropriate definition of the significance level. Two commonly used functions to define the significance level are,

$$\frac{S}{\sqrt{S+B}}, \tag{4.5}$$

and

$$\frac{S}{\sqrt{B}}. \tag{4.6}$$

Here S is the number of selected signal events in a given dataset, and B is the number of selected background events expected in this sample. The number of selected signal events is connected to the selection efficiency of the signal, S, the branching ratio of the decay, B, and the number of $B\bar{B}$ decays in the dataset, $N_{B\bar{B}}$, by the following relation

$$S = \epsilon_S B N_{B\bar{B}}, \tag{4.7}$$

Optimization of the first equation, Eq. 4.5, requires prior knowledge of the branching ratio. This poses a problem when the branching ratio is not known and cannot be estimated. The second equation, Eq. 4.6 can be optimized without this knowledge. The branching ratio introduces an overall scaling factor that does not influence the optimization procedure. However, optimization based on this function becomes nonoptimal for a small number of selected background events as it will tend to push the signal efficiency down to small values, see the discussion in Punzi [63]. A definition for the significance level is proposed by Punzi that needs no prior knowledge of the branching ratio and still behaves properly for small numbers of background events. The definition of the significance level SL is given by

$$S_{LP} = \frac{S}{a/2 + \sqrt{B}} \tag{4.8}$$

where a is the desired significance of the measurement and B is the number of background events. By finding the maximum of this function the minimal detectable branching ratio is found that can still be measured, or excluded, with a significance of a. By including the desired significance, a, the formula becomes more robust for small numbers of B. We define a significance level that is used for our optimization process. It behaves exactly like Eq. 4.8 in the optimization procedure and is more practically used as $SL = \frac{N_{sig}}{2.5+\sqrt{B}}$, where N_{sig} is the number of selected signal events in the Monte Carlo sample. We have chosen to optimize for a 5σ discovery. We modeled the signal shape as a single Gaussian function with a floated mean of the B mass and a floated resolution on the official Monte Carlo sample. We define the signal region as $\pm 5\sigma$ of nominal B^+ mass, shown as the area between arrows in Figure 4.4, where σ is B mass resolution taken as 3 MeV, which is obtained from the Monte Carlo single Gaussian fit. The S is the number of B^+ candidates from the official signal MC, and B is the number of background candidates, which is the 1st order Chebyshev polynomial fit yield within the aforementioned signal region. To maximize CPU resources, we did not do a scan over all variable to find the maximum FOM. Instead, we optimize each variable individually. In this process, we find local maximum first and iterate the process until we find out the global maximum. The FOM has a stable maximum value for each optimized selection cut eventually. The important cuts we optimized are listed below:

Table 4.1: Optimized selection cut values.

Selection cut variable	Optimum cut value
Pointing Angle	> 0.99
Transverse Flight Length Significance $\frac{L_{xy}}{\sigma_{xy}}$ w.r.t. Beamspot	>4.0
B vertex probability	>0.1
Dimuon P_T	>7.0 GeV
ϕ mass window $\lvert m_{K^+K^-} - 1.019\rvert$	<8 MeV

- Pointing angle is defined as the cosine of the angle between the B meson 3D momentum direction and the direction obtained by the secondary and the primary vertices. The primary vertex is chosen to be the one that minimizes this angle for a given secondary vertex.
- Transverse flight length Significance $\frac{L_{xy}(B^+)}{\sigma_{xy}}$ w.r.t Beam Spot.
- B vertex Probability.
- Dimuon P_T.
- ϕ mass window.

Di-muon track pairs passing the $\psi(2S)$ candidate selection presented above are again fitted to a common vertex with an additional three(one) tracks having p_T greater than 1 GeV. The five(three)-track vertex fit is performed by constraining the muon tracks to the $\psi(2S)$ world average mass and assigning kaon mass hypothesis to the three(one) additional tracks. Fitted quintuplets(triplets) are considered to be loose $B^\pm \to \psi(2S)\phi K^\pm (B^\pm \to \psi(2S)K^\pm)$ decay candidates if the five(three)-track vertex fit is greater than 0.1. In case of multiple candidates, the one with highest B vertex Probability is retained. A total of 140(87259) candidates fulfilling the above criteria are found in a wide mass range 5220 - 5330 MeV (5150 - 5410 MeV).

The optimized selection cut values are shown in Table 4.1. The $B^+ \to \psi(2S)\phi K^+$ mass spectrum after applying the above optimized selection cuts is shown in Figure 4.4.

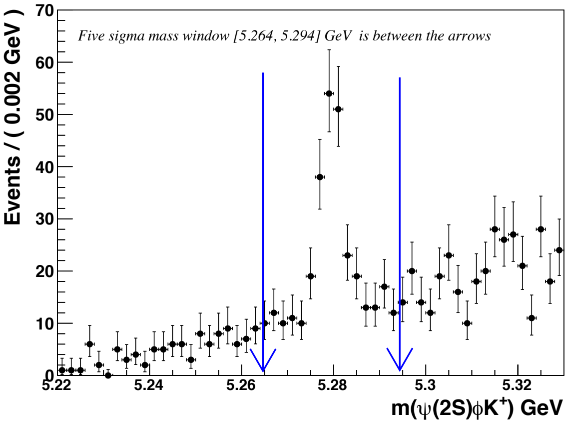

Figure 4.4: Invariant mass distributions of reconstructed $\psi(2S)\phi K^{\pm}$ candidates in mass range 5.22 - 5.33 GeV passing the selection criteria described in Section 4.9. Five sigma mass region to the nominal B^+ mass is the area between the arrows.

4.10 Fit to invariant B^+ mass distribution

An unbinned maximum-likelihood fit is used to extract the number of $B^{\pm}$ signal (Normalization) candidates from the data. The likelihood function is defined by:

$$L = \prod_{i=1}^{N} F_{signal}(m^i_{\psi(2S)\phi K^{\pm}}) + F_{bkg}(m^i_{\psi(2S)\phi K^{\pm}}) \tag{4.9}$$

where N is the total number of $\psi(2S)\phi K^{\pm}$ candidates in the invariant mass range $m_{min} < m_{\psi(2S)\phi K^{\pm}} < m_{max}$, with $m_{min} = 5220$ MeV and $m_{max} = 5330$ MeV. The F_{signal} and F_{bkg} are probability density functions that model the $B^{\pm}$ signal and background mass shapes in this range. For the signal, the mass is modeled with a sum of two Gaussian distributions $(wG_1(m_{\psi(2S)\phi K^{\pm}}) + (1-w)G_2(m_{\psi(2S)\phi K^{\pm}}))$ with a common mean for the signal but different width parameters (see Table 4.4) and a 1st order Chebyshev polynomial for the background. Where w is the double Gaussian convolution fraction, and

$$G_1(m_{\psi(2S)\phi K^{\pm}}) \equiv \frac{1}{\sqrt{2\pi}\delta m_{\psi(2S)\phi K^{\pm}}} e^{\frac{-(m_{\psi(2S)\phi K^{\pm}} - m_{B^{\pm}})^2}{2(\delta m_{\psi(2S)\phi K^{\pm}})^2}} \tag{4.10}$$

whose mean value $m_{B^{\pm}}$ is taken from PDG and its width $\delta m_{\psi(2S)\phi K^{\pm}}$ is hypothesized. Similarly G_2 can be expressed as a Gaussian. The mass resolution $\sigma_{m_{\psi(2S)\phi K^{\pm}}}$ is defined as the half of width of the $B^{\pm}$ mass distribution for which the integral of F_{signal} retains 68.3% of N_{sig} symmetrically around the fitted mass $m_{B^{\pm}}$.

For the background, the mass distribution is modelled with a first order Chebychev polynomial.

$$F_{bkg}(m_{\psi(2S)\phi K^{\pm}}) \equiv Ch(m_{\psi(2S)\phi K^{\pm}}; c_0) \equiv 1 + c_0 . m_{\psi(2S)\phi K^{\pm}} \tag{4.11}$$

On account of partially reconstructed $B^{\pm}$ mesons and kinematic reflections, no attempt is made to model the background far from the $B^{\pm}$ mass region. In the mass region 5220 - 5330 MeV a 1st order Chebyshev polynomial model to the background is adequate within available statistics.

The fit has five free parameters: common Gaussian mean, w, width 1, width

2, N_{sig} in case of MC events assuming $F_{bkg} \equiv 0$ and three free parameters in data: N_{sig}, N_{bkg}, and C_1.

4.11 Results

4.11.1 The B sideband subtracted ϕ

The raw K^+K^- mass within $\pm 5\sigma, (\sigma = 3MeV)$ of B^+ mass window is shown in Fig. 4.5(a). To subtract non-B background, we divide the K^+K^- mass into 18 bins in the range of [0.986,1.058] GeV with a bin width of 4 MeV. In each bin, we extracted B^+ candidates yield after fitting signal to a double Gaussian function and background to a 1st order Chebyshev polynomial. For each fit, we fix the B^+ mass shape (double Gaussian signal with common mean, shape fixed by signal official Monte Carlo fit parameters listed in Table 4.4). The B sideband subtracted K^+K^- mass distribution is shown in Figure 4.5(b).

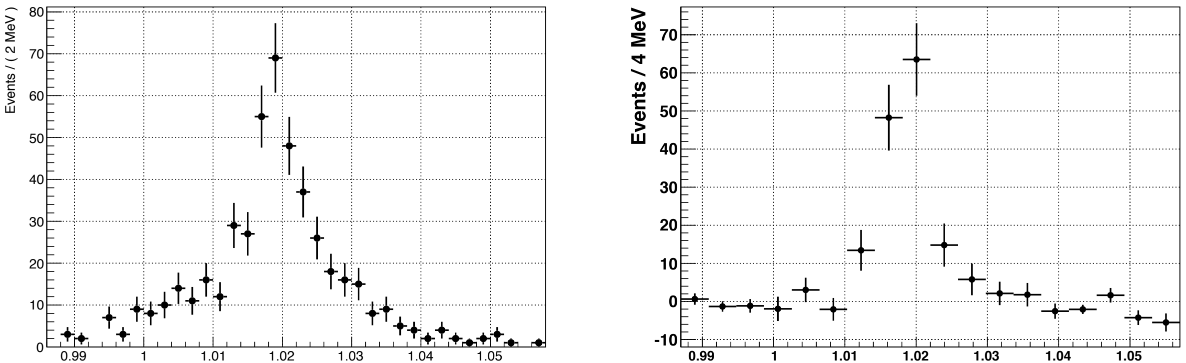

(a) ϕ mass distribution inside 5σ B mass window. (b) B sideband subtracted ϕ mass distribution.

Figure 4.5: ϕ mass distribution inside 5σ B mass window $[5.264, 5.294]$ on the Left and after B^+ sideband subtraction on the Right.

4.11.2 The ϕ signal

Among the three kaon tracks in the B candidate event, there are two K^+K^- pairs. Because of limited available phase space (80 MeV), the ϕ candidates are from both K^+K^- pair with high mass as well as K^+K^- pair with low mass, as shown in Figure 4.6 from Monte Carlo signal sample.

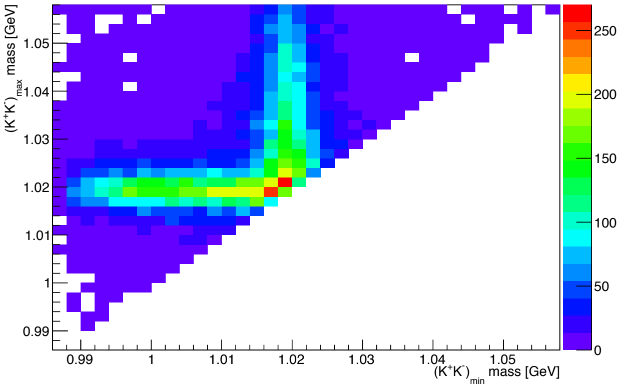

Figure 4.6: K^+K^- pairs mass distribution from Monte Carlo signal showing both pairs are possible candidates for ϕ, we choose the pair which is closest to ϕ PDG mass as our ϕ candidate.

We keep the K^+K^- pair which has the mass closest to the ϕ PDG mass (1.01946) GeV as our ϕ candidate. We fit the K^+K^- mass with two PDFs: one with a P-wave relativistic Breit-Wigner convoluted with Gaussian resolution function with width fixed to 1.3 MeV obtained from MC simulation and the other is with a Gaussian shape coming from f_0 contamination described here. We tried to calculate the f_0 contribution and the K^+K^- non-resonance contribution in the ϕ mass fit. We generated 479K dedicated MC $B^+ \to \psi(2S) f0 K^+$ events and applied the same selection ($B^+ \to \psi(2S)\phi K^+$) cuts to see if there is any f0 contribution. We collected the (K^+K^-) pair closest to the ϕ nominal mass and the distribution is modelled by a Gaussian shape shown in Figure 4.7 (a).

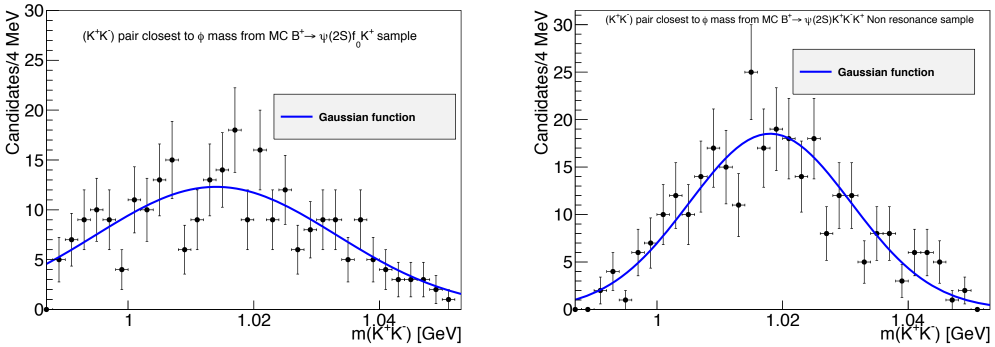

(a) K^+K^- closest to ϕ nominal mass from $B^+ \to \psi(2S)f_0K^+$ dedicated MC sample is modelled by a Gaussian

(b) K^+K^- closest to ϕ nominal mass from $B^+ \to \psi(2S)K^+K^-K^+$ private MC sample is modelled by a Gaussian

Figure 4.7: ϕ contamination study.

We also generated 497K private MC $B^+ \to \psi(2S)K^+K^-K^+$ Non-resonant events and applied the same selection ($B^+ \to \psi(2S)\phi K^+$) cuts to see if there is any non-resonant K^+K^- contribution. The (K^+K^-) pair closest to the ϕ nominal mass is modelled by a Gaussian shown in Fig. 4.7 (b).

We carried out the ϕ mass fit with an integration of the function in each bin. The fitted K^+K^- mass is shown in Fig. 4.8. The fit parameters are listed in Table 4.2. We use $\frac{\chi^2}{d.o.f}$ as a test of goodness-of-fit: $\frac{\chi^2}{d.o.f} = \frac{35.79}{12} = 2.98$.

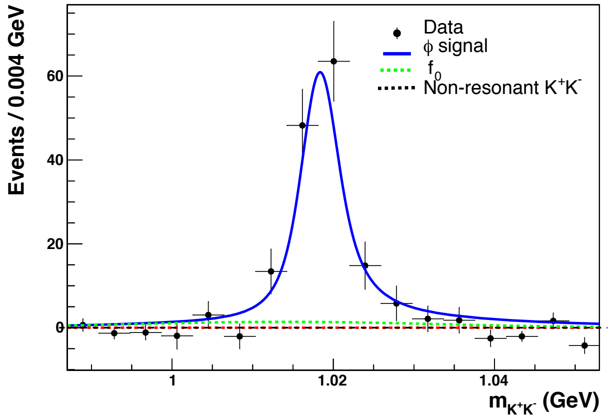

Figure 4.8: The K^+K^- mass distribution with signal modelled by a P-wave relativistic Breit-Wigner convoluted with Gaussian resolution function and f_0 contamination, Non-resonant K^+K^- contaminations are modelled by a Gaussian distributions.

Table 4.2: ϕ mass P-wave relativistic Breit-Wigner fit parameters.

Signal Fit parameters	Fit value
Mean	1.0184±0.0003 GeV
width	4.36± 0.82 MeV
ϕ Yield	158±15
f_0 Background fit parameters Single Gaussian	Fit value
Fixed Mean from MC	1.014 GeV
Fixed sigmafrom MC	19.18 MeV
nf0	20±9
Non-resonant K^+K^- Background fit parameters Single Gaussian	Fit value
Fixed Mean from MC	1.01803 GeV
Fixed sigmafrom MC	12.903 MeV
nNonresonantKK	0.00±16

4.11.2.1 Fit bias validation studies using Toy Monte Carlo

Various validation tests have been performed to verify the quality of the fit procedure (closure test). To validate the fit procedure and determine possible biases introduced by the algorithms, a study has been performed on fast parametrized simulated data also called 'toy Monte Carlo' events.

In total 3000 toy Monte Carlo sample sets have been produced, each sample

Table 4.3: The mean and width of a Gaussian fitted to the pull distributions of the fitted number of ϕ (N_{ϕ}), f_0 (N_{f_0}), and non-resonant K^+K^- ($N_{NonResKK}$) events of 3000 fits on a toy Monte Carlo sample. Three types of samples are fitted, the left (middle, right) two rows present the results with 100 signal events added(with 150 ϕ events added, with 200 ϕ events added) samples.

pull	+100 ϕ events		+150 ϕ events		+200 ϕ events	
	mean	width	mean	width	mean	width
N_{ϕ}	-0.0332±0.0253	0.7669±0.0195	0.0368±0.0159	0.8595±0.01323	-0.1049±0.0212	0.6585±0.0168
N_{f_0}	0.4730±0.0317	0.9053±0.0240	0.2637±0.0165	0.8393±0.01379	0.4125±0.0324	0.8561±0.0232
$N_{NonResKK}$	-0.0611±0.0239	0.5910±0.0215	0.007076±0.01746	0.7949±0.0126	0.0704±0.0268	0.5747±0.0223

set consists of 150 ϕ, 20 f_0 and 10 nonresonant K^+K^- candidates. The samples are generated using the p.d.f. shapes that are also used to fit the data. Approximately the same constitution and number of background events are produced as found in the fit to the data, as summarized in Table 4.2. The parameters determined by the likelihood fits are compared with the input values, so-called 'true' values, by calculating the pull. The pull on a parameter x is defined by

$$pull_x = \frac{x_{fit} - x_{true}}{\sigma_x}, \tag{4.12}$$

where x_{fit} is the fitted parameter, σ_x the associated fit error and x_{true} is the true value of the parameter. The pull distributions are fitted with a Gaussian function. The mean and widths of the fitted Gaussians are presented in Table 4.3. Figure 4.9 shows the pull distribution plots for the ϕ yield in three Toy MC samples.

The fit algorithm gives consistent and unambiguous results. No artificial biases are introduced in the fitted parameters by the algorithm. The errors are neither over nor underestimated. In conclusion, the fit model and its implementation performs as

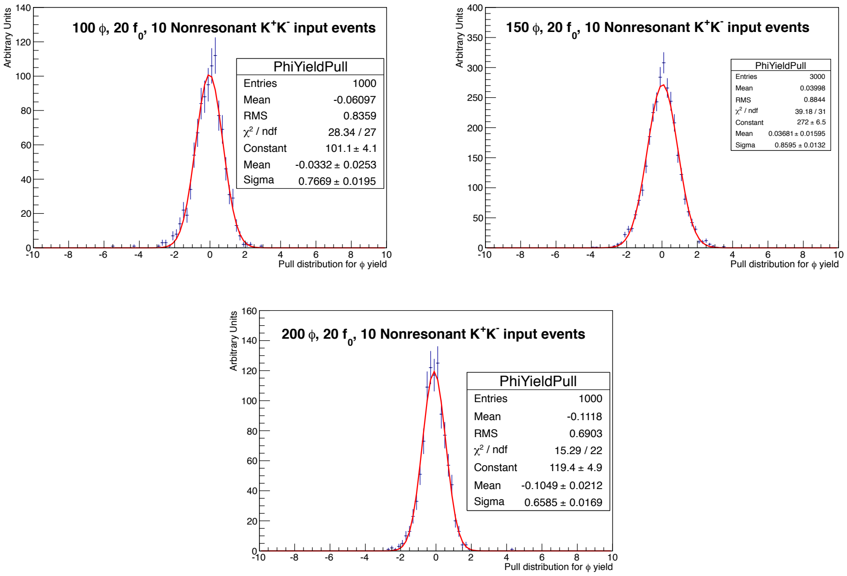

Figure 4.9: The mean and width of a Gaussian fitted to the pull distributions of the fitted number of ϕ events of 3000 fits on a toy Monte Carlo sample. Three types of samples are fitted, the left (middle, right) column presents the results with 100 signal events added(with 150 ϕ events added, with 200 ϕ events added) samples.

desired.

We also plotted the difference of the input ϕ yield with the fitted ϕ yield for the above three samples. As an example one of the distributions of this difference is shown in Figure 4.10. The bias in ϕ yield is very small ($\sim 0.5/150 = 0.3\%$). This demonstrates the fitter is extracting each component properly, thus the closure test is verified.

The ϕ fraction $\frac{N_\phi}{N_\phi+N_{f0}+N_{NonResKK}}$ is not very sensitive to the change in non-ϕ component yield. As an example one of the distributions of this parameter is shown in Figure 4.11. The distribution is representative for all the decay mode fits and is very broad. The two background p.d.f.'s are very similar and do not hold much dis-

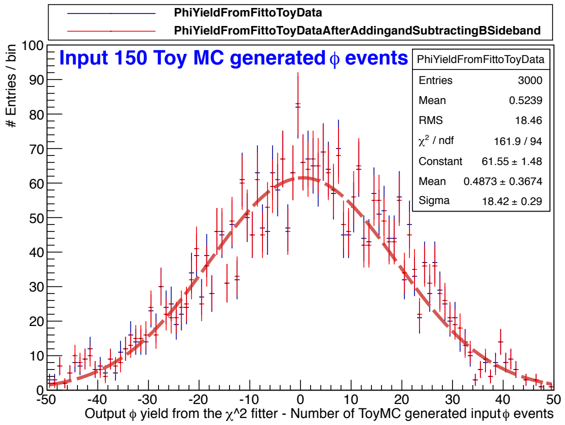

Figure 4.10: Distribution of the difference between the fitted ϕ yield and the input ϕ yield from 3000 Toy MC fits. The difference is produced around ~ 0. A Gaussian function is fitted to the distribution and imposed on the plot in a grey dashed line.

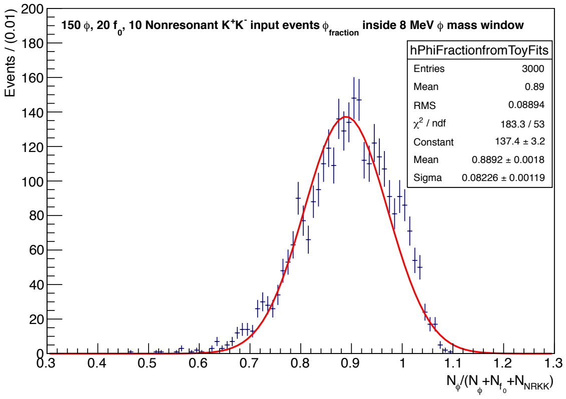

Figure 4.11: Distribution of the fitted ϕ fraction $\frac{N_\phi}{(N_\phi+N_{f_0}+)}$ in the 8 MeV *phi* mass window from 3000 Toy MC fits. The fraction is produced around ~ 0.89. A Gaussian function is fitted to the distribution and imposed on the plot in a red solid line. 150 ϕ, 20 f_0, and 10 Non resonant K^+K^- are the input to the fitter.

criminative power against each others shape. We do not expect any errors introduced from this insensitivity to affect the other fitted parameters. The correlations between the other parameters and the ϕ fraction parameter are not significant.

4.11.2.2 Simultaneous fitting of K^+K^- mass

We tried a simultaneous fit to extract the ϕ fraction from the $m(K^+K^-)$ mass distributions. Without applying the 8 MeV ϕ mass window cut on $m(K^+K^-)$, we have two $m(K^+K^-)$ histograms; one is for the events within $\pm 3\sigma$ of the B^+ mass (h1) and the other is from the B^+ lower sideband [5.22, 5.27925-3×0.003]GeV and upper sideband [5.27925+3×0.003, 5.33]GeV (h2).

We fit two histograms simultaneously. We first parameterized h2 using a double Gaussian function (non B^+) and it is fixed in the simultaneous fit. The other pdfs we used for h1 are: ϕ, f_0, nonresonant K^+K^-. Both h1 and h2 share the same non B^+. We also tried fitting the above two histograms simultaneously with different pdf shapes, we first parameterized the $m(K^+K^-)$ shape from B^+ sidebands with a Breit-Wigner convoluted with a Crystal-Ball function, also we include a Relativistic Breit-Wigner shape for a small excess around $m(\phi)$ as shown in right plot in Figure 4.12 and it is fixed in the simultaneous fit as shown in left plot in Figure 4.12. The other pdfs we used for $m(K^+K^-)$ inside 3σ B^+ mass window are: ϕ, f_0, Nonresonant K^+K^-. The number of non B^+ in $m(K^+K^-)$ inside 3σ B^+ is restricted to be 194, while the number of non B^+ in B^+ sideband is floating or fixed to 913. We used the same parameterization for f_0 and nonresonant K^+K^- as shown in Figure 4.7. The ϕ is a relativistic Breit-Wigner convoluted with Gaussian resolution function (1.3 MeV). The mass and the width of ϕ are fixed to their nominal values taken from Particle Data Group (PDG). The fit returns a non ϕ yield of 2 ± 2 events, and the conclusion from the simultaneous fit is $(99\pm12)\%$ of K^+K^- are from real ϕ signal.

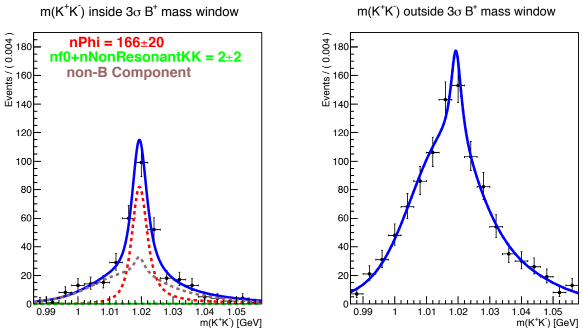

Figure 4.12: Simultaneous fitting of K^+K^- mass.

Table 4.4: Monte Carlo double Gaussian fixed parameters.

Parameter	Signal	Normalization Channel
Width 1	6.68±0.16 MeV	31.9±3.2 MeV
Width 2	2.30±0.03 MeV	12.05±0.57 MeV
Gaussian Mean 1	5279.20± 0.02 MeV	5279.76± 0.35 MeV
Fraction	0.190±0.011	0.209±0.046

4.11.3 Signal and Normalization channel shapes from MC

Currently we use one million officially generated MC signal events and a half million MC normalization channel events for our study. The reconstructed $\psi(2S)\phi K^+$ and $\psi(2S)K^+$ invariant mass distributions in a restricted mass range from 5.26 to 5.3 GeV for signal and for normalization channel from 5.2 to 5.36 GeV after all selection cuts are shown in Fig. 4.13(a) and Fig. 4.13(b) respectively. We use a double Gaussian function with a common mean to model their shapes. The shape parameters returned from the fit are listed in Table 4.4.

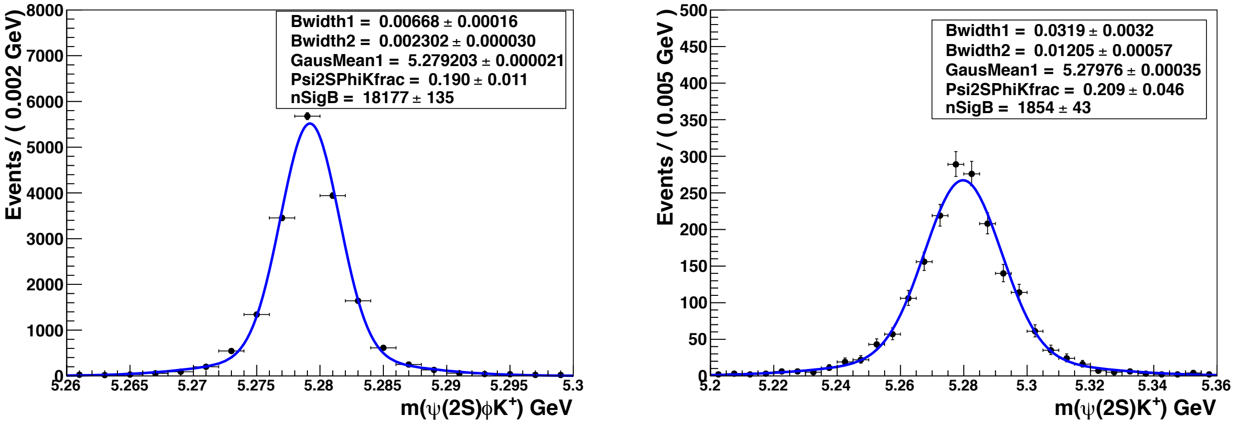

(a) MC signal yield

(b) MC normalization channel yield

Figure 4.13: MC fit results.

4.11.4 Signal and Normalization channel yields from Data

In order to cancel out some of the systematic uncertainties, we apply exactly the same requirements for $B^+ \to \psi(2S)K^+$ as in the $B^+ \to \psi(2S)\phi K^+$ channel except the requirement of ϕ. The reconstructed signal and $B^+ \to \psi(2S)K^+$ from data after all selection cuts are shown in Fig. 4.14. We use a double Gaussian with a common mean to model the B^+ peak, and modeled the background by a 1st order Chebyshev polynomial. The fitted shape parameters are listed in Table 4.4. Since we have high statistics in the normalization channel and to save the CPU time, we perform a binned log-likelihood fit and let the double Gaussian common mean, widths and fraction to float. Then we use $\frac{\chi^2}{d.o.f}$ as a test of goodness-of-fit:$\frac{\chi^2}{d.o.f} = \frac{642.68}{519} = 1.24$ for the normalization channel. The normalization channel fit parameters from data are listed in Table 4.5.

The $B^{\pm}$ signal extracted from the fit is 140 ± 15 and the background is 624 ± 27.

Table 4.5: $\psi(2S)K$ fit parameters.

$\psi(2S)K$ parameters	Value
Double Gaussian common mean	5.2787±0.0001 GeV
Width1	22.3 ±0.4 MeV
Width2	10.0 ±0.2 MeV
fraction	0.482±0.018
c1	-0.15±0.01

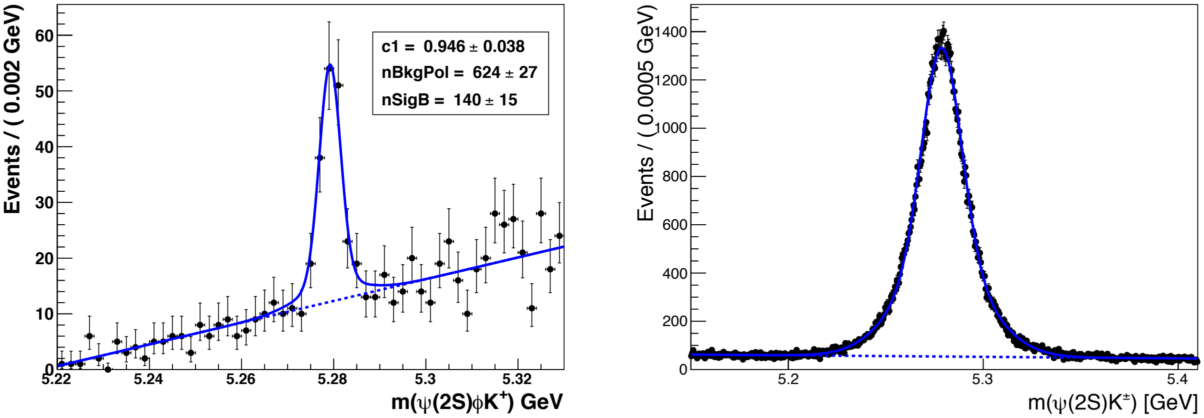

(a) Signal from 2012 Dataset

(b) Normalization yield from 2012 Dataset

Figure 4.14: $(2S)\phi K^{\pm}$ candidates on the left and $(2S)K^{\pm}$ candidates on the right in a narrow mass window (no distinction made between charges of the combinations). The solid line is the projection of the results of the unbinned maximum likelihood fit to all $(2S)\phi K^{\pm}$ candidates in the mass range 5.22 5.33 GeV and the binned maximum likelihood fit to all $(2S)K^{\pm}$ candidates in the mass range 5.15 - 5.41 GeV respectively. The dashed lines are the projections for the background components of the same fit.

The signal mass resolution σ_m from Monte Carlo is the weighted quadrature sum of the two Gaussians sigmas: $\sigma_m = \sqrt{w\sigma_1^2 + (1-w)\sigma_2^2} = \sqrt{0.19 \times (0.00668)^2 + 0.81 \times (0.002302)^2} =$ 3.6 MeV.

For the normalization channel the number of $B^{\pm}$ extracted from the fit is 87259±355 and the background is 28042±258. The $B^{\pm}$ mass resolution σ_m from data is the weighted quadrature sum of the two Gaussians sigmas: $\sigma_m = \sqrt{w\sigma_1^2 + (1-w)\sigma_2^2} = \sqrt{0.48 \times (0.0223)^2 + 0.52 \times (0.010)^2} = 17$ MeV; the equivalent for Monte Carlo is 18 MeV.

4.11.5 Signal significance

We see a clear B^+ signal in Fig. 4.15(a) from data after applying all selection cuts. We model the B^+ signal by a double Gaussian function with the RMS, common mean of both Gaussians and the core Gaussian's fractional ratio fixed to the expected values obtained from $B^+ \to \psi(2S)\phi K^+$ signal MC shown in Table 4.4. We model the background by a 1st order Chebyshev polynomial. Fig. 4.15(a) shows a fit with the signal and background together, where the only B^+ yield and background yield are floating. We observe 140 ± 15 signal B^+ events. We perform a goodness-of-fit using $\frac{\chi^2}{d.o.f}$ value. To avoid empty bins we rebinned the histogram and calculated $\frac{\chi^2}{d.o.f}$ for the $[5.22, 5.33]$ GeV range, and the returned value for this fit is 0.96. To evaluate the significance of the B^+ signal for completeness, we perform two hypothesis tests to the data in observation of $B^+ \to \psi(2S)\phi K^+$ signal: (1) A null hypothesis is tested by fitting the data using a background-only model, and (2) a signal hypothesis is tested by fitting the data to a background model and a signal model together while floating the signal amplitude but fix the B^+ signal mass and B^+ signal shape. The likelihood returned from the null- or signal-hypothesis fit is denoted by L_0 or L_S , respectively.

The local significance is defined as $\sqrt{-2\ln(L_S/L_0)}$. We find the B^+ signal has a local significance of 12.7σ with $-\ln(L_S) = 6197.47$ and $-\ln(L_0) = 6116.37$. Since we fixed B^+ mass and B^+ width in our case, we do not take Look-Elsewhere-Effect into account.

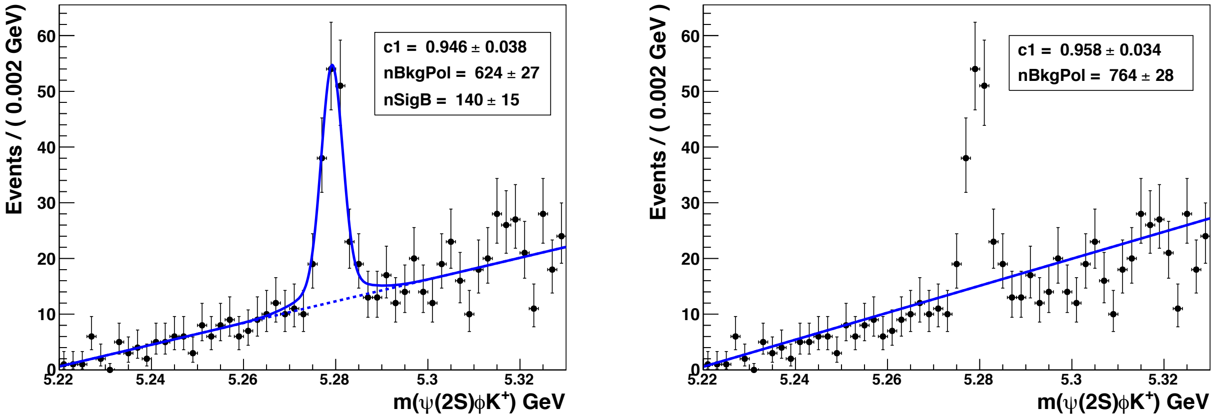

(a) Signal and Background hypothesis

(b) Background hypothesis only

Figure 4.15: Significance studies. Invariant mass distribution of reconstructed $B^\pm \rightarrow \psi(2S)\phi K^\pm$ candidates. The points with error bars are data. The solid line is the projection of the result of the unbinned maximum likelihood fit to all $\psi(2S)\phi K^\pm$ candidates in the mass range 5.22 5.33 GeV. The dashed line is the projection for the background component of the same fit.

4.11.6 Relative reconstruction efficiency with $B^\pm \rightarrow \psi(2S)K^\pm$ channel

The reconstruction efficiencies and relative reconstruction efficiencies are given below:

- The overall analysis efficiency for the $B^+ \rightarrow \psi(2S)\phi K^+$ detection:

$$\varepsilon_{RecoSignal} = \frac{N_{signalreco}}{N_{signalgenerated}} = \frac{18177}{9538259} = (1.91 \pm 0.01) \times 10^{-3}$$

- The overall analysis efficiency for the $B^+ \to \psi(2S)K^+$ detection:

  $$\varepsilon_{RecoNormalizationchannel} = \frac{N_{B^+ \to \psi(2S)K^+ Reco}}{N_{B^+ \to \psi(2S)K^+ generated}} = \frac{1854}{504823} = (3.67 \pm 0.08) \times 10^{-3}$$

- $\varepsilon_{relative} = \frac{\varepsilon_{RecoSignal}}{\varepsilon_{RecoNormalizationchannel}} = 0.520 \pm 0.012$

  Many systematics cancel out in the ratio $\frac{\varepsilon_{\psi(2S)\phi K^+}}{\varepsilon_{\psi(2S)K^+}}$ which enters in the BF calculation.

- $B^+ \to \psi(2S)\phi K^+$ yield in data: 140±15

- $B^+ \to \psi(2S)K^+$ yield in data: 87259±355

4.11.7 B^+ p_T comparison between Monte Carlo and Data

We investigated the B^+ candidates p_T distributions after subtracting background for both data and Monte Carlo and compared to each other. We divide the signal B^+ p_T range into 10 bin intervals with 5 GeV bin width, except the last bin, where we do not have enough statistics, { 10-15, 15-20, 20-25, 25-30, 30-35, 35-40, 40-45, 45-50, 50-55, 55-100 } GeV. In each bin, the number of B^+ candidates are extracted by fitting the B^+ mass distribution with a double Gaussian shape fixed used the signal fit parameters shown in Table 4.6. The background for $\psi(2S)\phi K^+$ is modelled by a 1st order Chebyshev polynomial on data. Figure 4.16(a) shows the p_T distributions comparison for signal. Similarly, we divide the normalization channel B^+ p_T into 12 bin intervals with 5 GeV binwitdth(except the last bin), { 5-10, 10-15, 15-20, 20-25, 25-30, 30-35, 35-40, 40-45, 45-50, 50-55, 55-60, 60-100 }. In each bin, the number of B^+ candidates are extracted by fitting the B^+ mass distribution with a double Gaussian shape fixed, the $\psi(2S)K^+$ fit parameters used are shown in Table 4.6.

Table 4.6: Fit parameters used for B^+ p_T comparison between Monte Carlo and Data.

fit parameters	$\psi(2S)\phi K^+$ fit Values	$\psi(2S)K^+$ fit Values
Double Gaussian common Mean	fixed to 5.279 GeV	floating value in [5.275,5.285] GeV
Width1	0.002386 GeV	0.0319 GeV
Width2	0.00895 GeV	0.01203 GeV
fraction	0.8389	0.213

The background for $\psi(2S)K^+$ is modelled by a 1st order Chebyshev polynomial on data. Figure 4.16(b) shows the p_T distributions comparison for $\psi(2S)K^+$.

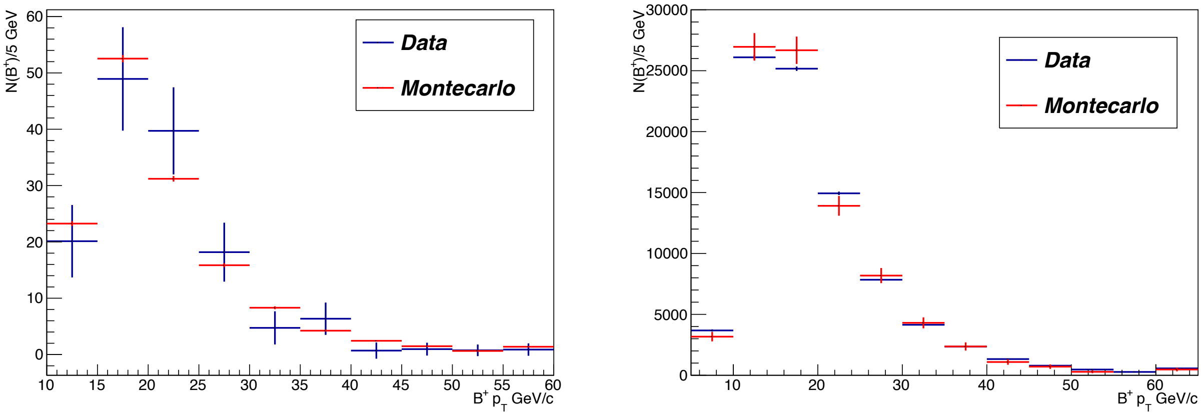

(a) $B(\psi(2S)\phi K)$ Candidates p_T distribution comparison between MC and Data

(b) $B(\psi(2S)K)$ Candidates p_T distribution comparison between MC and Data

Figure 4.16: B^+ Candidates p_T distribution comparison between MC and Data.

Table 4.7: Fixed and floating parameters.

Parameter	$\psi(2S)\phi K^+$	fixed/floated	$\psi(2S)K^+$	fixed/floated
Double Gaussian common Mean	5.2792 GeV	fixed	5.2787$\pm$ 0.0001 GeV	floated
Width 1	6.68 MeV	fixed	22.3 $\pm$ 0.4 MeV	floated
Width 2	2.302 MeV	fixed	10.0 $\pm$ 0.2 MeV	floated
Fraction of 1 st Gaussian	0.190	fixed	0.48 $\pm$ 0.02	floated
Signal Fit Yield	140$\pm$15	floated	87259$\pm$355	floated
Background Fit Yield	764$\pm$28	floated	28042$\pm$258	floated
1st order Chebyshev polynomial Fit coefficients:				
c1	0.958$\pm$0.034	floated	-0.152$\pm$ 0.011	floated

4.11.8 Measured Branching fraction

The fit parameters for signal and normalization channel are listed in Table 4.7. When no B^+ p_T efficiency reweighting correction is applied on B^+ mass, taking the BF of $\phi \to K^+K^-$ as 0.489$\pm$0.005 and the BF of $B^+ \to \psi(2S)K^+$ as $(6.27 \pm 0.24) \times 10^{-4}$ from PDG; the default result of measured BF for $B^+ \to \psi(2S)\phi K^+$ can be obtained from the relation

$BF\left(B^+ \to \psi(2S)\phi K^+\right) = \frac{\left(B^+ \to \psi(2S)\phi K^+\right)_{datayield} \times BF\left(B^+ \to \psi(2S)K^+\right)_{PDG}}{\left(B^+ \to \psi(2S)K^+\right)_{datayield} \times (\varepsilon_{relative}) \times BF(\phi \to K^+K^-)_{PDG}}$ so the measured BF of $B^+ \to \psi(2S)\phi K^+$ is determined as: $(4.0 \pm 0.4(stat.)) \times 10^{-6}$.

4.11.9 Statistical and systematic uncertainties

Estimates of the contributions to the systematic uncertainty in $\mathcal{B}(B^+ \to \psi(2S)\phi K^+)$ are summarized in Table 4.12, and described below.

We estimated the systematic uncertainty coming from data/MC difference in the signal mass shape by allowing the widths of the two Gaussian functions to vary in the fit, with the background function fixed to a first order polynomial. Figure 4.17 shows the signal fit with floated double Gaussian widths. We got signal yield with floated widths:128±15 and the estimated systematic is 8.6%.

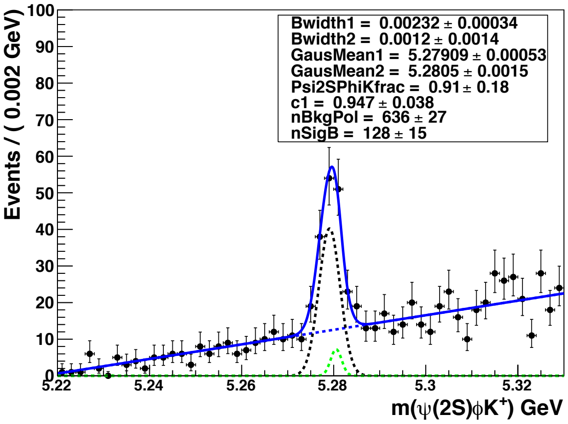

Figure 4.17: Signal yield with floated double Gaussian widths.

Sources of systematic uncertainty such as muon ID, trigger efficiency and efficiency for the three common tracks (two muons and one kaon) cancel each other in our case. In order to verify that systematic uncertainties cancel for the two muons and one kaon in signal and normalization channel, we compared the muon p_T and η between the signal channel and the normalization channel as shown in Figure 4.18, the distributions between these two samples are very similar. For kaons, we have chosen high purity kaon tracks with $p_T > 1$ GeV, and in the reference [64], the track efficiency as a function of p_T/η is almost constant for tracks with $1 < p_T < 80$ GeV. The uncertainty in the charged particle track reconstruction efficiency, obtained in an independent study by comparing two-body and four-body D^0 decays in data and simulated events [65], gives an uncertainty of 3.9% per track, and we take a total uncertainty of 7.8% for the three kaon tracks(both channels have at least one kaon tracks). Assigning 12% seems too conservative, so we keep 7.8% as track systematic.

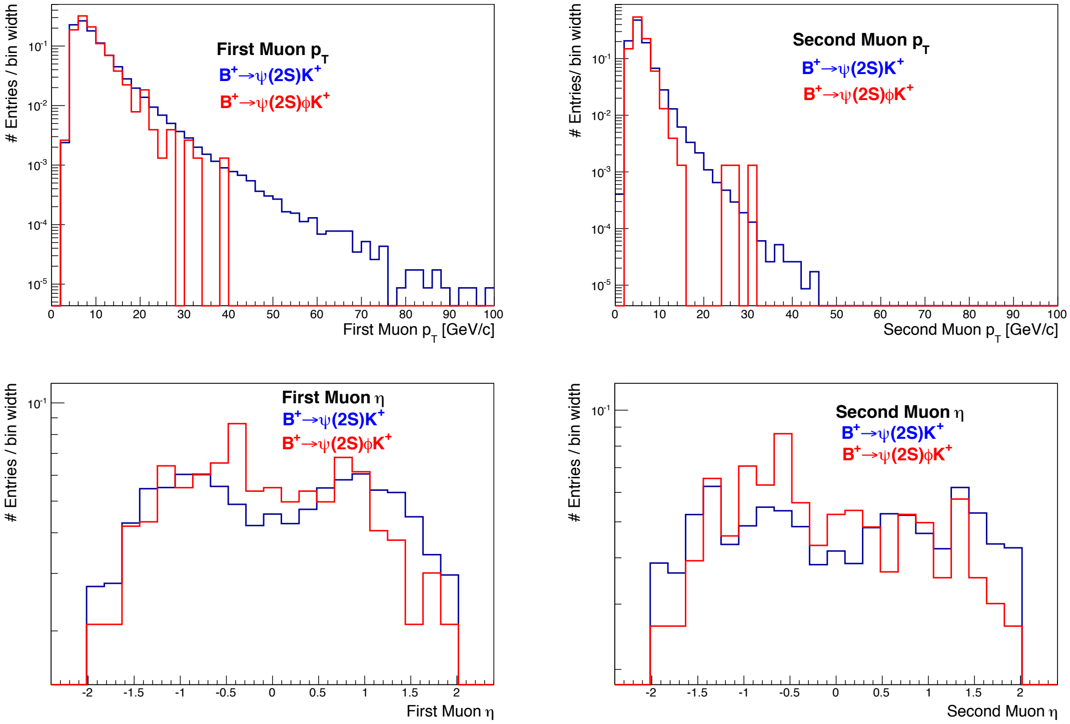

Figure 4.18: Kinematic distributions comparison for signal and normalization channel Muons.

We estimated the systematic uncertainty associated with B^+ p_T distributions for both signal and normalization channel; however the signal channel has low statistics. A mismatch in the p_T distribution between B^+ mesons in MC simulations and in data can lead to an incorrect efficiency. We therefore reweight the signal and normalization events using a weighting function derived from the normalization channel.

Table 4.8: Signal B^+ sideband subtracted B^+ p_T 4th order polynomial fit parameters.

Fourth order polynomial fit parameters	on signal from data	on reconstructed signal from MC
Chi2	0.302404	199.829
NDf	3	3
p0	-412.577± 191.454	-557.071 ± 13.4279
p1	73.1946 ± 33.3643	97.8279 ± 2.37003
p2	-4.09385 ± 2.02497	-5.59765 ± 0.145213
p3	0.0935357 ± 0.0516664	0.132778 ± 0.00373212
p4	-0.000760277 ± 0.000473051	-0.0011308 ± 3.43626e-05

We fitted the signal B^+ side band subtracted B^+ p_T distributions to a 4th order polynomial in the p_T window [10,42] GeV/c on data and reconstructed MC events. Figure 4.19 shows the 4th order polynomial fit plots for signal channel both from data and reconstructed MC and the corresponding fit parameters are listed in Table 4.8. We define the signal B^+ p_T reweighting factor $= \frac{f_{signaldata}}{f_{signalMCReco}}$ at MC generator level using the 4th order polynomial fit parameters from the Table 4.8.

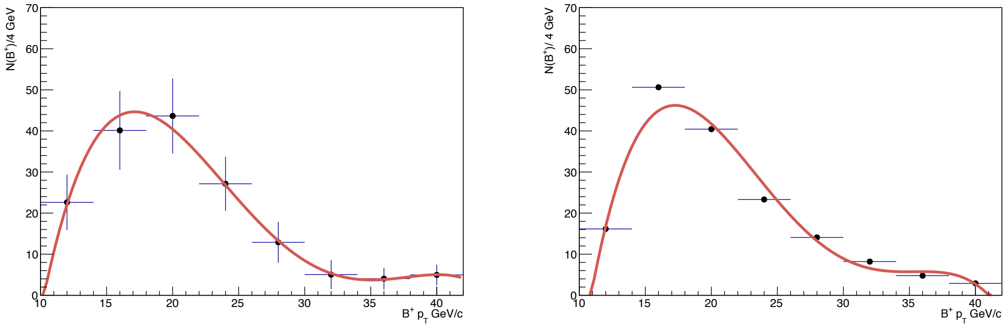

Figure 4.19: Signal B^+ sideband subtracted B^+ p_T fit to a 4th order polynomial for data on the left and for reconstructed MC on the right in the p_T window $[10, 42]$ GeV/c.

The default reconstruction efficiency is: 0.02014 and reconstruction efficiency after reweighting: 0.02223. The % change in the efficiency is: 10.4. Figure 4.20 shows the signal B^+ p_T comparison between unweighted and reweighted at the reconstruction level.

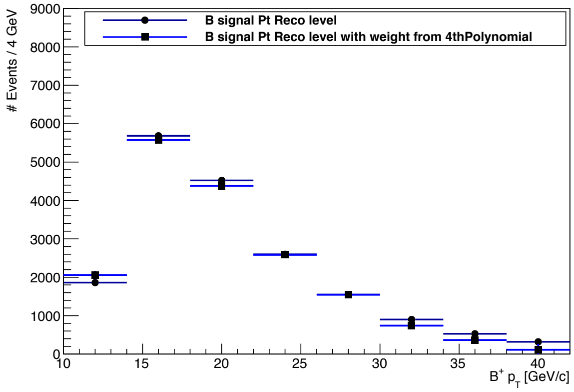

Figure 4.20: B^+ p_T comparison between unweighted and reweighted at the reconstruction level.

For the normalization channel, we fitted the B^+ side band subtracted normalization channel B^+ p_T distributions to a 6th order polynomial in the p_T window [10,40] GeV/c on data and reconstructed MC events. Figure 4.21 shows the 6th order polynomial fit plots for both data and reconstructed MC and the corresponding fit parameters are listed in Table 4.9. We define the normalization channel B^+ p_T reweighting factor $= \frac{f_{normchandata}}{f_{normchanMCReco}}$ at MC generator level using the 6th order polynomial fit parameters from the Table 4.9. The default reconstruction efficiency is: 0.03741 and the reconstruction efficiency after reweighting is: 0.03678. The % change

Table 4.9: Normalization B^+ sideband subtracted B^+ p_T 6th order polynomial fit parameters.

Sixth order polynomial fit parameters	on normalization channel from data	on reconstructed normalization channel from MC
Chi2	31.6148	20.5966
NDf	23	23
p0	-94177.7±7813.74	-60731.9±44534.2
p1	23549.9±2155.5	13477.3±12350.3
p2	-2177.19±237.083	-975.376±1364.77
p3	102.394±13.3678	29.8114±77.2373
p4	-2.6451±0.409265	-0.300248±2.37092
p5	0.0359143±0.0064756	-0.00267621±0.037575
p6	-0.00020102±4.15102e-05	5.30302e-05±0.000241043

in the efficiency is 1.7. The ratio of efficiencies from the reweighted MC events is compared to the nominal value to extract a systematic uncertainty of 5.3%. Figure 4.22 shows the B^+ p_T comparion between unweighted and reweighted at the reconstruction level.

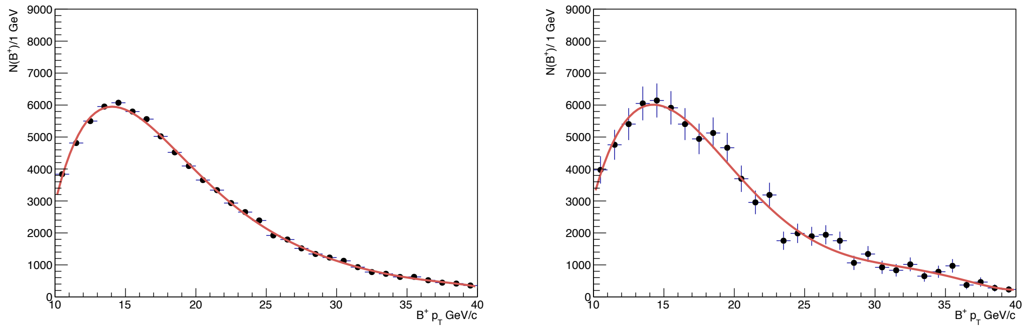

Figure 4.21: Normalization B^+ sideband subtracted B^+ p_T fit to a 6th order polynomial for data on the left and for reconstructed MC on the right in the p_T window $[10, 40]$ GeV/c.

The choice of the K^+K^- candidate closest to the nominal ϕ mass causes a bias,

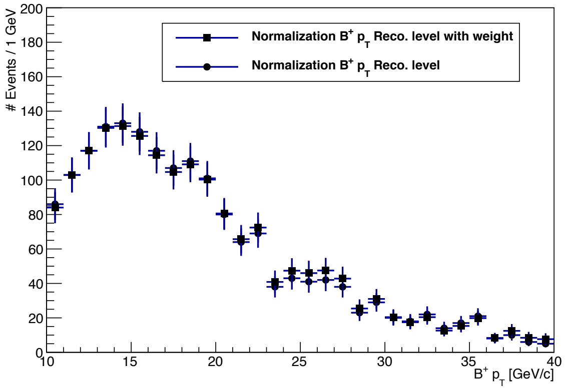

Figure 4.22: B^+ p_T comparison between unweighted and reweighted at the reconstruction level.

and, to estimate any systematic contamination of the K^+K^- mass peak from non-ϕ backgrounds, the analysis is repeated after removing the selection on the K^+K^- mass being closest to the mass of the ϕ. This makes the choice of the K^+K^- pair independent of the closest value to the nominal ϕ mass, and the branching fraction is remeasured by keeping both K^+K^- pair candidate events. The subsequent $B^+ \to \psi(2S)K^+K^-K^+$ invariant mass distribution is shown in Fig. 4.23. The signal in Fig. 4.23 is clear, but there is more background relative to the signal mass distribution shown in Fig. 4.15. There are 165 ± 18 B^+ signal events with two K^+K^- combinations for each event. The efficiency for the $B^+ \to \psi(2S)\phi K^+$ signal after removing the choice of ϕ candidate is $(2.14 \pm 0.02) \times 10^{-3}$, and the redetermined $\mathcal{B}(B^+ \to \psi(2S)\phi K^+)$ is $(4.2 \pm 0.4(stat)) \times 10^{-6}$. The 5.0% difference between this and the nominal branching fraction is used as the systematic uncertainty from possible non-ϕ backgrounds.

The uncertainties in modeling the $B^+ \to \psi(2S)\phi K^+$ and the normalization

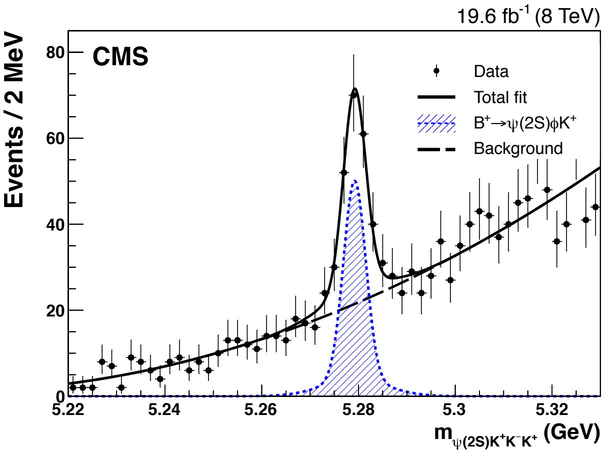

Figure 4.23: The $\psi(2S)K^+K^-K^+$ invariant mass distribution with no ϕ mass selection. The solid curve shows the result of fitting this distribution to a signal represented by two Gaussian functions and a second-order polynomial for the background. The shaded area represents the signal component, while the black dashed line shows the fitted background contribution.

channel backgrounds are estimated to be 2.9% and 2.2%, respectively, by adding polynomials of higher order in the fit to describe the background. The uncertainty from the angular distribution of the K^+K^- system is estimated to be 1.9%, based on the changes induced in the B^+ reconstruction efficiency by weighting the simulated events with different helicity angle distributions. The uncertainty in the B^+ mass shape for the normalization channel is estimated to be 1.0% by adding a third Gaussian function with a common mean and a varying width to the fit, with the background again modeled by a linear function. The uncertainty in $\mathcal{B}(\phi \to K^+K^-)$ is 1% [66].

Possible systematic uncertainties introduced by different trigger and pileup conditions and analysis selections have been investigated by dividing the data into subsets and evaluating the statistical consistency of the independent samples; the

Table 4.10: Helicity angle definitions in two body subsystems of $B^+ \to \psi(2S)\phi K^+$ three body decay.

Two body subsystem considered	Helicity angle definition
$\psi^{'}\phi$	$\Theta^*_{\psi^{'}\phi} = arccos(\frac{V_{\psi^{'}}.V_{\psi^{'}\phi}}{\lvert V_{\psi^{'}}\rvert\lvert V_{\psi^{'}\phi}\rvert})$
$\psi^{'}K$	$\Theta^*_{\psi^{'}K} = arccos(\frac{V_{\psi^{'}}.V_{\psi^{'}K}}{\lvert V_{\psi^{'}}\rvert\lvert V_{\psi^{'}K}\rvert})$
ϕK	$\Theta^*_{\phi K} = arccos(\frac{V_{\phi}.V_{\phi K}}{\lvert V_{\phi}\rvert\lvert V_{\phi K}\rvert})$

resulting variations are found to be within the expected uncertainties.

We estimated the systematic uncertainty due to possible $\psi(2S)\phi$ polarization by re-weighting signal MC using different helicity angle distributions in the $\psi(2S)\phi$ system, for instance, $(1 + cos^2(\Theta^*))$, $cos^2(\Theta^*)$, $(1 + sin^2(\Theta^*))$, and $sin^2(\Theta^*)$; where Θ^* is the helicity angle defined as the angle between $\psi(2S)$ momentum vector and $\psi(2S)\phi$ momentum vector in the rest frame of $\psi(2S)\phi$ system. Table 4.10 shows the helicity angle definitions for all possible two body systems in $B^+ \to \psi(2S)\phi K^+$ three body decay.

Figure 4.24(a) shows the $cos(\Theta^*_{\psi^{'}\phi})$ distribution at generator level for $psi(2S)\phi$ system. We removed the B^+ multiple Candidates at generator level by retaining the one with highest B^+ transverse momentum. We also investigated the polarization systematics in $\psi(2S)K$ and ϕK systems. Figure 4.24(b)&(c) shows the $cos(\Theta^*_{\psi^{'}K})$ distribution at generator level for $\psi(2S)K$ and $cos(\Theta^*_{\phi K})$ distribution at generator level for ϕK systems respectively.

The total systematic uncertainty on branching fraction measurement is reported in section 4.11.9.3.

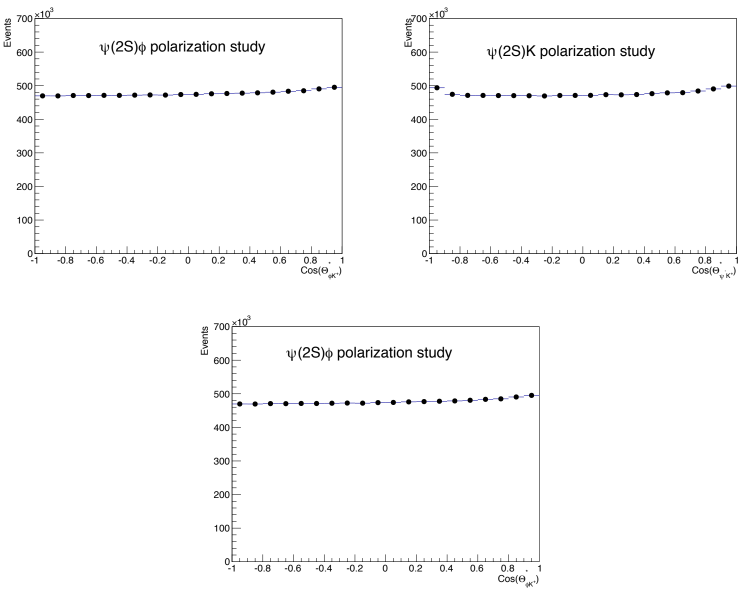

Figure 4.24: Polarization study.

Table 4.11: Reweighted signal MC reconstruction efficiency for different cos(helicityangle) distributions.

	$\psi(2S)\phi$ polarization study		$\psi(2S)K$ polarization study		ϕK polarization study	
Weight of the cos(HelicityAngle) distribution	ε_{Reco}	%Variation	ε_{Reco}	%Variation	ε_{Reco}	%Variation
Default	1.849×10^{-3}	N/A	1.849×10^{-3}	N/A	1.849×10^{-3}	N/A
$cos^2(\Theta^*)$	1.841×10^{-3}	0.4	1.821×10^{-3}	1.5	1.841×10^{-3}	0.4
$1 + cos^2(\Theta^*)$	1.847×10^{-3}	0.1	1.842×10^{-3}	0.4	1.847×10^{-3}	0.1
$sin^2(\Theta^*)$	1.853×10^{-3}	0.2	1.863×10^{-3}	0.8	1.852×10^{-3}	0.2
$1 + sin^2(\Theta^*)$	1.850×10^{-3}	0.1	1.854×10^{-3}	0.3	1.850×10^{-3}	0.1

The overall relative systematic uncertainty in $\mathcal{B}(B^+ \to \psi(2S)\phi K^+)$ is 15% from adding the individual contributions summarized in Table 4.12 in quadrature. The total uncertainty in $\mathcal{B}(B^+ \to \psi(2S)K^+)$ is 3.8% [66]. Thus, the final measured value of $\mathcal{B}(B^+ \to \psi(2S)\phi K^+)$, including all systematic uncertainties, is: $(4.0 \pm 0.4\ (\text{stat.}) \pm 0.6\ (\text{syst.}) \pm 0.1) \times 10^{-6}$, where the third uncertainty is from the imprecision in the $\mathcal{B}(B^+ \to \psi(2S)K^+)$ measurement.

Table 4.12: Relative systematic uncertainties in the measurement of $\mathcal{B}(B^+ \to \psi(2S)\phi K^+)$ in percent. The total systematic uncertainty corresponds to the sum in quadrature of the listed uncertainties.

Source	Uncertainty (%)
B^+ mass shape for signal mode	8.6
Charged particle track reconstruction efficiency	7.8
Modeling of p_T dependence of B^+ efficiency	5.3
ϕ purity	5.0
Mass distribution for the background in the signal	2.9
Uncertainty in relative efficiency of signal and normalization	2.3
Background distribution in the normalization channel	2.2
Angular distributions of K^+K^- systems	1.9
B^+ mass shape for normalization mode	1.0
$\mathcal{B}(\phi \to K^+K^-)$ uncertainty	1.0
Total	15

4.11.9.1 Upper Limit on non ϕ events with 95% Confidence level

We have two non ϕ components: one is f_0 and the other is non-resonant K^+K^- that can pass required event selection criteria as described in section 4.11.2. The shapes of these two components are very similar as shown in Figure 4.7, so we considered only one component (non-resonant K^+K^- shape) to represent these two components; we call it non-ϕ component.

The simultaneous fit shown in Figure 4.12 returned a non-ϕ yield of 2 ± 20 events and is set to be default in calculating the 95% confidence level upper limit. We varied (scanned) the non-ϕ component and the corresponding log likelihood value returned from the simultaneous fit are tabulated as shown in Table 4.13.

Table 4.13: -log likelihood simultaneous fit returned values w.r.t number of Non ϕ events.

Number of Non ϕ events	-log likelihood simultaneous fit result
2	11095.1 (Default)
10	11095.0
20	11094.7
30	11094.2
40	11093.5
50	11092.6

We plotted -2(ΔlnL) vs number of non-ϕ events as shown in Fig. 4.25. The 95% confidence level (where the -2lnL increases by 1.64×1.64) [67] returns 37 non-ϕ events. Since we have 140 total B^+ events in the data as shown in Figure 4.15, the 95% confidence level upper limit for non-ϕ component fraction in the selected $B^+ \to \psi(2S)K^+K^-K+$ decay channel is $\frac{37}{140} = 26\%$.

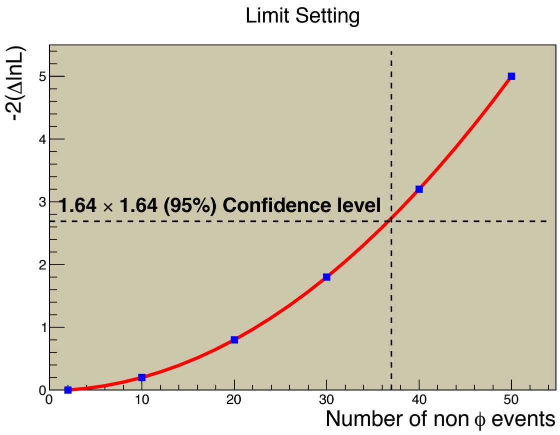

Figure 4.25: 95% Confidence level upper limit on non ϕ components.

4.11.9.2 Systematic from PDG

We take the BF of $B^+ \to \psi(2S)K^+$ ($(6.27 \pm 0.24) \times 10^{-4}$) from PDG. However, we find that the scaled error from the BF contribute a percent uncertainty of 3.8% to our branching fraction measurement and thus we label it as BF.

4.11.9.3 The BF with Systematics

The measured BF of $B^+ \to \psi(2S)\phi K^+$, including all systematics, can be expressed as: $(4.0 \pm 0.4(stat.) \pm 0.5(syst.) \pm 0.1) \times 10^{-6}$, where the third uncertainty is due to imprecise knowledge of BF.

4.12 Summary of the first observation of $B^+ \to \psi(2S)\phi K^+$

The B meson state carries heavy flavor bottom quark. The $B^\pm$ meson is clearly observed by CMS in the decay $B^\pm \to \psi(2S)\phi K^\pm$. Using 20 fb^{-1} of pp collision data at 8 TeV, after all cuts, the total number of observed signal events is $140 \pm 15(stat.)$ over a background of $624 \pm 27(stat.)$, which is the world's largest signal yield up to today with a significance over five standard deviations. For the first time, we observed the $B^+ \to \psi(2S)\phi K^+$ with a statistical significance of 12.7 standard deviations. Including systematics, the BF of $B^+ \to \psi(2S)\phi K^+$ is determined to be $(4.0 \pm 0.4\ \text{(stat.)} \pm 0.6\ \text{(syst.)} \pm 0.1) \times 10^{-6}$.

CHAPTER 5
SHOWER DEVELOPMENT STUDIES IN HADRONIC CALORIMETERS

5.1 Introduction

Calorimetry is a well understood measurement method used at high-energy particle physics experiments. Physicists are still developing novel techniques in perfecting this method to match with the increasing demand of new experiments planned, under construction in various research labs around the world. A calorimeter is a detector for energy measurement via total absorption of particles. Calorimeters are position sensitive to measure energy depositions depending on their location. A calorimeter measures energy either homogeneously or by sampling. Sampling calorimeters consist of alternating layers of an absorber, a dense material used to degrade the energy of the incident particle, and an active medium that provides the detectable signal. Homogeneous calorimeters, on the other hand, are built of only one type of material that performs both tasks, energy degradation and signal generation. The principle operation of a calorimeter is an incoming particle initiates shower (particle cascade) in a detector material depositing energy in the form of heat, ionization, excitation of atoms, Cherenkov light, etc. Shower composition and dimensions depend on particle type and detector material. Calorimeters can measure the energy of both charged and neutral particles, if they interact via electromagnetic or strong forces.

Sampling calorimeters consist of two different elements, normally in a sandwich geometry: (i) layers of active material (collection of signal) such as gas, scintillator, etc (ii) layers of passive material (shower development). Typical elements used as calorimeter passive and active material are shown in Table 5.1. A few advantages of building sampling calorimeters are: segmentation allows measurement of spatial coordinates, can be very compact, simple geometry, relatively cheap to construct, sampling concept can be used in either electromagnetic or hadronic calorimeter, only part of the energy is sampled in the active medium.

The key parameters of a calorimeter are linearity and resolution. This chapter summarizes the performance of calorimeters in terms of the elementary physics processes and designing/developing new and better calorimetric techniques. These studies were initiated as a search for possible techniques for very high resolution jet calorimetry. They have evolved into the fundamental studies of the principles of sampling and total absorption calorimetry. They are of significant interest for various practical applications (as a guide or as a tool) for the application specific simulations: for instance LHC upgrades.

Table 5.1: Typical elements used as calorimeter passive and active material.

Passive	Pb, W, U, Fe
Active	Scintillator slabs, scintillator fibers, silicon detectors, LAr, LXe

5.2 Simulated Detector configurations

Dual readout calorimeter, which measures both energy and time is simulated using the Calorimeter and Tracker Simulation (CaTs) [68] framework in GEANT4. CaTs (based on Geant4 and ROOT) provides hit classes that register both energy deposit and the number of photons produced in the Cerenkov radiation by particles travelling with the speed greater than the speed of light in the calorimeter, and allows detailed study of calorimeter single cells by enabling the tracing of optical photons. Geometry description markup language (Gdml) is used to simulate any shape and any size of a detector. Gdml description of a detector allows to provide all relevant optical properties of scintillation.

Different calorimeter geometries are generated for input beam of e^-, n, π^- and p particles as shown in Tables 5.2, 5.3, 5.4, 5.5 with energy: 0.002, 0.005, 0.01, 0.02, 0.05, 0.1, 0.2, 0.5, 1, 2, 5, 10, 20, 50, 100 GeV. The symbolic notations used in describing the calorimeter geometry are as follows:

- Incoming particle energy: E
- Number of logitudinal planes: N_z
- Absorber thickness: Abs_th
- Scintillator thickness: Sc_th
- Number of transverse segments: N_{trans}
- Size of transverse segments: S_{trans}
- The fundamental longitudinal cell thickness: d_z =Abs_th+Sc_th

- The detector limits will be from $z_{min} = \frac{-N_z}{2} \times d_z$ to $z_{max} = \frac{N_z}{2} \times d_z$ and $\frac{-N_{trans}}{2} \times S_{trans}$ to $\frac{N_{trans}}{2} \times S_{trans}$

Table 5.2: Simulated Sampling Calorimeter Detector Configurations with input e^- beam.

Number of Z (logitudinal) planes	Sampling Calorimeter (Absorber+Scintillator)	Thickness of the fundamental logitudinal cell
100	BGO+BGO MetalIron + Scintillator MetalPb + Scintillator	18.0 + 2.0 = 20 mm 20.0 + 5.0 = 25 mm 20.0 + 5.0 = 25 mm
250	BGO + BGO MetalIron + Scintillator MetalIron + BGO MetalPb + Scintillator	7.2 + 0.8 = 8.0 mm 8.0 + 2.0 = 10.0 mm 8.0 + 1.4 = 9.4 mm 8.0 + 2.0 = 10.0 mm
500	BGO + BGO MetalIron + Scintillator MetalPb + Scintillator	3.6 + 0.4 = 4 mm 4.0 + 1.0 = 5 mm 4.0 + 1.0 = 5 mm

Histograming the total energy deposited per event in the absorber and in the scintillator followed by fitting the histogram peak using a Gaussian model allows estimating the mean deposited energy, which is the response of the calorimeter, and the resolution calculated using fit parameters as $\frac{\sigma}{MeanEnergy}$. A typical fit, for electrons at 20 GeV, is shown in Fig. 5.1.

Table 5.3: Simulated Sampling Calorimeter Detector Configurations with input neutron beam.

Number of Z (logitudinal) planes	Sampling Calorimeter (Absorber+Scintillator)	Thickness of the fundamental logitudinal cell
100	MetalIron + Scintillator MetalPb + Scintillator	20.0 + 5.0 = 25 mm 20.0 + 5.0 = 25 mm
250	MetalIron + Scintillator MetalIron + BGO MetalPb + Scintillator	8.0 + 2.0 = 10.0 mm 8.0 + 1.4 = 9.4 mm 8.0 + 2.0 = 10.0 mm
500	BGO + BGO_FTFP_BERT_HP MetalIron + Scintillator MetalPb + Scintillator	3.6 + 0.4 = 4.0 mm 4.0 + 1.0 = 5 mm 4.0 + 1.0 = 5 mm

Table 5.4: Simulated Sampling Calorimeter Detector Configurations with input π^- beam.

Number of Z (logitudinal) planes	Sampling Calorimeter (Absorber+Scintillator)	Thickness of the fundamental logitudinal cell
100	BGO + BGO	18.0 + 2.0 = 20 mm
250	BGO + BGO	7.2 + 0.8 = 8.0 mm
500	BGO + BGO	3.6 + 0.4 = 4 mm

Table 5.5: Simulated Sampling Calorimeter Detector Configurations with input proton beam.

Number of Z (logitudinal) planes	Sampling Calorimeter (Absorber+Scintillator)	Thickness of the fundamental logitudinal cell
100	BGO + BGO MetalIron + Scintillator MetalPb + Scintillator	18.0 + 2.0 = 20 mm 20.0 + 5.0 = 25 mm 20.0 + 5.0 = 25 mm
250	BGO + BGO MetalIron + Scintillator MetalIron + BGO MetalPb + Scintillator	7.2 + 0.8 = 8.0 mm 8.0 + 2.0 = 10.0 mm 8.0 + 1.4 = 9.4 mm 8.0 + 2.0 = 10.0 mm
500	BGO + BGO MetalIron + Scintillator MetalPb + Scintillator	3.6 + 0.4 = 4 mm 4.0 + 1.0 = 5 mm 4.0 + 1.0 = 5 mm

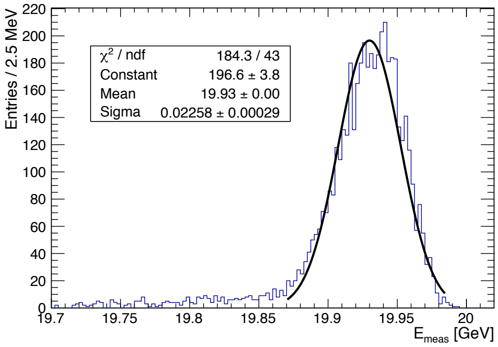

Figure 5.1: An example of a Gaussian fit to the measured energy, for recorded hit data using an electron beam at 20 GeV. Such fits are used to estimate the mean response and energy resolution of the calorimeter.

5.3 BGO+BGO calorimeter energy response and resolution

In BGO+BGO calorimeter both active and passive materials are the same; thus, it can be used as both a total absorption calorimeter as well as a sampling calorimeter. Figure 5.2(a) and (b) show the linearity and the resolution using histogram mean and RMS parameters, respectively, as a function of energy for simulated e^-, π^-, and p beams in total absorption calorimeter at normal incidence, with energies 1 − 100 GeV. Similarly, the linearity and the resolution plots for the sampling calorimeter are shown in Fig. 5.3(a) and (b), respectively.

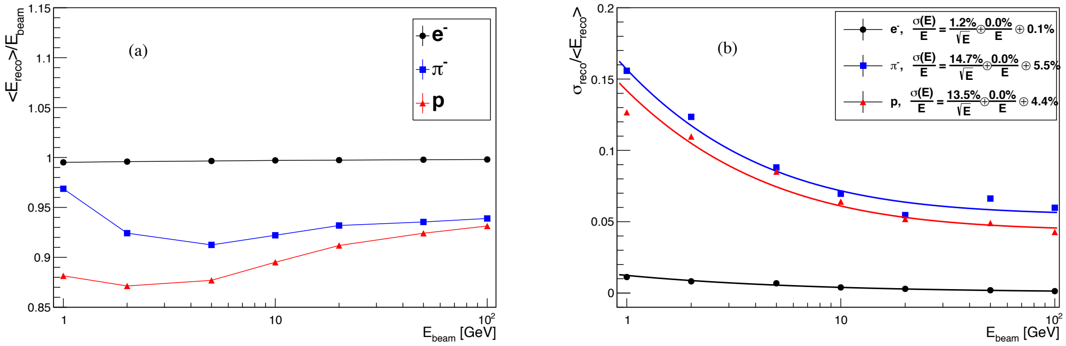

Figure 5.2: Response (a) and resolution (b) of the BGO + BGO total absorption calorimeter, divided by beam energy, plotted as a function of beam energy, using histogram parameters. The plot relates to e^-, π^-, and p beams simulation data generated at normal incidence, with energies 1 − 100 GeV.

In total absorption calorimeter, at low energies the p reconstructed energy has about a 12% deviation with respect to the true energy. For e^-, at low and high energies the deviation of the reconstructed from the true energy is within 1%, and for π^-, the deviation is about 7% at high energies. An observation of the rise in π^+

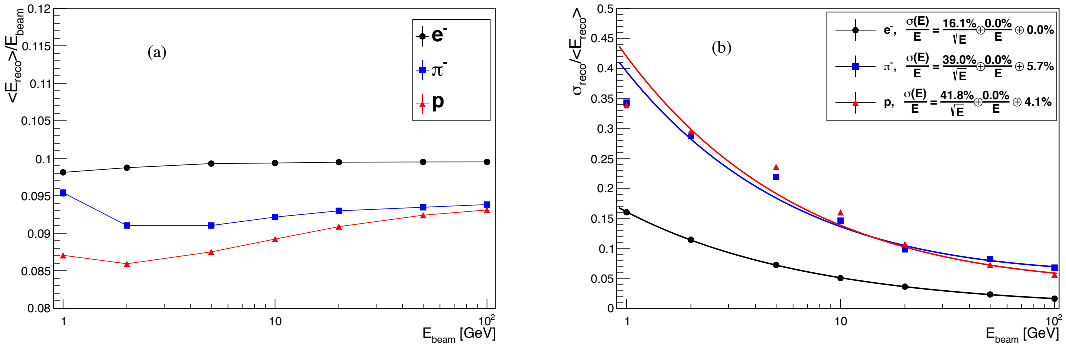

Figure 5.3: Response (a) and resolution (b) of the BGO + BGO sampling calorimeter, divided by beam energy, plotted as a function of beam energy, using histogram parameters. The plot relates to e^-, π^-, and p beams simulation data generated at normal incidence, with energies 1 – 100 GeV.

reconstructed energy close to the true energy with a deviation of 4% at low energies (at 1 GeV beam energy, the 4% deviation on deposited energy is about 40 MeV comes from the π^- decay) indicates that this rise in energy deposition is coming from the $\pi^- \to \mu^-\bar{\nu}_\mu$ and $\mu^- \to e^-\bar{\nu}_e$ decays, the daughter particles μ^-, e^- deposite a fraction of their kinetic energy. The measurement of the 2 MeV π^- energy deposition (π^- decay energy) is shown in Fig. 5.4. However, this 40 MeV additional energy contribution at higher energies (2 - 100 GeV) is negligible in comparision to the beam energy. For π^-, and p, the resolution varies from ≈15% at 1 GeV and ≈7% at 100 GeV in the total absorption calorimeter, where as in sampling calorimeter, the π^-, and p resolutions varies from ≈35% at 1 GeV and ≈11% at 100 GeV.

The energy resolution may be parameterized as:

$$\frac{\sigma}{E} = \frac{s}{\sqrt{E}} \oplus \frac{n}{E} \oplus c \tag{5.1}$$

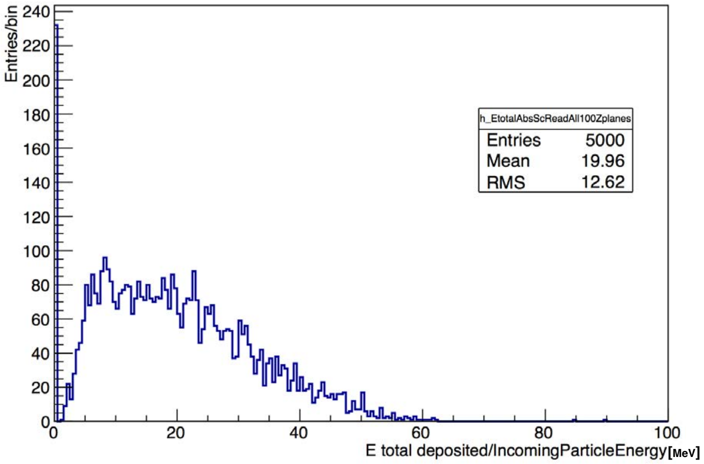

Figure 5.4: Measured energy distribution for a 2 MeV π^- beam. The 40 MeV mean energy is due to the π^- decays.

where the symbol $\oplus$ denotes a quadratic sum. The first term is the *stochastic term*, the second denotes the *noise term* and the third one is the *constant term* [69]. This function is fitted to the energy resolution for the energies of $1-100$ GeV, and the fit returned sampling terms and constant terms for various single particle beams, are shown in Table 5.6.

Table 5.6: Stochastic terms and constant terms from the BGO+BGO total absorption and sampling calorimeters energy resolution fits.

Single particle beam	Total absorption calorimeter		sampling calorimeter	
	$\frac{s}{\sqrt{E}}$	c	$\frac{s}{\sqrt{E}}$	c
e^-	$\frac{1.2\%}{\sqrt{E}}$	0.1%	$\frac{16.1\%}{\sqrt{E}}$	0.0%
π^-	$\frac{14.7\%}{\sqrt{E}}$	5.5%	$\frac{39.0\%}{\sqrt{E}}$	5.7%
p	$\frac{13.5\%}{\sqrt{E}}$	4.4%	$\frac{41.8\%}{\sqrt{E}}$	4.1%

Figures 5.10(a) and 5.16(a) show that the p has higher visible energy than n. This is due to the fact that p has electric charge and deposits energy by two processes; first through the electromagnetic interaction, and the second through the hadronic interaction, where as n is charge-less, deposits energy only through hadronic interaction. The higher the initial beam energy, the higher the energy spent (Q-value) in hadronic interaction; in other words, larger the deviation of the reconstructed energy from the true energy.

The stochastic and constant term contribution to the energy resolution as a function of sampling frequency is studied for both total absorption and sampling BGO+BGO calorimeters as shown in Fig 5.5 and Fig 5.6, respectively.

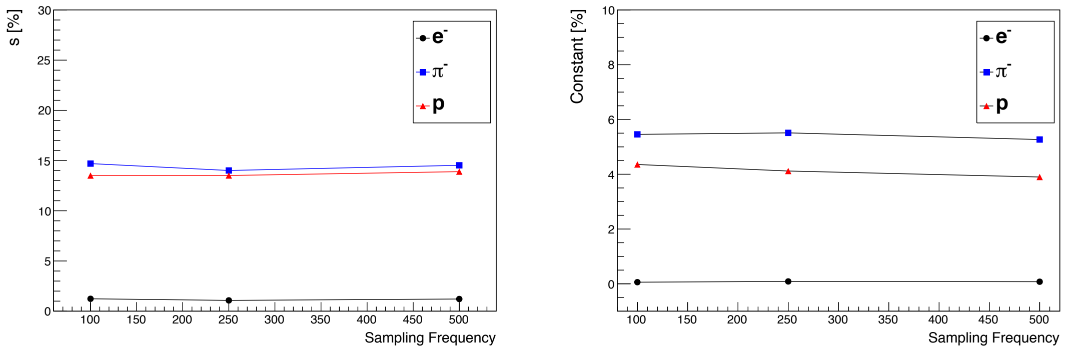

Figure 5.5: The stochastic (a) and constant term (b) of the BGO + BGO total absorption calorimeter as a function of sampling frequency. The plot relates to e^-, π^-, and p beams simulation data generated at normal incidence, with energies $1-100$ GeV.

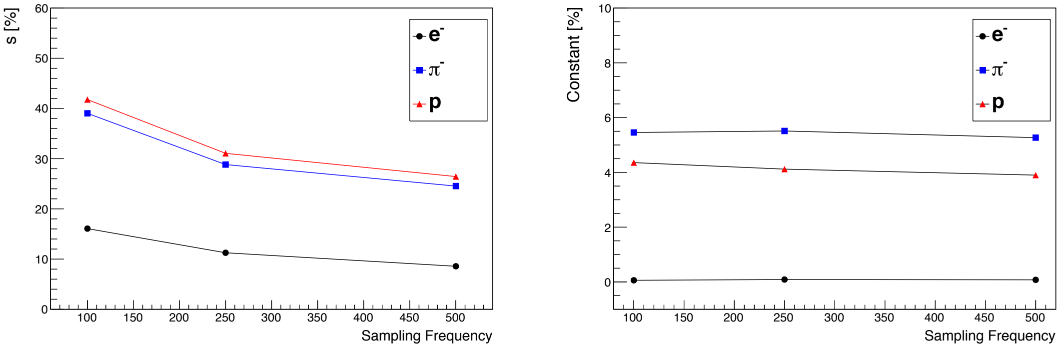

Figure 5.6: The stochastic (a) and constant term (b) of the BGO + BGO total sampling calorimeter as a function of sampling frequency. The plot relates to e^{-}, π^{-}, and p beams simulation data generated at normal incidence, with energies $1-100$ GeV.

The sampling fraction f_{samp} parameter of sampling calorimeter defined as:

$$f_{\text{samp}} = \frac{< E_{reco} > (active)}{< E_{reco} > (active) + < E_{reco} > (absorber)} \tag{5.2}$$

where $< E_{reco} >$(active) and $< E_{reco} >$(absorber) indicate the energies deposited by an incident beam particles in the active part and in the absorber part of the detector respectively. The f_{samp} as a function of beam energy for various sampling frequencies are shown in Fig. 5.7(a) 100 z planes (b) 250 z planes, and (c) 500 z planes, respectively, in BGO+BGO sampling calorimeter for e^{-}, π^{-}, and p beams with energies $1-100$ GeV.

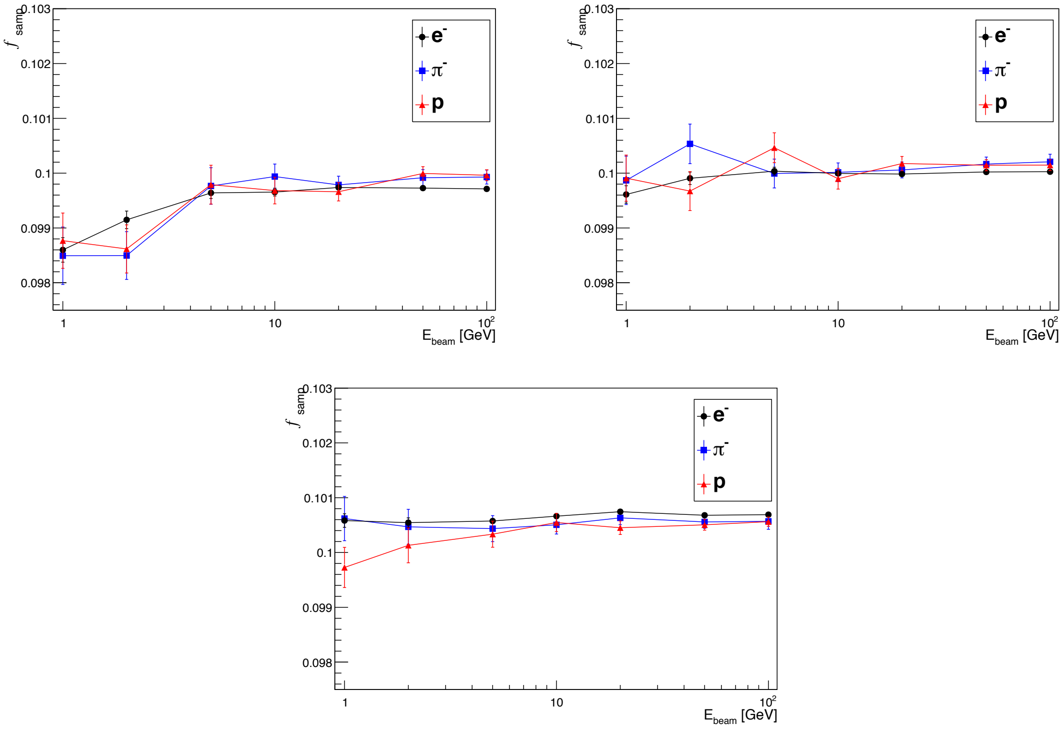

Figure 5.7: Sampling fraction as a function of beam energy for various sampling frequencies of (a) 100 z planes (b) 250 z planes, and (c) 500 z planes in BGO+BGO sampling calorimeter, using histogram parameters. The plot relates to e^-, π^-, and p beams simulation data generated at normal incidence, with energies $1 - 100$ GeV.

5.4 BGO+BGO calorimeter energy resolution as a function of sampling frequency

The Data Acquisition System (DAQ) is needed for reading energy deposit information in any hadronic calorimeter. The cost of building a hadronic calorimeter depends on the amount of readout electronics required; more the readouts (higher the sampling frequency) higher the cost, and better the detector resolution. A simulation study of the energy resolution vs sampling frequency is used to fix the DAQ system readouts for the requirement of energy resolution at the design time of a hadronic calorimeter.

We study the energy resolution as a function of sampling frequency, the fraction of the detector read in the total absorption calorimeter BGO+BGO with fundamental thickness 18 (Abs) + 2 (Sc) = 20 mm in the configurations of 100, 250, and 500 Z planes. For clarity, if we read the energy deposits from the whole 100 Scintillator Z planes then we have read 10% of the detector. Similarly reading all Absorbers Z planes means reading 90% of the detector, and reading all Absorbers + Scintillators Z planes means reading 100% of the detector. Table 5.7 describes the sampling frequencies considered and their corresponding fractions of the detector readout (Z=100 planes detector with (18+2=20mm) fundamental thickness).

The energy resolution as a function of sampling frequency by keeping the sampling fraction fixed to 18% of the total detector readout in BGO+BGO calorimeter is shown in Fig. 5.9.

Table 5.7: Sampling frequencies (fraction of the detector readouts) considered for Z=100 planes BGO+BGO detectors.

Sampling frequency	% of the detector read
Reading every 10th Sc plane of total 10 planes	1.0%
Reading every 5th Sc plane of total 20 planes	2.0%
Reading every 4th Sc plane of total 25 planes	2.5%
Reading every 3rd Sc plane of total 33 planes	3.3%
Reading every 2nd Sc plane of total 50 planes	5.0%
Reading All 100 Sc planes	10.0%
Reading every 5th Abs plane of total 20 planes	18.0%
Reading every 4th Abs plane of total 25 planes	22.5%
Reading every 3rd Abs plane of total 33 planes	30.0%
Reading every 2nd Abs plane of total 50 planes	45.0%
Reading every 2nd Abs+Sc plane of total 50 fundamental cells	50.0%
Reading All 100 Abs planes	90.0%
Reading All 100 Abs+Sc planes	100.0%

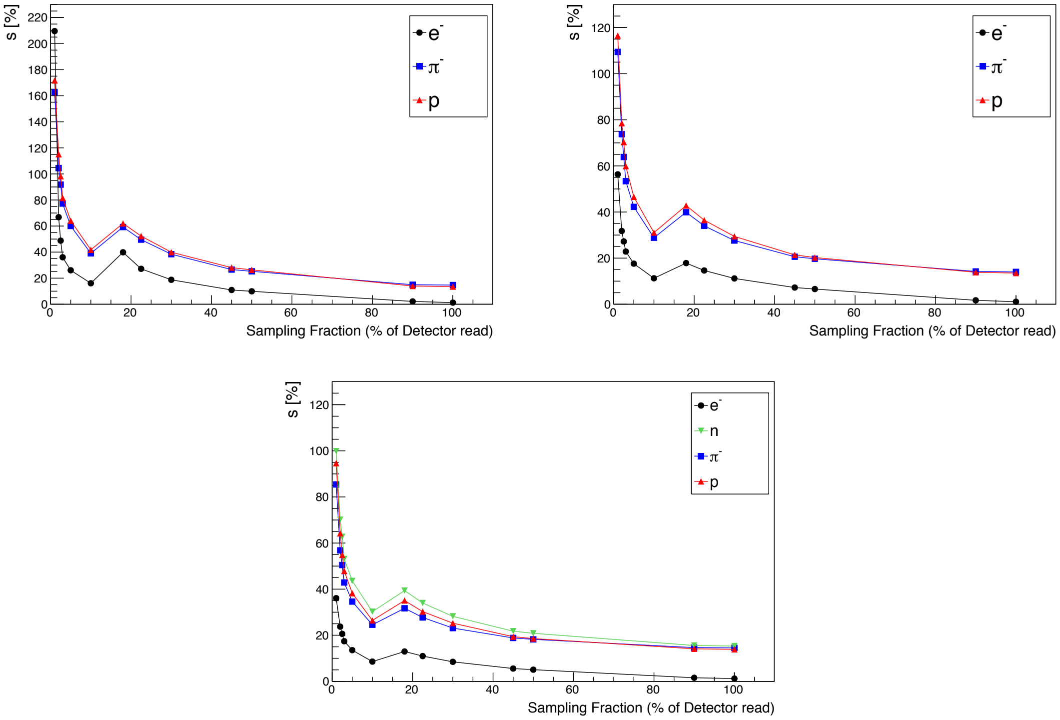

Figure 5.8: Stochastic term as a function of sampling frequency in (a) 100 Z planes (b) 250 Z planes, and (c) 500 Z planes of BGO+BGO total absorption calorimeter, using histogram parameters. The plot relates to e^-, π^-, n, and p beams simulation data generated at normal incidence, with energies $1-100$ GeV.

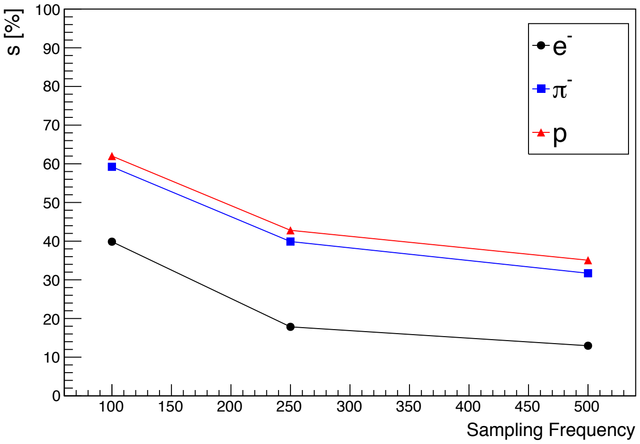

Figure 5.9: Energy resolution as a function of sampling frequency at a sampling fraction fixed to 18% of detector readout, for particles e^-, π^-, and p in BGO+BGO total absorption calorimeter.

5.5 Metal Iron + Scintillator energy response and resolution

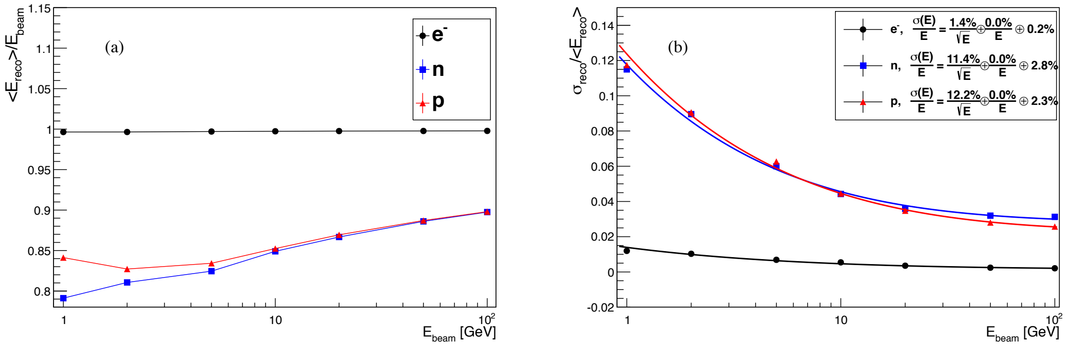

Figure 5.10: Response (a) and resolution (b) of the MetalIron + Scintillator total absorption calorimeter, divided by beam energy, plotted as a function of beam energy, using histogram parameters. The plot relates to e^{-}, n, and p beams simulation data generated at normal incidence, with energies $1-100$ GeV.

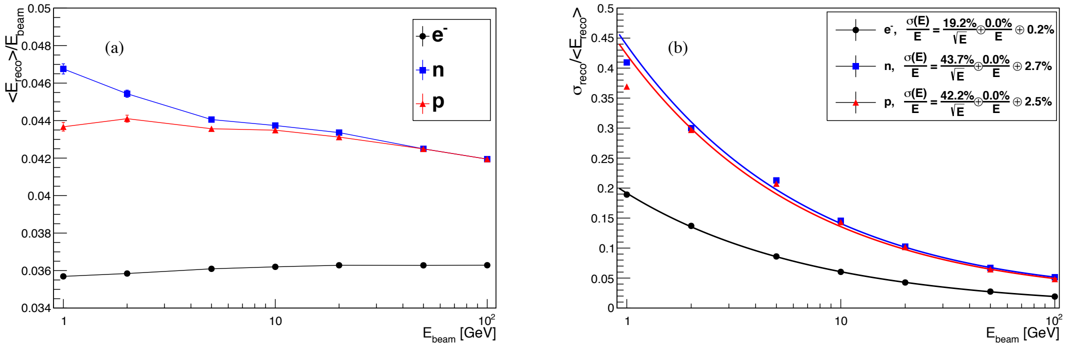

Figure 5.11: Response (a) and resolution (b) of the MetalIron + Scintillator sampling calorimeter, divided by beam energy, plotted as a function of beam energy, using histogram parameters. The plot relates to e^{-}, n, and p beams simulation data generated at normal incidence, with energies $1-100$ GeV.

The f_{samp} as a function of beam energy for various sampling frequencies are

shown in Fig. 5.12(a) 100 z planes (b) 250 z planes, and (c) 500 z planes, respectively, in Metal Iron + Scintillator sampling calorimeter for e^{-}, π^{-}, and p beams with energies $1 - 100$ GeV.

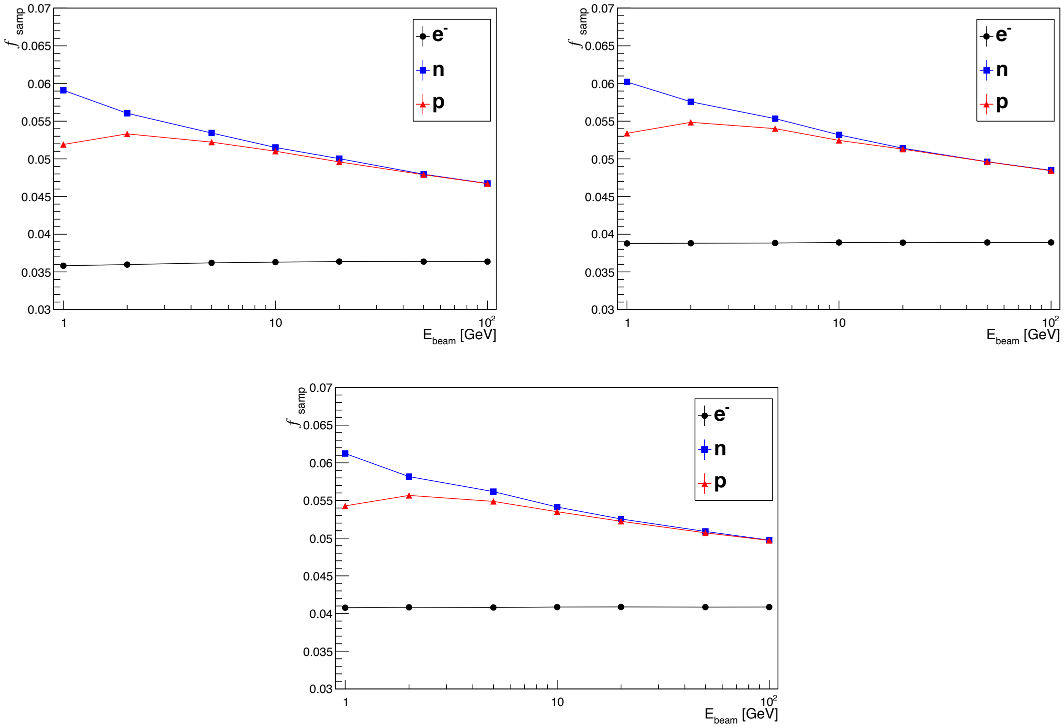

Figure 5.12: Sampling fraction as a function of beam energy for various sampling frequencies of (a) 100 z planes (b) 250 z planes, and (c) 500 z planes in Metal Iron + Scintillator sampling calorimeter, using histogram parameters. The plot relates to e^{-}, n, and p beams simulation data generated at normal incidence, with energies $1 - 100$ GeV.

5.6 Metal Iron + BGO energy response and resolution

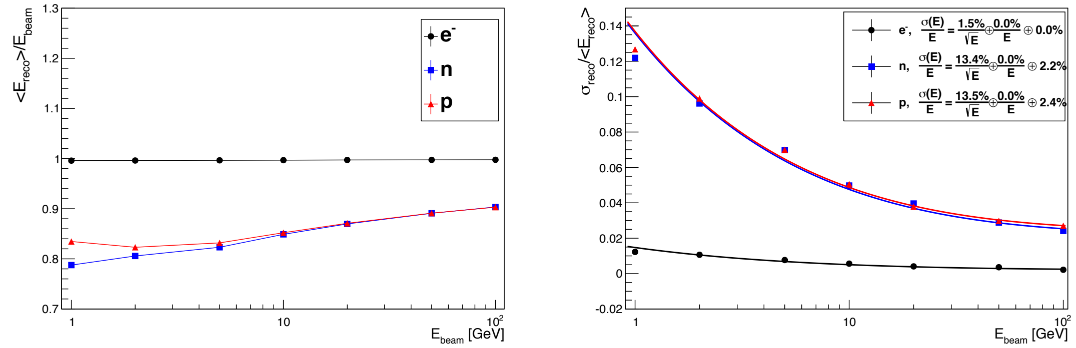

Figure 5.13: Response (a) and resolution (b) of the MetalIron + BGO total absorption calorimeter, divided by beam energy, plotted as a function of beam energy, using histogram parameters. The plot relates to e^-,n, and p beams simulation data generated at normal incidence, with energies $1 - 100$ GeV.

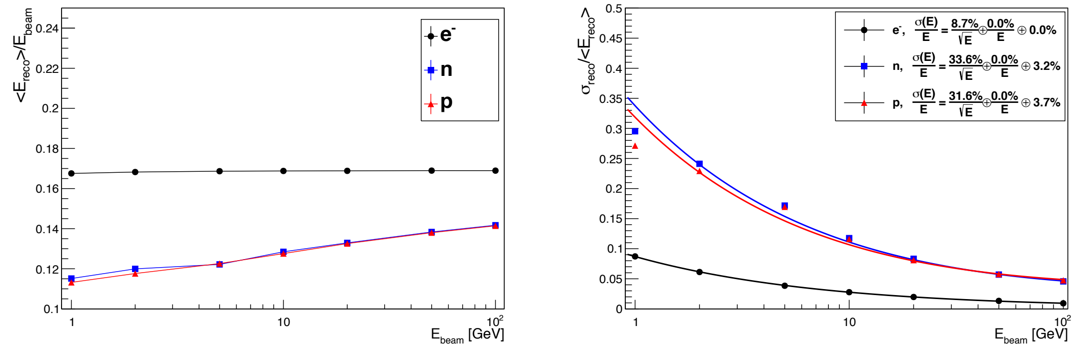

Figure 5.14: Response (a) and resolution (b) of the MetalIron + BGO sampling calorimeter, divided by beam energy, plotted as a function of beam energy, using histogram parameters. The plot relates to e^-, n, and p beams simulation data generated at normal incidence, with energies $1 - 100$ GeV.

The f_{samp} as a function of beam energy for various sampling frequencies are

shown in Fig. 5.15 250 z planes in Metal Iron + BGO sampling calorimeter for e^-, n, and p beams with energies $1 - 100$ GeV. An important observation from the Fig. 5.12 and Fig. 5.15 is that the sampling fraction ratio of $\frac{hadrons}{electron}$ is less than one in case of non-hydrogen sampling material (BGO) and is greater than one in case of hydrogen sampling material (Plastic Scintillator). Hadrons entering into the plastic scintillator produce soft neutrons, which undergo elastic collisions with the hydrogen atoms in the scintillator. Then the soft neutrons come to a complete stop and knock out protons in the scintillator. The newly-released protons with positive charge deposit energy in the scintillator resulting in an energy deposition well above that of the electrons, where as in case of denser BGO sampling calorimeter the soft produced neutrons will not be able to knock out the protons from BGO atoms.

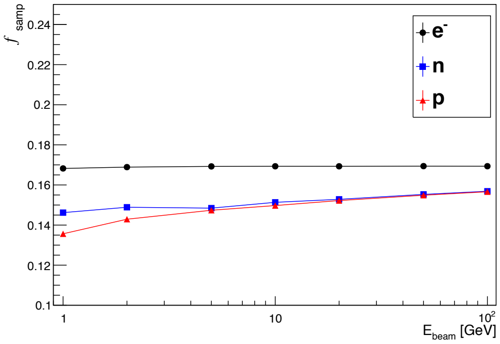

Figure 5.15: Sampling fraction as a function of beam energy for various sampling frequencies of 250 z planes in Metal Iron + BGO sampling calorimeter, using histogram parameters. The plot relates to e^-, n, and p beams simulation data generated at normal incidence, with energies $1 - 100$ GeV.

5.7 Metal Pb + Scintillator energy response and resolution

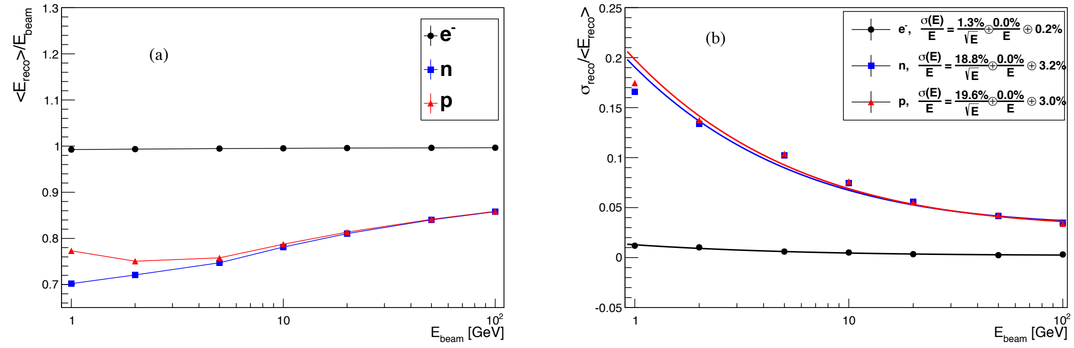

Figure 5.16: Response (a) and resolution (b) of the MetalPb + Scintillator total absorption calorimeter, divided by beam energy, plotted as a function of beam energy, using histogram parameters. The plot relates to e^-, n, and p beams simulation data generated at normal incidence, with energies $1 - 100$ GeV.

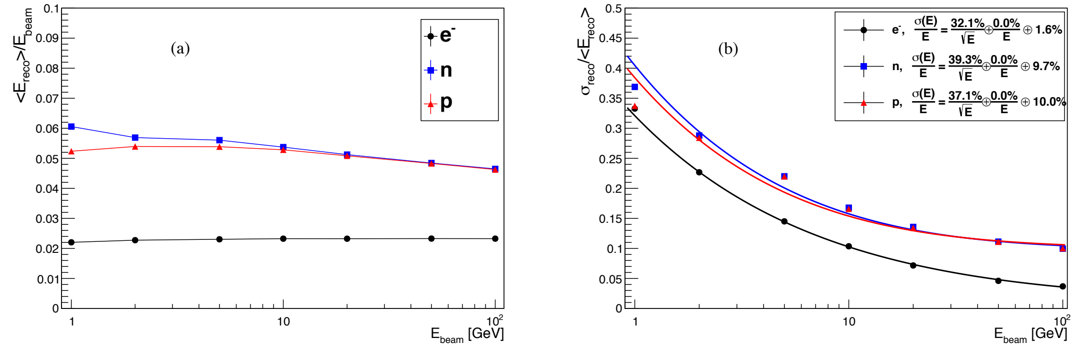

Figure 5.17: Response (a) and resolution (b) of the MetalPb + Scintillator sampling calorimeter, divided by beam energy, plotted as a function of beam energy, using histogram parameters. The plot relates to e^-, n, and p beams simulation data generated at normal incidence, with energies $1 - 100$ GeV.

The f_{samp} as a function of beam energy for various sampling frequencies are

shown in Fig. 5.18(a) 100 z planes (b) 250 z planes, and (c) 500 z planes, respectively, in Metal Pb + Scintillator sampling calorimeter for e^-, n, and p beams with energies $1 - 100$ GeV.

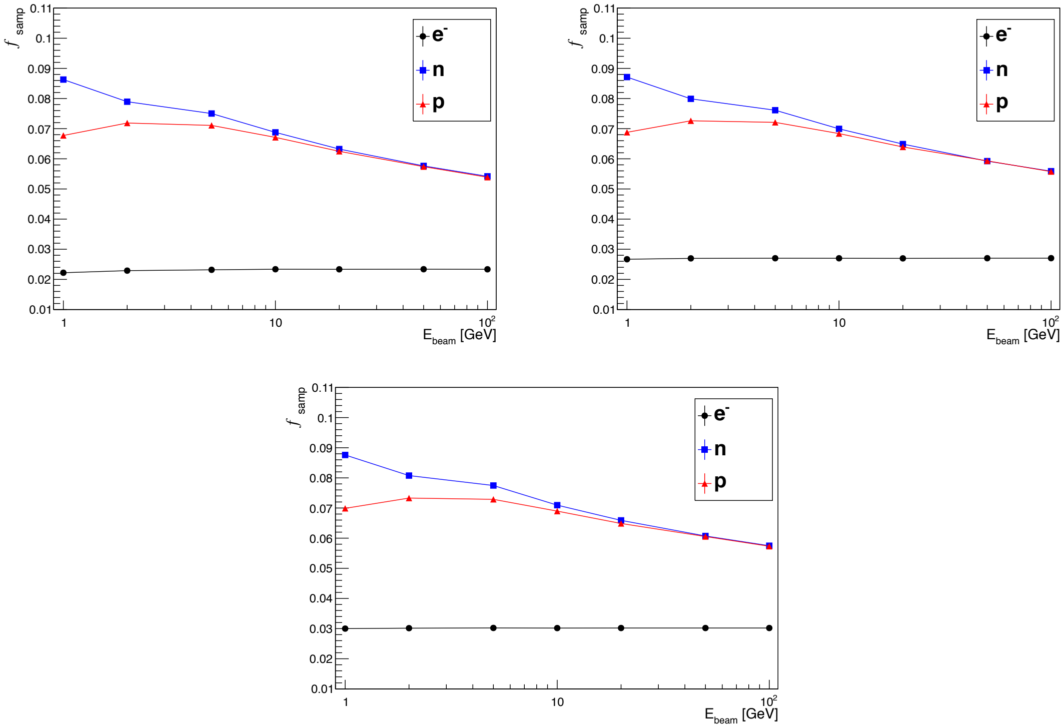

Figure 5.18: Sampling fraction as a function of beam energy for various sampling frequencies of (a) 100 z planes (b) 250 z planes, and (c) 500 z planes in Metal Pb + Scintillator sampling calorimeter, using histogram parameters. The plot relates to e^-, n, and p beams simulation data generated at normal incidence, with energies $1 - 100$ GeV.

5.8 Results and Summary

We performed an energy response and resolution study in simulated sampling calorimeters made of different active and passive elements (BGO+BGO, MetalIron+Sc, and MetalPb+Sc) with e^-, π^-, n, and p beams of energy $1-100$ GeV. A simulation study of the energy resolution compared to sampling frequency is performed to estimate the DAQ system readouts for the requirement of an energy resolution at the design time of a hadronic calorimeter. In the energy resolution of a calorimeter, the stochastic term depends on sampling frequency, higher the sampling rate, better the energy resolution, where as the constant term remains unchanged. The effect on the energy response of a calorimeter on using hydrogen rich scintillator materials compared to non-hydrogen metals as an active material is studied, the energy deposition ratio of $hadron/electron$ is greater than one for plastic scintillators and less than one for BGO metal. In conclusion, as a first exercise, we have measured the linearity and resolution in different hadron calorimeter configurations. Further studies can be done in improving the hadronic calorimeter resolution by implementing the energy leakage correction.

APPENDIX A
CMS FIREWORKS EVENT DISPLAY

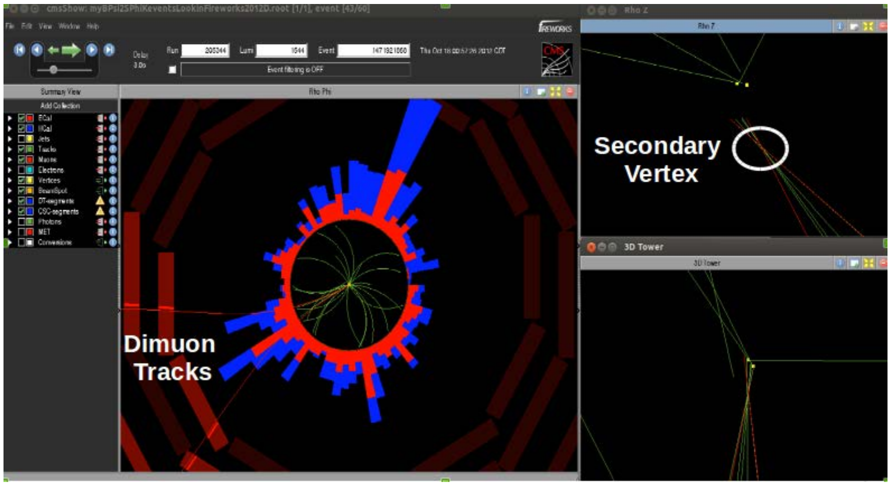

Figure A.1: A possible $B^+ \to \psi(2S)\phi K^+$ candidate event is displayed using CMS fireworks tool.

APPENDIX B
ϕ PURITY STUDY

In order to check if the choice of ϕ candidate causes any bias, we consider both combinations and label them as $(\mathrm{K^+K^-})_{\mathrm{min}}$ and $(\mathrm{K^+K^-})_{\mathrm{max}}$ based on the masses of the two pairs. We generated 479K private Monte Carlo $\mathrm{B^+} \to \psi(2\mathrm{S})\mathrm{f_0K^+}$ events and there are 266 events that passed the event selection requirement resulting the f_0 reconstruction efficiency of 0.0006. For phase space K^+K^- contamination check, we generated 497K private Monte Carlo $\mathrm{B^+} \to \psi(2\mathrm{S})\mathrm{K^+K^-K^+}$ events and there are 300 events that passed the event selection requirement resulting the non-resonant $\mathrm{K^+K^-}$ reconstruction efficiency of 0.0006.

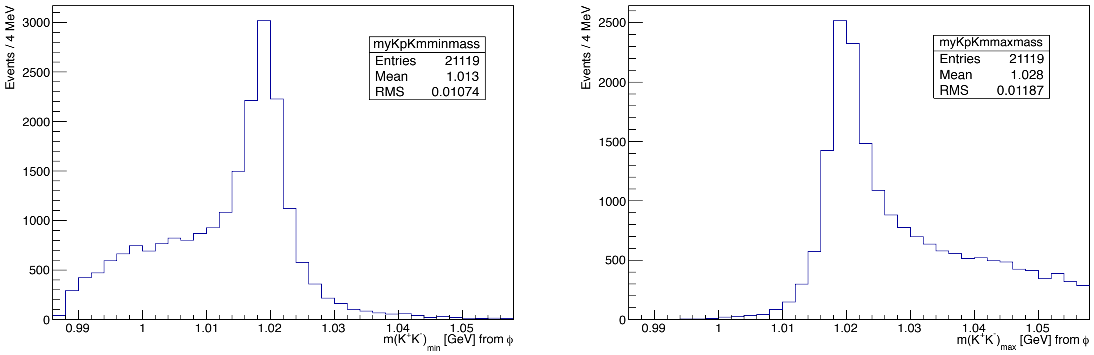

(a) $m(K^+K^-)_{min}$ distribution from Monte Carlo signal sample.

(b) $m(K^+K^-)_{max}$ distribution from Monte Carlo signal sample.

Figure B.1: $(\mathrm{K^+K^-})_{\mathrm{min}}$ and $(\mathrm{K^+K^-})_{\mathrm{max}}$ pairs distribution from $\mathrm{B^+} \to \psi(2\mathrm{S})\phi\mathrm{K^+}$ MC events.

The mass distributions of $(\mathrm{K^+K^-})_{\mathrm{min}}$ and $(\mathrm{K^+K^-})_{\mathrm{max}}$ from Monte Carlo for

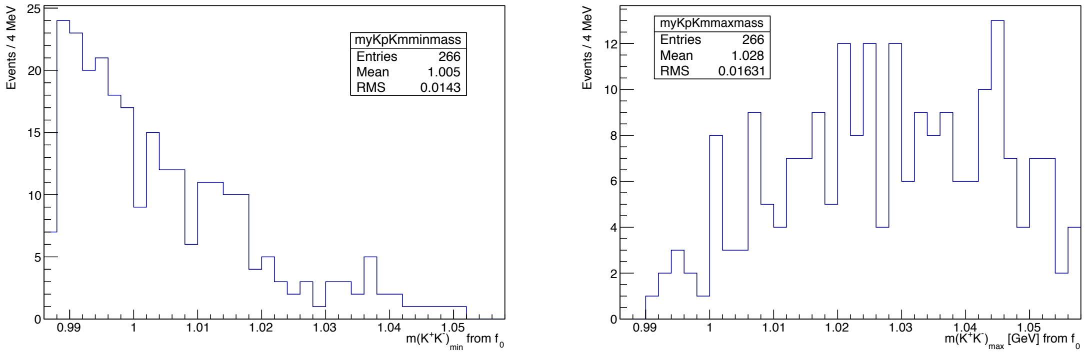

(a) $m(K^+K^-)_{min}$ distribution from Monte Carlo $B^+ \to \psi(2S) f_0 K^+$ sample.

(b) $m(K^+K^-)_{max}$ distribution from Monte Carlo $B^+ \to \psi(2S) f_0 K^+$ sample.

Figure B.2: $(\mathrm{K^+K^-})_{\mathrm{min}}$ and $(\mathrm{K^+K^-})_{\mathrm{max}}$ pairs distribution from $\mathrm{B^+} \to \psi(\mathrm{2S})\mathrm{f_0K^+}$ MC events.

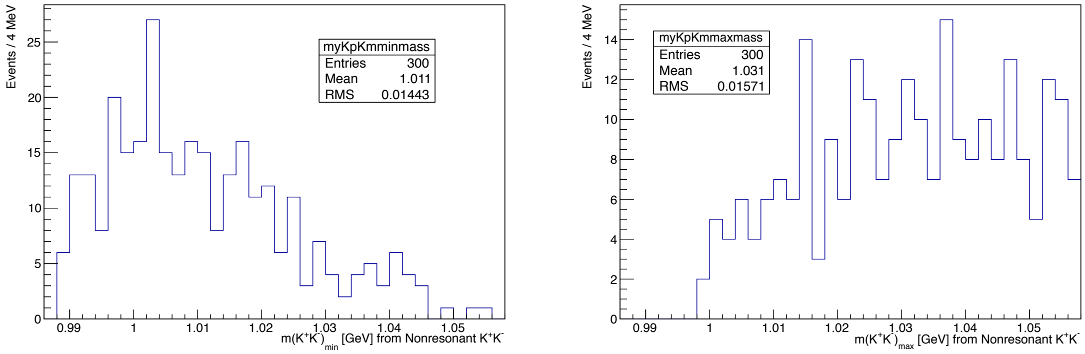

(a) $m(K^+K^-)_{min}$ distribution from Monte Carlo signal sample.

(b) $m(K^+K^-)_{max}$ distribution from Monte Carlo signal sample.

Figure B.3: $(\mathrm{K^+K^-})_{\mathrm{min}}$ and $(\mathrm{K^+K^-})_{\mathrm{max}}$ pairs distribution from $\mathrm{B^+} \to \psi(\mathrm{2S})\mathrm{K^+K^-K^+}$ MC events.

signal sample is shown in Figure B.1, for f_0 sample is shown in Figure B.2, and for nonresonant K^+K^- sample is shown in Figure B.3.

The mass distributions of $(\mathrm{K^+K^-})_{\mathrm{min}}$ and $(\mathrm{K^+K^-})_{\mathrm{max}}$ after non-B background subtraction using the same method are shown in Figure B.4. The $(\mathrm{K^+K^-})_{\mathrm{min}}$ and $(\mathrm{K^+K^-})_{\mathrm{max}}$ mass shapes of $\mathrm{B^+} \to \psi(2\mathrm{S})\phi\mathrm{K^+}$, $\mathrm{B^+} \to \psi(2\mathrm{S})\mathrm{f_0K^+}$, and $\mathrm{B^+} \to \psi(2\mathrm{S})\mathrm{K^+K^-K^+}$ are obtained from MC. We then use TFraction fitter [70] to find out the fraction of each component. Table B.1 lists the fraction for each component. The fits to the mass distributions of $(\mathrm{K^+K^-})_{\mathrm{min}}$ returns 5.9% of f_0 and $(\mathrm{K^+K^-})_{\mathrm{max}}$ returns 0.5% of f_0 components, and both fits return negligible non-resonance K^+K^- components.

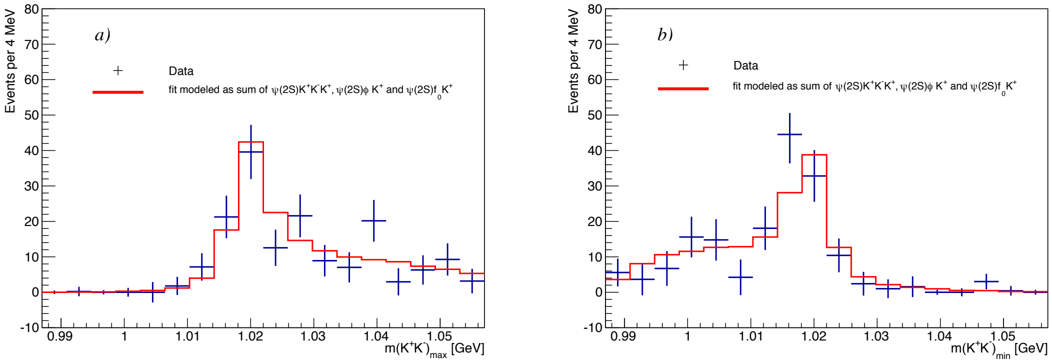

Figure B.4: a) The B sideband subtracted $(\mathrm{K^+K^-})_{\mathrm{max}}$ mass distribution is shown with dotted line and the red line is the fit modeled as sum of $\psi(2S)\phi K^+$, $\psi(2S)K^+K^-K^+$, and $\psi(2S)\mathrm{f_0}K^+$. b) The B sideband subtracted $(\mathrm{K^+K^-})_{\mathrm{min}}$ mass distribution is shown with dotted line and the red line is the fit modeled as sum of $\psi(2S)\phi K^+$, $\psi(2S)K^+K^-K^+$, and $\psi(2S)\mathrm{f_0}K^+$.

Table B.1: The fraction for each $\psi(2S)K^+K^-K^+$, $\psi(2S)\phi K^+$ and $\psi(2S)f_0K^+$ components is listed here.

Component	Fraction from $m(K^+K^-)_{max}$	Fraction from $m(K^+K^-)_{min}$
$\psi(2S)\phi K^+$	0.995 ± 0.095	0.941 ± 0.092
$\psi(2S)f_0K^+$	0.005 ± 0.096	0.059 ± 0.066
$\psi(2S)K^+K^-K^+$	0.000 ± 0.087	0.000 ± 0.035

APPENDIX C
PILEUP SYSTEMATIC STUDY USING SPLIT SAMPLE METHOD

This section is copied from CMS AN 2012/437.

We calculated the signal/normalization channel yield w.r.t triggers/run-period per unit of luminosity. In Table C.1 signal/normalization channel yield w.r.t run period per fb^{-1} of luminosity is presented. In Table C.2, signal/normalization channel yield w.r.t HLT Dimuon5 $\psi(2S)$ trigger versions v3, v4, v5, v6 is presented.

The data set is split in N independent samples: x_i individual measurements are performed with the associated errors σ_i, where i goes from 1 to N. If the N independent measurements are statistically consistent there is no evidence for a split sample systematic error. To test the statistical consistency a χ^2 with N-1 degrees of freedom is calculated through the form

$$\chi^2 = \sum_{i=1}^{N} \frac{(x_i - \bar{x})^2}{\sigma_i^2} \tag{C.1}$$

where $\bar{x}$ is the weighted average

Table C.1: Signal/normalization channel yield per unit of luminosity vs Run epoch.

Run period	$N_{\psi(2S)\phi K+}$	$N_{\psi(2S)K+}$	Effective luminosity	$N_{\psi(2S)\phi K+}/fb^{-1}$	$N_{\psi(2S)K+}/fb^{-1}$
$Run12A\&Run2012B$	25±7	19865±168	$4.760fb^{-1}$	5.3±1.5	4173.3±35.3
$Run12C$	58±10	33226±222	$7.308fb^{-1}$	8.0±1.4	4547±30.4
$Run12D$	57±10	34442±221	$7.576fb^{-1}$	7.5±1.3	4546.2±29.2

Table C.2: Signal/normalization channel yield per unit of luminosity vs HLT Dimuon $\psi(2S)$ trigger versions.

HLT Dimuon trigger	$N_{\psi(2S)\phi K^+}$	$N_{\psi(2S)K^+}$	Effective luminosity	$N_{\psi(2S)\phi K^+}/fb^{-1}$	$N_{\psi(2S)K^+}/fb^{-1}$
$HLT\_Dimuon5\_PsiPrime\_v3$	5.1±3.4	5378±87	$1.217fb^{-1}$	4.2±2.8	4419±72
$HLT\_Dimuon5\_PsiPrime\_v4$	19.4±5.8	14489±143	$3.453fb^{-1}$	5.6±1.7	4196±41
$HLT\_Dimuon5\_PsiPrime\_v5$	17.8±5.1	8069±107	$1.825fb^{-1}$	9.8±2.8	4421±59
$HLT\_Dimuon5\_PsiPrime\_v6$	98.0±13.0	59585±294	$13.059fb^{-1}$	7.5±1.0	4563±23

$$\bar{x} = \frac{\sum_{i=1}^{N} x_i/\sigma_i^2}{\sum_{i=1}^{N} 1/\sigma_i^2} \tag{C.2}$$

with an associated statistical error $\bar{\sigma}$

$$\bar{\sigma} = \frac{1}{\sqrt{\sum_{i=1}^{N} 1/\sigma_i^2}} \tag{C.3}$$

If $\chi^2/(N-1) \leq 1$, then the measurements are consistent with each other within their errors. However, if $\chi^2/(N-1) > 1$, it is assumed that the split sample true errors are all underestimated because of an unknown systematic problem. If each subsample statistical error σ_i is scaled to

$$\sigma_i\sqrt{\frac{\chi^2}{(N-1)}} \tag{C.4}$$

then it is guaranteed that $\chi^2/(N-1) = 1$ for the new value of σ_i. In addition $\bar{\sigma}$ will be increased by the same factor and become a scaled error $\tilde{\sigma}$

$$\tilde{\sigma} = \bar{\sigma}\sqrt{\frac{\chi^2}{(N-1)}} = \sqrt{\frac{\bar{x^2} - \bar{x}^2}{N-1}} \tag{C.5}$$

where $\bar{x^2}$ is defined as

$$\bar{x^2} = \frac{\sum_{i=1}^{N} x_i^2/\sigma_i^2}{\sum_{i=1}^{N} 1/\sigma_i^2} \tag{C.6}$$

When this scaled error is smaller than the statistical error from the fit of the unsplit data set (σ_{stat}), any difference between the split samples can be interpreted as being compatible with a statistical fluctuation. The final systematic error σ_{sys} is evaluated as

$$\begin{aligned} \sigma_{sys} &= \sqrt{\tilde{\sigma}^2 - \sigma_{stat}^2} && \text{if} \quad \tilde{\sigma} > \sigma_{stat} \\ \sigma_{sys} &= 0 && \text{if} \quad \tilde{\sigma} \leq \sigma_{stat} \end{aligned} \tag{C.7}$$

REFERENCES

[1] Das Souvik. Observation Of The Dalitz Decay Of The First Excited State Of The Charmed-Strange Meson. *Cornell Library*, 2011.

[2] S. L. Glashow, J. Iliopoulos, and L. Maiani. Weak interactions with lepton-hadron symmetry. *Phys. Rev. D*, 2:1285–1292, Oct 1970.

[3] Makoto Kobayashi and Toshihide Maskawa. CP Violation in the Renormalizable Theory of Weak Interaction. *Prog. Theor. Phys.*, 49:652–657, 1973.

[4] S. W. Herb, D. C. Hom, L. M. Lederman, J. C. Sens, H. D. Snyder, J. K. Yoh, J. A. Appel, B. C. Brown, C. N. Brown, W. R. Innes, K. Ueno, T. Yamanouchi, A. S. Ito, H. Jöstlein, D. M. Kaplan, and R. D. Kephart. Observation of a dimuon resonance at 9.5 gev in 400-gev proton-nucleus collisions. *Phys. Rev. Lett.*, 39:252–255, Aug 1977.

[5] F. Abe et al. Observation of top quark production in $\overline{p}p$ collisions with the collider detector at fermilab. *Phys. Rev. Lett.*, 74:2626–2631, Apr 1995.

[6] S. Abachi et al. Search for high mass top quark production in $p\bar{p}$ collisions at $\sqrt{s} = 1.8$ TeV. *Phys. Rev. Lett.*, 74:2422–2426, 1995.

[7] Georges Aad et al. Observation of a new particle in the search for the Standard Model Higgs boson with the ATLAS detector at the LHC. *Phys. Lett.*, B716:1–29, 2012.

[8] Serguei Chatrchyan et al. Observation of a new boson at a mass of 125 GeV with the CMS experiment at the LHC. *Phys. Lett.*, B716:30–61, 2012.

[9] Wanwei Wu. Semi-leptonic Decay of Lambda-b in the Standard Model and with New Physics. Master's thesis, Mississippi U., 2015.

[10] David J. Gross and Frank Wilczek. Ultraviolet behavior of non-abelian gauge theories. *Phys. Rev. Lett.*, 30:1343–1346, Jun 1973.

[11] H. David Politzer. Reliable perturbative results for strong interactions? *Phys. Rev. Lett.*, 30:1346–1349, Jun 1973.

[12] Particle Data Group, K. A. Olive, et al. Review of Particle Physics. *Chin. Phys. C*, 38:090001, 2014.

[13] John M. Campbell, J. W. Huston, and W. J. Stirling. Hard Interactions of Quarks and Gluons: A Primer for LHC Physics. *Rept. Prog. Phys.*, 70:89, 2007.

[14] C. P. Jessop et al. First observation of the decay $B \to J/\psi\phi K$. *Phys. Rev. Lett.*, 84:1393, 2000.

[15] M. Wirbel, B. Stech, and Manfred Bauer. Exclusive Semileptonic Decays of Heavy Mesons. *Z. Phys.*, C29:637, 1985.

[16] Manfred Bauer, B. Stech, and M. Wirbel. Exclusive Nonleptonic Decays of D, D(s), and B Mesons. *Z. Phys.*, C34:103, 1987.

[17] Thomas E. Browder, Klaus Honscheid, and Daniele Pedrini. Nonleptonic decays and lifetimes of b quark and c quark hadrons. *Ann. Rev. Nucl. Part. Sci.*, 46:395–469, 1996.

[18] J. J. Aubert, U. Becker, P. J. Biggs, J. Burger, M. Chen, G. Everhart, P. Goldhagen, J. Leong, T. McCorriston, T. G. Rhoades, M. Rohde, Samuel C. C. Ting, Sau Lan Wu, and Y. Y. Lee. Experimental observation of a heavy particle j. *Phys. Rev. Lett.*, 33:1404–1406, Dec 1974.

[19] J. E. Augustin et al. Discovery of a Narrow Resonance in e+ e- Annihilation. *Phys. Rev. Lett.*, 33:1406–1408, 1974. [Adv. Exp. Phys.5,141(1976)].

[20] F. Abe et al. Observation of $B^+ \to \psi(2S)K^+$ and $B^0 \to \psi(2S)K^{*0}(892)$ decays and measurements of B meson branching fractions into J/ψ and $\psi(2S)$ final states. *Phys. Rev.*, D58:072001, 1998.

[21] Matthias Neubert and Berthold Stech. Nonleptonic weak decays of B mesons. *Adv. Ser. Direct. High Energy Phys.*, 15:294–344, 1998.

[22] V. M. Belyaev, A. Khodjamirian, and R. Ruckl. QCD calculation of the $B \to \pi$, K form-factors. *Z. Phys.*, C60:349–356, 1993.

[23] Andrzej J. Buras. QCD factors a1 and a2 beyond leading logarithms versus factorization in nonleptonic heavy meson decays. *Nucl. Phys.*, B434:606–618, 1995.

[24] A.J. Buras and M. Lindner, editors. *M. Neubert, V. Rieckert, B. Stech and Q.P. Xu, in Heavy Flavours*, chapter 8, page 286. World Scientific,Singapore, 1 edition, 1992.

[25] CMS Collaboration. CMS Introduction Session for Newcomers. *CMS workshop*, 2014.

[26] Tai Sakuma and Thomas McCauley. Detector and Event Visualization with SketchUp at the CMS Experiment. *J. Phys. Conf. Ser.*, 513:022032, 2014.

[27] Serguei Chatrchyan et al. CMS Introduction Session for Newcomers. 2015.

[28] Serguei Chatrchyan et al. Performance of CMS muon reconstruction in pp collision events at $\sqrt{s} = 7$ TeV. *JINST*, 7:P10002, 2012.

[29] S Chatrchyan et al. Commissioning and Performance of the CMS Silicon Strip Tracker with Cosmic Ray Muons. *JINST*, 5:T03008, 2010.

[30] Addendum to the CMS ECAL technical design report: Changes to the CMS ECAL electronics. 2002.

[31] CMS Collaboration. Technical proposal for the upgrade of the CMS detector through 2020. Technical Report CERN-LHCC-2011-006. LHCC-P-004, Jun 2011.

[32] *The CMS hadron calorimeter project: Technical Design Report*. Technical Design Report CMS. CERN, Geneva, 1997.

[33] S. Dasu et al. CMS. The TriDAS project. Technical design report, vol. 1: The trigger systems. 2000.

[34] Sergio Cittolin, Attila Rcz, and Paris Sphicas. *CMS The TriDAS Project: Technical Design Report, Volume 2: Data Acquisition and High-Level Trigger. CMS trigger and data-acquisition project*. Technical Design Report CMS. CERN, Geneva, 2002.

[35] S Chatrchyan et al. Performance of CMS Muon Reconstruction in Cosmic-Ray Events. *JINST*, 5:T03022, 2010.

[36] R. Frhwirth. Application of kalman filtering to track and vertex fitting. *Nuclear Instruments and Methods in Physics Research Section A: Accelerators, Spectrometers, Detectors and Associated Equipment*, 262(2):444 – 450, 1987.

[37] Measurement of Tracking Efficiency. 2010.

[38] Vardan Khachatryan et al. Prompt and non-prompt J/ψ production in pp collisions at $\sqrt{s} = 7$ TeV. *Eur. Phys. J.*, C71:1575, 2011.

[39] Serguei Chatrchyan et al. Measurement of the Inclusive W and Z Production Cross Sections in pp Collisions at $\sqrt{s} = 7$ TeV. *JHEP*, 10:132, 2011.

[40] Particle-Flow Event Reconstruction in CMS and Performance for Jets, Taus, and MET. Technical Report CMS-PAS-PFT-09-001, CERN, 2009. Geneva, Apr 2009.

[41] Commissioning of the particle-flow event reconstruction with leptons from J/ψ and W decays at 7 TeV. Technical Report CMS-PAS-PFT-10-003, CERN, 2010. Geneva, 2010.

[42] S. Chatrchyan et al. The CMS experiment at the CERN LHC. *JINST*, 3:S08004, 2008.

[43] CMS Collaboration. CMS Introduction Session for Newcomers. *CMS workshop*, 2014.

[44] Claudia Patrignani. On the particle data group evaluation of chi(c)(1P) and psi-prime(2S) branching ratios. *Phys. Rev.*, D64:034017, 2001.

[45] Jonathan Lewis and Rick van Kooten. Review of Physics Results from the Tevatron: Heavy Flavor Physics. *Int. J. Mod. Phys.*, A30(06):1541003, 2015.

[46] T. Aaltonen et al. Evidence for a Narrow Near-Threshold Structure in the $J/\psi\phi$ Mass Spectrum in $B^+ \to J/\psi\phi K^+$ Decays. *Phys. Rev. Lett.*, 102:242002, 2009.

[47] R Aaij et al. Search for the $X(4140)$ state in $B^+ \to J/\psi\phi K^+$ decays. *Phys. Rev. D*, 85:091103, 2012.

[48] Victor Mukhamedovich Abazov et al. Search for the X(4140) state in $B^+ \to J/\psi\phi K^+$ decays with the D0 detector. *Phys. Rev. D*, 89:012004, 2014.

[49] Serguei Chatrchyan et al. Observation of a peaking structure in the $J/\psi\phi$ mass spectrum from $B^\pm \to J/\psi\phi K^\pm$ decays. *Phys. Lett. B*, 734:261, 2014.

[50] J. P. Lees et al. Study of $B^{\pm,0} \to J/\psi K^+K^-K^{\pm,0}$ and search for $B^0 \to J/\psi\phi$ at BaBar. *Phys. Rev. D*, 91:012003, 2015.

[51] Roel Aaij et al. Observation of $J/\psi\phi$ structures consistent with exotic states from amplitude analysis of $B^+ \to J/\psi\phi K^+$ decays. 2016.

[52] Roel Aaij et al. Amplitude analysis of $B^+ \to J/\psi\phi K^+$ decays. 2016.

[53] J. Beringer et al. Review of Particle Physics (RPP). *Phys. Rev.*, D86:010001, 2012.

[54] Torbjorn Sjostrand, Stephen Mrenna, and Peter Z. Skands. PYTHIA 6.4 Physics and Manual. *JHEP*, 05:026, 2006.

[55] D. J. Lange. The EvtGen particle decay simulation package. *Nucl. Instrum. Meth.*, A462:152–155, 2001.

[56] S. Agostinelli et al. GEANT4: A Simulation toolkit. *Nucl. Instrum. Meth.*, A506:250–303, 2003.

[57] S. Chatrchyan et al. The CMS experiment at the CERN LHC. *JINST*, 3:S08004, 2008.

[58] CMS Luminosity Based on Pixel Cluster Counting - Summer 2012 Update. Technical Report CMS-PAS-LUM-12-001, CERN, Geneva, 2012.

[59] Muon Reconstruction in the CMS Detector. Technical report, CERN, Geneva, 2008.

[60] CMS Physics Analysis Toolkit (PAT): Tutorial. Technical report, CERN, Geneva, 2014.

[61] Vardan Khachatryan et al. CMS Tracking Performance Results from early LHC Operation. *Eur. Phys. J.*, C70:1165–1192, 2010.

[62] K. Prokofiev and T. Speer. A kinematic fit and a decay chain reconstruction library. *CMS Internal Note*, page 106, 2004.

[63] Giovanni Punzi. Sensitivity of searches for new signals and its optimization. *eConf*, C030908:MODT002, 2003. [,79(2003)].

[64] Serguei Chatrchyan et al. Description and performance of track and primary-vertex reconstruction with the CMS tracker. *JINST*, 9(10):P10009, 2014.

[65] Measurement of Tracking Efficiency. 2010.

[66] Particle Data Group, K. A. Olive, et al. Review of Particle Physics. *Chin. Phys. C*, 38:090001, 2014.

[67] Glen Cowan, Kyle Cranmer, Eilam Gross, and Ofer Vitells. Asymptotic formulae for likelihood-based tests of new physics. *Eur. Phys. J. C*, 71:1554, 2011.

[68] Hans Wenzel. Calorimeter and tracking simulation. 2013.

[69] Christian W. Fabjan and Fabiola Gianotti. Calorimetry for particle physics. *Rev. Mod. Phys.*, 75:1243–1286, Oct 2003.

[70] R. Barlow and C. Beeston. Fitting using finite monte carlo samples. *Comp. Phys. Comm.*, 77:219–228, 1993.